

Controlling Dopant Rich Layers in Solar Cells

by

Abu Bakr Siddique

Thesis submitted for
the Degree of Doctor of Philosophy

Jan, 2018

Supervisor: Prof Peter R Wilshaw





Abstract

Controlling Dopant Rich Layers in Solar Cells

Abu Bakr Siddique
St. Anne's College
Department of Materials, University of Oxford

Thesis submitted for the Degree of Doctor of Philosophy
Michaelmas Term, 2017

Improving the efficiency of silicon (*Si*) solar cells relies on the understanding and optimization of individual processing steps. One such processing step, namely the diffusion of phosphorus (*P*), has been found to influence cell efficiencies significantly. This thesis discusses a mathematical model of *P* diffusion in *Si* based on first order approximations.

Phosphorus diffusion studies have been carried out in small increments of time that facilitate the development of a diffusion model which is shown to agree reasonably well with experimental profiles over a wide range of processing conditions. It is assumed that phosphorus diffuses via vacancies in the high concentration region and via interstitials in the low concentration region. A supersaturation of interstitials due to the kick out reactions enhances dopant diffusivity in the low concentration region. However, the dissociation of phosphorus interstitial pairs into phosphorus vacancy pairs at high doping levels facilitate the suppression of excess interstitials with the help of surface injected vacancies, resulting in the lowering of the overall free energy. For the very high doping levels, the dissociation rate of phosphorus interstitials is rapid in comparison to the kick out reactions that enables the slowly injected surface vacancies to completely suppress the interstitial supersaturation, thereby restoring point defect equilibrium wherein the system attains the lowest energy configuration.

The model uses the relative (to the intrinsic) concentration of point defects instead of actual point defect concentrations. This approach is particularly useful since it significantly reduces the number of fitting parameters of the model by allowing the use of an effective diffusivity in the flux equation. The effective P diffusivity is also used in the modelling of dopant precipitation kinetics, where the growth (and dissolution) of precipitates by the addition (removal) of single solute atoms is considered. Appropriate corrections are used to account for the formation of small sized clusters that are often present along with larger precipitates. The diffusion model is argued to be consistent with previous findings and is able to demonstrate very good simulation accuracies compared to all previous models.

Electrically inactive *P* limits the low wavelength response of the solar cell. The simulation developed here, based on the finite difference method (FDM), show that high temperature diffusion processes for very short durations can achieve low levels of electrically inactive *P*. In addition, such processes are predicted to result in higher levels of the electrically active *P* thereby improving contact resistance between metal and *Si*.

ACKNOWLEDGMENTS

All praise and glory to Allah Almighty, whose presence I have felt throughout my life. Its guidance through thick and thin has enabled me to achieve this goal.

I would like to express my upmost gratitude to my supervisor Professor Peter R. Wilshaw who provided me with invaluable support, guidance, encouragement and supervision throughout this journey. I would also like to thank Dr. Phillip Hamer for useful discussions and Radka Chackalova for support and assistance. Being part of the Semiconductor group at Oxford has been a wonderful experience. I thank Sebastian, George and Kanad for making my stay at Oxford memorable. In addition I am fortunate to have had the company of John, Min, Shark, Fred, Richard, Lucy and Katie.

I am grateful to Thermco Systems (a subsidiary of Tetreon Technologies Ltd) for funding, material supply and lab set up. I would like to take this opportunity to convey special thanks to the entire staff at Tetreon for their immense support throughout these years and in particular to Mr. Gerald Thurgood, Managing Director at Tetreon, for putting faith in this work. The author is grateful to the support of Edward Renouf, Garry Oldfield and Steve Leggett with furnace setup and design and to Kevin Barthrop, Ian McGregor, Helen and Amanda Ansell for assistance with material supply.

I will like to thank Prof. Ravi Silva and Dr. Damitha Adikaari of the University of Surrey for useful discussions and my friends, Miss A. Nazir Ahmed & Hasan Ashraf, for encouragement.

The author is indebted to the University of Engineering & Technology (UET), Peshawar, Pakistan for funding.

A special thank you to my father (FarhatUllah Babar), mother (Mussarrat Babar), brothers (Muhammad and Nusrat) and sisters (Amina, Kulsoom & Ayesha) for their love, understanding and endless support. I would not have been able to complete this work without the prayers of Amma (my mother).

LIST OF ACRONYMS

BSF	Back Surface Field
CB	Conduction Band
FSF	Front Surface Field
FZ	Float zone
GI-XRF	Grazing Incidence X-ray Fluorescence Spectroscopy
HCPD	High Concentration Phosphorus in-diffusion
MFC	Mass Flow Controller
N_2	Nitrogen Gas
O_2	Oxygen Gas
P	Phosphorus
$POCl_3$	Phosphor-oxy-trichloride
PSG	Phosphosilicate Glass
PV	Photovoltaics
SCCM	Standard centimetre cubed per minute
Si	Silicon
SIMS	Secondary Ion Mass Spectroscopy
SLPM	Standard litres per minute

LIST OF SYMBOLS

D	Diffusion coefficient [$cm^2 sec^{-1}$]
I	Silicon self interstitial.
V	Silicon vacancy.
C_{X^z}	Concentration of point defect, X (I or V), [cm^{-3}].
$C_{X^{z,*}}$	Concentration of point defect, X, in the charge state, z, under equilibrium ($*$) conditions [cm^{-3}].
$C_{X_i^{z,*}}$	Concentration of point defect, X, in the charge state, z, under equilibrium ($*$) and intrinsic (i) conditions [cm^{-3}].
n_i	Intrinsic carrier concentration [cm^{-3}].
n	Electron concentration [cm^{-3}].
n_i	Intrinsic carrier concentration [cm^{-3}].
C_P^+	Concentration of electrically active phosphorus [cm^{-3}].
C^{Th}	Vacancy percolation threshold concentration [cm^{-3}].
C_P	Concentration of total phosphorus [cm^{-3}].
S_{eff}	Effective Supersaturation Factor of self interstitials. Ratio of the actual concentration of self interstitials to their concentration under equilibrium conditions.
h	Field enhancement factor.
$(PX)^{z+1}$	Pair of ionized phosphorus, P^+, and point defect, X, in charge state, z.
$C_{(PX)^{z+1}}$	Concentration of the ionized phosphorus and point defect (X in charge state z) pair, [cm^{-3}].
$C_{(PX)^{z+1,*}}$	Concentration of the ionized phosphorus and point defect pair under equilibrium ($*$) conditions, [cm^{-3}].
$C_{(PX)_i^{z+1,*}}$	Concentration of interstitials of charged state z under equilibrium ($*$) and intrinsic (i) conditions [cm^{-3}].
J	Flux [$cm^{-2} sec^{-1}$].
$J_{(PX)^{z+1}}$	Flux of the ionized phosphorus and point defect (X in charge state z) pair, [$cm^{-2} sec^{-1}$].
$D_{(PX)_i^{z+1,*}}$	Diffusivity of P due to pairing with X under equilibrium and intrinsic conditions [$cm^2 sec^{-1}$]
f_u	Concentration of precipitates of size u (precipitates comprising of u P atoms) [cm^{-3}].
g_u	Growth rate of precipitates of size u [sec^{-1}].
d_u	Dissolution rate of precipitates of size u [sec^{-1}].
R_u	Net growth rate of precipitates of size u [$cm^{-3} sec^{-1}$].
λ_u	Kinetic precipitation factor [cm].
R_u^{eff}	Effective radius of precipitate of size u [cm].
ΔG_u	Change in free energy of precipitates of size u [eV].
ΔG_u^{excess}	Change in precipitate excess energy [eV].
C_{SS}	Solid solubility limit of P in Si [cm^{-3}].
B	Parabolic rate constant [$nm^2 s^{-1}$].
B/A	Linear rate constant [nm].
x_i	Initial oxide thickness [cm].
τ	Time constant associated with the initial oxide thickness [s].

S_0	Supersaturation factor of neutrally charged silicon self-interstitials. Ratio of the actual concentration of neutral self-interstitials to their concentration under equilibrium conditions.
S_1	Supersaturation factor of negatively charged silicon self-interstitials. Ratio of the actual concentration of negative self-interstitials to their concentration under equilibrium conditions.
n_{k1}	The electron concentration at which the dissociation rate of $(PI)^+$ equals the rate of excess I^0 formation $[cm^{-3}]$.
n_{k2}	The electron concentration at which the dissociation rate of $(PI)^0$ equals the rate of excess I^- formation $[cm^{-3}]$.
m	Number of phosphorus atoms with which a vacancy interacts while percolating through the material.

TABLE OF CONTENTS

Chapter 1 Introduction 1

1.1 Solar Energy Outlook 1
1.2 Principles of Solar Cell Operation 2
1.3 Phosphorus Diffusion in Solar Cells 4
1.4 $POCl_3$ Diffusion and the *PSG/Si* System 7
1.5 Limitations of $POCl_3$ Doping and a Proposed Mechanism for Reducing Inactive P . 9
1.6 Project Aims 13
1.7 Thesis Outline 14

2 Chapter 2 background 15

2.1 Fick's Law 15
2.2 Point Defects 16
2.3 Extrinsic Diffusion 20
2.3.1 Field Enhancement Factor 21
2.3.2 Point Defect Concentrations 23
2.4 Defect Mediated Dopant Diffusion Equations 25
2.5 High Concentration Phosphorus in-diffusion (HCPD) 31
2.5.1 The electrically active phosphorus profile 32
2.5.2 Inactive Phosphorus: precipitation, solubility & modelling 40
2.5.2.1 Physics of Precipitation 41
2.5.2.2 Kinetic Rate Equations 42
2.5.2.3 Solid Solubility of Phosphorus 44
2.5.3 Summary of HCPD 46

3 Chapter 3 Experimental Techniques 48

3.1 Characterization Techniques 48
3.1.1 Four Point Probe 49
3.1.2 Secondary Ion Mass Spectroscopy 50
3.2 Diffusion Furnace 59
3.3 Sample Preparation 60

4 Chapter 4 A Simulation Study of Phosphorus Diffusion in Silicon 64

4.1 Simulation Methodology 66
4.2 Phosphorus Concentration at the Si surface 72
4.3 Effective Diffusivity of Phosphorus 78
4.3.1 IV Recombination during P Diffusion 81
4.3.2 Dopant Defect Pair Concentrations 82

4.3.3 Interstitial Concentrations 84
4.3.3.1 Supersaturation Factor 85
4.3.3.2 Dissociation & Recombination Processes 86
4.3.3.3 Effective Supersaturation Factors 91
4.3.4 Interstitial Mediated Diffusion Equations 94
4.3.5 Vacancy Mediated P Diffusion 97
4.4 Considerations in the determination of constants 100
4.5 Summary 113
5 Chapter 5 Results and Discussion 114
5.1 Results 114
5.2 Comparison of constants with values from previous studies 123
5.2.1 Constants for the effective diffusivity of P 123
5.2.2 Constants for the P precipitation kinetics 126
5.3 Concentration profiles of electrically active P 135
5.4 Summary 141
6 Chapter 6 Conclusions and future work 142
7 References 144
8 Appendix A 153
9 Appendix B 154

LIST OF FIGURES

Figure 1: Space charge region of a PN junction and the corresponding energy diagram. (a) Electric field in the junction region is formed between positive ions on the n-side of the junction and negative ions on the p-side of the junction, (b) Bending of conduction and valence bands takes place in the junction region [5]. 3

Figure 2: SIMS (Secondary ion mass spectroscopy) profile of *P* in *Si* (black) obtained in this work after in-diffusion from $POCl_3$ source at 890 ºC for 9.25 minutes. Profile displays three distinct regions (see text for explanation). Dashed red line depicts the expected electrically active *P* profile. These data will be discussed in more detail in section 4.5..... 6

Figure 3: [21] Schematic of $POCl_3$ diffusion process. Oxygen, nitrogen and the dopant gas, $POCl_3$, are injected from one end of the tube and extracted at the other. Diffusion takes place at high temperatures inside the wafers placed in the quartz tube. The tube is heated electrically..... 8

Figure 4: SIMS (Secondary ion mass spectroscopy) profile of *P* in the *PSG/Si* system for process 10 (green) and process 12 (purple) as obtained after in-diffusion from $POCl_3$ source at 890 ºC for 9.25 minutes with N_2 flows through bubbler of 200 SCCM (standard cubic centimetres per minute) and 1750 SCCM, respectively. Flat P profiles to the left of the respective P peaks represent the *PSG*. The *Si* substrate is located to the right of the P peak (after the dip). Regions between the *PSG* and *Si* are the interfacial regions (see section 3.1.2 for more details). 10

Figure 5: [29] Diffusion coefficients of important elements in Si at low concentrations. Transition elements in green: nickel (Ni), copper (Cu), iron (Fe) and lithium (Li). Hybrid impurities in blue: gold (Au) and platinum (Pt). Important substitutional dopants in red: boron (B), phosphorus (P), arsenic (As) and antimony (Sb)..... 17

Figure 6: Vacancy diffusion mechanism in an equivalent picture of the silicon lattice represented by a two dimensional hexagonal structure. Clockwise: (a) A vacancy (yellow) approaches an impurity atom (red) and (b) exchanges lattice sites with it resulting in a diffusional hop of the dopant to the left. The vacancy then (c) diffuses away from the dopant atom to a third nearest neighbour site and (d) returns via a different path. The dopant and vacancy again exchange lattice sites (e) resulting in resulting in a second diffusional hop of the dopant to the left..... 19

Figure 7: Simulated electrically active *P* profile for process 6 as listed in Appendix A (890 ºC, 14.25 mins) as obtained in this work. Region 1 is also referred to as the plateau region. Intersection between regions 2 & 3 is referred to as the kink. 33

Figure 8: Theoretical depiction of *P*, S_I (interstitial supersaturation) and S_V (vacancy undersaturation) profiles in *Si* after in-diffusion from a surface source [58]. 36

Figure 9: [33] The vacancy (yellow) will move from B (second coordination site from dopant P1, red) to A (second coordination site from dopant P2, green) and percolate through the structure..... 38

Figure 10: Solubility limit and maximum electrically active level of *P* as defined in [66] for the temperature range 750-1100 ºC..... 46

Figure 11: [72] Schematic of a four-point probe. The probe spacing is denoted by S. Inner probes at locations x_1 and x_2 measure voltage as current flows between the outer two probes. 49

Figure 12: [73] Schematic of the *SIMS* technique. See text for explanation. 51

Figure 13: *SIMS* profile (blue) of *P* in the *PSG* & in the *PSG/Si* interface region for process 5 in Appendix A (890 ºC, 9.25 mins). Inset shows the complete profile in the *PSG/Si* system. Dotted red line in the pile up region depicts the expected profile in this region (see text for explanation). 57

Figure 14: Conventional & $PCs2 + SIMS$ profiles for process 6 in Appendix A (890 ºC, 14.25 mins). 58

Figure 15: Schematic of the diffusion furnace used in this study. Furnace comprised of three heating zones. The tube was 1375 mm long and had an internal diameter of 205 mm. For each diffusion run, wafers were loaded on five different slots on a wafer boat with a spacing of 10 cm between wafers..... 59

Figure 16: Sheet resistance versus diffusion time for the specimen in slot 2 (as illustrated in Figure 15) for diffusion processes conducted at 890 ºC. Error bar depict the maximum variation across the wafer. Clearly, shallow emitters with sheet resistances between 80-140 Ω/□ can be formed within 6-9 minutes at 890 ºC. 62

Figure 17: Schematic of FDM where flux of the solute $CP +$ flowing across cell i is shown. Ru is the flux of solute involved in the net growth from precipitate of size u to $u + 1$ due to the addition (removal) of solute atoms to (from) the u $(u + 1)$ sized precipitate. $J3$ represents the sum of the individual solute fluxes (sum of individual Ru) that are involved in the growth of precipitates of all sizes. Therefore, $J3$ represents the total solute flux due to precipitation/dissolution. 67

Figure 18: Phosphorus concentration at the silicon surface, CSi, and *PSG* thickness vs diffusion time for processes with the same temperature and gas flow composition. Processes 1-6 in appendix A. The *PSG* thicknesses were obtained by recording the depth of the P *SIMS* signal from the *PSG* surface to the *PSG/Si* interface (pile up) while CSi was (as explained in section 3.2) recorded by extrapolating the concentration in the Si bulk to the pile up region..... 73

Figure 19: Oxide thickness vs diffusion time for processes with the same temperature and gas flow composition. Processes 1-6 in appendix A. 75

Figure 20: Phosphorus concentration at the silicon surface vs diffusion time for processes with the same temperature and gas flow composition. Processes 1-6 in appendix A. 77

Figure 21: Simulated electrically active *P* profile for process 6 as listed in Appendix A (890 ºC, 14.25 mins) as obtained in this work. Region 1 is also referred to as the plateau region. Intersection between regions 2 & 3 is referred to as the kink. 79

Figure 22: [97] Normalized interstitial (solid black) and vacancy (solid red) concentrations as a function of depth into the wafer. Dashed blue line represents the normalized vacancy concentrations as per relation 4.14a ($CICV = CI * CV *$). The vacancy profile (solid red line) scales according to relation 4.14b ($CICV > CI * CV *$) near the Si

surface and according to relation 4.14a in regions further away from the Si surface. The dotted black line depicts the value of 1. 87

Figure 23: Phosphorus concentration (brown) and normalized interstitial (blue) and vacancy (solid red) concentrations as a function of depth into the wafer. Dashed red line represents the normalized vacancy concentrations as per relation 4.14a ($CICV = CI * CV *$). The vacancy profile (solid red line) scales according to relation 4.14a in region 1 and according to relation 4.14b ($CICV > CI * CV *$) in regions 2 and 3 of the P profile. 90

Figure 24: Simulated (red) and experimental (black) P profiles for process 3 (2.75 minutes long diffusion) and simulated (pink) and experimental (blue) P profiles for process 4 (5.75 minutes long diffusion). Both processes (Process 3 and Process 4) had the same diffusion temperature (890 ^{o}C) and gas composition ($POCl_3$ = 375 SCCM, O_2 = 500 SCCM, N_2 = 13.125 SLPM). The simulated profiles used a modified value for the vacancy diffusivity ($DPVi-,* = 1.54 \times 102exp - 4.7eVKTcm2s - 1$) instead of the actual value ($DPVi-,* = 1.22 \times 102exp - 4.69eVKTcm2s - 1$) that has been used in simulating P profiles in this work..... 106

Figure 25: Simulated (blue) and experimental (yellow) P profiles for process 5 (9.25 minutes long diffusion) and simulated (red) and experimental (grey) P profiles for process 6 (14.25 minutes long diffusion). Both processes (Process 5 and Process 6) had the same diffusion temperature (890 ^{o}C) and gas composition ($POCl_3$ = 375 SCCM, O_2 = 500 SCCM, N_2 = 13.125 SLPM). The simulated profiles used a modified value for the vacancy diffusivity ($DPVi-,* = 1.54 \times 102exp - 4.7eVKTcm2s - 1$) instead of the actual value ($DPVi-,* = 1.22 \times 102exp - 4.69eVKTcm2s - 1$) that has been used in simulating P profiles in this work..... 107

Figure 26: Simulated (green) and experimental (grey) P profiles for process 7 (diffusion at 865 ^{o}C) and simulated (pink) and experimental (blue) P profiles for process 4 (diffusion at 865 ^{o}C). Both processes (Process 4 and Process 7) had the same diffusion duration (5.75 minutes) and gas composition ($POCl_3$ = 375 SCCM, O_2 = 500 SCCM, N_2 = 13.125 SLPM). The simulated profiles used a modified value for the vacancy diffusivity ($DPVi-,* = 1.54 \times 102exp - 4.7eVKTcm2s - 1$) instead of the actual value ($DPVi-,* = 1.22 \times 102exp - 4.69eVKTcm2s - 1$) that has been used in simulating P profiles in this work..... 108

Figure 27: Simulated (black) and experimental (pink) P profiles for process 8 (diffusion at 925 ^{o}C) and simulated (red) and experimental (grey) P profiles for process 9 (diffusion at 968 ^{o}C). Both processes (Process 8 and Process 9) had the same diffusion duration (5.75 minutes) and gas composition ($POCl_3$ = 375 SCCM, O_2 = 500 SCCM, N_2 = 13.125 SLPM). The simulated profiles used a modified value for the vacancy diffusivity ($DPVi-,* = 1.54 \times 102exp - 4.7eVKTcm2s - 1$) instead of the actual value ($DPVi-,* = 1.22 \times 102exp - 4.69eVKTcm2s - 1$) that has been used in simulating P profiles in this work..... 109

Figure 28: Simulated (black) and experimental (pink) *P* profiles for process 8 (5.75 mins) using the constants determined in this study and listed in Table 1, i.e., using the actual value for $DPVi-,*$ (see text for explanation)..... 110

Figure 29: Simulated and experimental *P* profiles for process 8 (5.75 mins) using the constants listed in Table 1 and the modified of $t0$ (see text for explanation). 111

Figure 30: Simulated and experimental *P* profiles for process 3 and process 4 (at 890 ^{o}C)..... 115

Figure 31: Simulated and experimental *P* profiles for process 5 and process 6 (at 890 °C)..... 115

Figure 32: Simulated and experimental *P* profiles for process 4 and process 7 (5.75 mins)..... 116

Figure 33: Simulated and experimental *P* profiles for process 8 and process 9 (5.75 mins)..... 116

Figure 34: Experimental and simulated diffusion profiles for processes 5 & 10 with different $POCl_3$ contents in the gas phase. (890 ºC, 9.25 mins)..... 117

Figure 35: Experimental and simulated diffusion profiles for processes (5, 12 & 13) with same diffusion temperature (890 ºC) and duration (9.25 mins) but different gas flow composition (appendix A)..... 118

Figure 36: Experimental and simulated diffusion profiles for processes with different O_2 partial pressure in the gas phase..... 119

Figure 37: Experimental and simulated diffusion profiles for processes with different O_2 partial pressure in the gas phase..... 119

Figure 38: Simulated electrical profile (blue) for process 6 (890 °C, 14.25 mins). The vacancy diffusivity (black) drops rapidly at the intersection of regions 1 and 2. Interstitial diffusivity (red) dominates P diffusion in regions 2 and 3. The vacancy and interstitial diffusivities shown are those pertaining at the end of the simulation. 120

Figure 39: Simulated electrical profile (blue) for process 6 (890 °C, 14.25 mins). The corresponding diffusivities of P via pairing with the neutral and negatively charged interstitials are shown by the pink and green curves, respectively. These diffusivities were obtained at the end of a simulation scheme..... 122

Figure 40: Expected intrinsic diffusivity of *P* as determined via simulations (red) and the intrinsic diffusivity (black) of *P* given by Fair & Tsai [15]. (See text for explanation). 124

Figure 41: Precipitate free energy with respect to the free energy of the solute ($\Delta Gu - \Delta G1$) as a function of the precipitate size (number of P atoms) for spherical P precipitates at 890 ºC and with a solute supersaturion, $CP + CSS$, of 12. Compared to the findings of Dunham (red line), markedly lower free energy is predicted for the small precipitate sizes in this work (black line)..... 131

Figure 42: Precipitate free energy with respect to the free energy of the solute ($\Delta Gu - \Delta G1$) as a function of the precipitate size (number of P atoms) for spherical P precipitates at 890 ºC and with a solute supersaturion, $CP + CSS$, of 8. Compared to the findings of Dunham (red line), markedly lower free energy is predicted for the small precipitate sizes in this work (black line)..... 131

Figure 43: Precipitate free energy with respect to the free energy of the solute ($\Delta Gu - \Delta G1$) as a function of the precipitate size (number of P atoms) for spherical P precipitates at 890 ºC and with a solute supersaturion, $CP + CSS$, of 4. Compared to the findings of Dunham (red line), markedly lower free energy is predicted for the small precipitate sizes in this work (black line)..... 132

Figure 44: Precipitate concentration vs precipitate size (number of P atoms) for spherical P precipitates at the *Si* surface as determined at the end of a simulation. The $POCl_3$ partial pressures for processes 6 (black), 13 (red), 11 (blue) and 12 (pink) were 0.1%, 0.16%, 0.21% and 0.53%, respectively. Diffusion duration for process 6 (black) was 14.25 minutes while for all remaining processes (11, 12 and 13) the diffusion duration was 9.25 minutes. Diffusion temperature was 890 ºC for all processes..... 134

Figure 45: Precipitate concentration vs precipitate size (number of P atoms) for spherical P precipitates at the *Si* surface as determined at the end of a simulation, for processes conducted at different temperatures. Diffusion duration (5.75 minutes) and gas flow composition ($POCl_3$ = 375, O_2 = 500, N_2 = 13125 SCCM) was the same for all processes. 135

Figure 46: Simulated electrical profiles for processes 4, 5 and 6. Temperature (890 ºC) and gas flow composition ($POCl_3$ = 375 SCCM, O_2 = 500 SCCM and N_2 = 13125 SCCM) was same for all processes. 137

Figure 47: Simulated electrical profiles for processes 4, 8 and 9. Diffusion duration (5.75 minutes) and gas flow composition ($POCl_3$ = 375 SCCM, O_2 = 500 SCCM and N_2 = 13125 SCCM) was same for all processes. 137

Figure 48: Simulated total, simulated electrically active and empirically determined (using equation 4.18) total P profile for process 6 (Temperature = 890 ºC, time = 14.25 minutes, $POCl_3$ = 375 SCCM, O_2 = 500 SCCM and N_2 = 13125 SCCM)..... 138

Figure 49: Simulated total CP (dashed) and electrically active $CP+$ P profiles for low (865 ºC, 22 mins) and high (968 ºC, 5 mins) temperature processes using an overall gas composition (N_2 = 13300 SCCM, O_2 = 500 SCCM, $POCl_3$ = 200 SCCM) with small $POCl_3$ partial pressures..... 140

Figure 50: Simulated total CP P profiles for low (865 ºC, 8.5 mins) and high (968 ºC, 5 mins) temperature processes using an overall gas composition (N_2 = 13300 SCCM, O_2 = 500 SCCM, $POCl_3$ = 200 SCCM) with small $POCl_3$ partial pressures. The diffusion durations are chosen such that the final surface concentrations of the two processes are the same (see text for explanation). 141

Figure 51: Experimentally and empirically (using equation 4.4) determined phosphorus concentration at the *Si* surface concentration as a function of diffusion duration for the different diffusion temperatures..... 158

Figure 52: Experimentally and empirically (using equation 4.4) determined phosphorus concentration at the *Si* surface concentration as a function of diffusion duration for the different $POCl_3$ partial pressures. 159

LIST OF TABLES

Table 1. List of parameters used in the determination of the effective P diffusion coefficient. 112

Table 2. List of constants used in modelling dopant precipitation by Dunham [64] and in this work. 112

Table 3. Summary of the diffusion conditions used in this work. 153

Table 4. List of constants used in the determination of Si surface concentration. .. 155

Table 5. List of constants used in the determination of Si surface concentration. .. 156

Table 6. List of constants used in the determination of Si surface concentration. .. 156

CHAPTER 1
INTRODUCTION

This dissertation discusses a numerical model for high concentration phosphorus (*P*) diffusion in silicon (*Si*) from a gaseous source. Simulations offer a fast and cheap route to process design compared to iterative fabrication and testing. However, diffusion models based on physical laws often require parameters (pair binding energy, hopping frequency, etc) that are impossible to determine. The phosphorus diffusion model in this dissertation therefore makes use of first-order approximations, which are often implicit in commonly employed dopant diffusion models. However, conventional P diffusion models that do not take into account several high concentration effects and assume a priori constant surface concentration are only (somewhat) accurate when the diffusion duration is sufficiently long. These models have often also been found to have a limited scope, in that, they require a large set of fitting parameters which are often not available over a wide range of processing conditions. Contrary to conventional phosphorus diffusion models, the model proposed in this thesis can be directly used to determine the short duration diffusion profiles of practical solar cells. The aim has been to minimize the number of empirically determined parameters while increasing the predictive capability of the model in the desired temperature range.

1.1 Solar Energy Outlook

Over the last few centuries the population and techno-economic growth of countries has increased world energy requirements. This increased demand puts pressure on conventional energy sources, including oil, gas and coal. These fossil fuel energy sources are not only

limited in quantity but also cause environmental pollution. An abundantly available clean energy source is the sun's energy. It is available directly in the form of sunlight and solar heating and indirectly in the form of biomass, wind energy and hydroelectric energy. Solar cell technology relies on the photovoltaic (PV) effect to convert sunlight into electricity.

The 1973 oil embargo generated a widespread interest in alternate sources of energy. One of the most important effects was a US Government photovoltaic program that resulted in a small terrestrial photovoltaic industry. Increased funding in private industry and PV research as well as stabilized oil prices in the mid 1990s yielded a substantial reduction in module costs. Further, government programs like feed-in tariffs allowed incentives for investments. The favourable environment allowed PV manufacturers to increase production; *"Increasing volume reduces costs significantly"* [1]. Since 2000, PV growth has been following an exponential curve worldwide and installation estimates by the International Energy Agency have consistently fallen short of actual deployment [2]. Consequently, the technology has been progressing as per Swanson's law: doubling capacity reduces cell costs by approximately 20%.

Today solar technology is competing with conventional energy and in many countries PV has already reached grid parity [3]. With the current trend it is anticipated that by 2050 solar power will become the world's largest source of electricity with a total share of about 27% [4].

1.2 Principles of Solar Cell Operation

Simply put, a solar cell is a large area diode (pn junction) designed to efficiently convert incident light to electrical energy. As shown in Figure 1(a) an electric field in the junction region (space charge region) is formed between positive ions on the n-side of the junction and negative ions on the p-side of the junction [5]. Positive (negative) ions are formed due to diffusion of electrons (holes) from n-doped (p-doped) region to p-doped (n-doped) region.

The diffusion itself is driven by the concentration gradient of carriers (electrons or holes) between the two materials. The direction of the electric field is such that it allows mainly minority carriers (electrons in p-region and holes in n-region) to traverse the junction and become majority carriers (holes in p-region and electrons in n-region) in the other region.

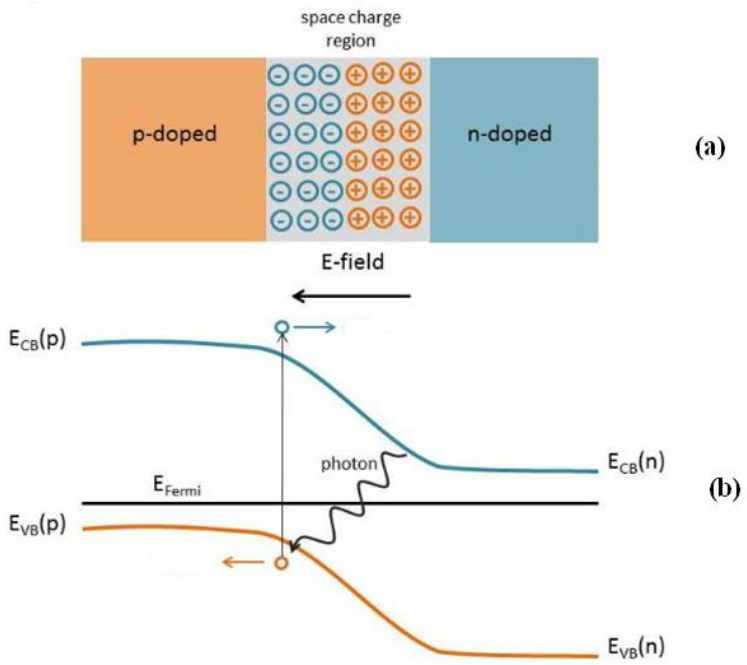


Figure 1: Space charge region of a PN junction and the corresponding energy diagram. (a) Electric field in the junction region is formed between positive ions on the n-side of the junction and negative ions on the p-side of the junction, (b) Bending of conduction and valence bands takes place in the junction region [5].

Light absorbed in either region of the junction generates free carriers (electron-hole pairs) if the energy of the incident photon is greater than the band gap energy of the semiconductor (silicon). Minority carriers generated near the junction will be quickly swept away by the field. This depletes minority carriers near the junction regions, which generates a gradient in concentration of these carriers in the p- and n-type semiconductors. Because of this concentration gradient, minority carriers generated further away from the junction can diffuse towards it before experiencing drift via the field.

The cell is completed by connecting the p- and n-regions to an external load via ohmic metal contacts. Under illumination, electrons generated (from either the p or n-region) will enter the load via the n-type semiconductor-metal contact and reach the metal-semiconductor

contact on the p-type side, where they can recombine with holes that were either swept across the junction from the n region or were directly generated by photons in the p region. The result is a light generated current of minority carriers flowing through the load.

A potential drop between the p- and n- regions always exists. Since the Fermi level remains constant, bending of the conduction and valence bands takes place in the junction, Figure 1(b) [5]. This gives rise to a potential difference also known as built in voltage which equals the amount of band bending. Theoretically, the built in voltage is cancelled out by the metal-semiconductor contact potential. When the pn junction is exposed to light (i.e. supplied with external energy) the sweep (generation and flow) of minority carriers increases the electron concentration in n-doped material and holes in p-doped materials resulting in a build-up of charge. A second electric field, between the increasing positive charges in p-region and negative charges in n-region, acts in the direction opposite to the built in field. The result is a decrease in the built in voltage and a net potential difference, ΔV, in the forward direction. This phenomenon, where a voltage appears across a pn junction when illuminated, is the *photovoltaic effect*.

The two currents in a solar cell, namely the forward current due to the potential difference and the light generated current, flow in opposite directions with the net current, I_p, given by the difference of the two. Useful power is generated in the load through current flow and the potential difference, $Power = I_p \Delta V$.

1.3 Phosphorus Diffusion in Solar Cells

Diffusion of phosphorus and boron are standard processes in the PV industry. They are often used to create a collecting junction or to improve surface passivation. Device simulations have shown [6] that an absolute improvement in cell efficiency of 2.78 % is possible by tailoring the phosphorus profile in the emitter region. Further, the process is able to improve minority carrier lifetime in p-type substrates by gettering several lifetime limiting impurities,

including iron (Fe) [7]. Heavy phosphorus doping generates a surface field irrespective of the substrate type: a feature of the phosphorus profile (as shown below) is that it naturally results in an n^+-n profile. On n-type substrates the field has been found to improve UV stability, enhance surface passivation and lower series resistance [8].

A typical solar cell profile of phosphorus is shown in Figure 2 with its three distinct regions. Also shown by the dashed line is the expected concentration of electrically active phosphorus. The two profiles are essentially the same in the tail region (low concentration) but the electrically active concentration of phosphorus saturates at high concentrations due to the formation of small clusters/precipitates [9]. A somewhat flat electrical profile, referred to as a plateau [10], followed by a rapid fall explains the n^+-n feature. The electrical profile in this region is discussed in chapter 5. Region 2 represents the rapidly falling diffusion profile and region 3 is referred to as the tail region. The intersection point between region 2 and 3 is called the kink.

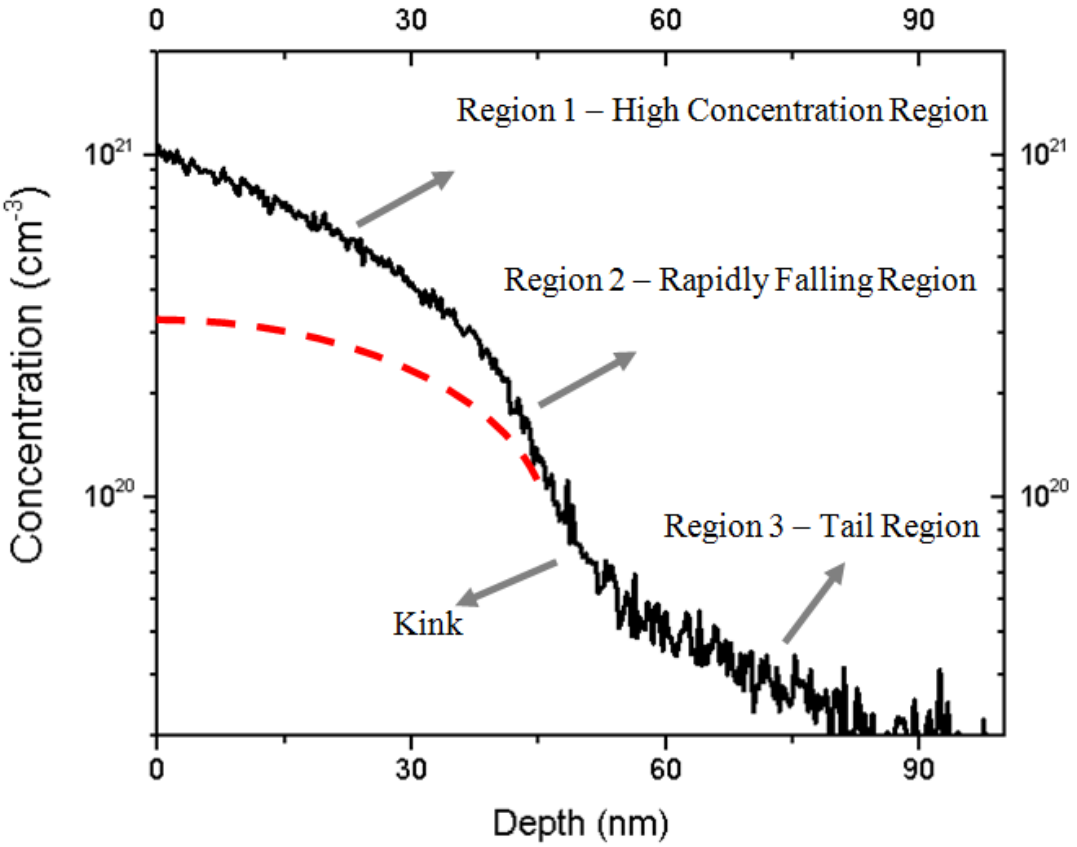


Figure 2: SIMS (Secondary ion mass spectroscopy) profile of *P* in *Si* (black) obtained in this work after in-diffusion from $POCl_3$ source at 890 ºC for 9.25 minutes. Profile displays three distinct regions (see text for explanation). Dashed red line depicts the expected electrically active *P* profile. These data will be discussed in more detail in section 4.5.

Clustered/precipitated phosphorus is expected to create deep levels within the bandgap rather than shallow donor levels [11, 12]. It is suggested [12] that the electrically inactive phosphorus significantly affects the minority carrier lifetime and/or the surface recombination velocity. In addition, the recombination rate inside the emitter scales with the total undissolved P and/or the undissolved *P* at the surface [12] whereas the recombination rate due to Auger recombination saturates with the electron concentration in the plateau region [12]. On the other hand, experimental determinations [13, 14, 15] of the electrically active and total P, following conventional processing methods, have often reported a correlation between the two concentrations. These relationships do not account for the effect of thermal history and predict that attempting to reduce the total phosphorus will reduce both dissolved and undissolved phosphorus. As a result, the general understanding seems that reduction in the undissolved phosphorus concentration will in turn increase contact resistance

of the solar cell [16]. More details about the limitations of these relationships [13, 14, 15] are given in sections 4.4 and 5.3.

Minority carrier lifetimes in surface regions of heavily doped emitters can be very low [12, 17] and the region is often termed dead [17] for photogenerated carriers. Lightly doped emitters, which are also referred to as shallow emitters, are desirable for optimum cell performance [17, 18, 19]. It is possible to reduce contact resistance between metal and a shallow emitter by improving the quality of the metal paste [20]. However, high electrically active dopant concentrations in the very near surface regions of these shallow emitters are still required to reduce contact resistance even with improved metal pastes [19]. A plateau depth of 30-50 nm [17, 19] gives an optimum balance between reduced emitter recombination and low contact resistance.

From a solar cell efficiency perspective, the undissolved phosphorus is unwanted. The presence of electrically in-active phosphorus does not affect contact resistance. Furthermore, from a recent study on the effect of *P* concentration on gettering one can easily deduce that the onset of gettering happens at concentrations (between $3 \times 10^{17} cm^{-3}$ and $4 \times 10^{19} cm^{-3}$) below the maximum electrically in-active phosphorus level [7]. One of the aims of this study is to determine, by simulation, process conditions which should achieve emitters with reduced electrically inactive phosphorus for a given plateau depth (i.e. to reduce electrically inactive phosphorus with little or no reduction in the electrically active *P* concentration level).

1.4 $POCl_3$ Diffusion and the *PSG/Si* System

Phosphorus is introduced to the wafer using a phosphor-oxy-trichloride ($POCl_3$) source. The method is widely known simply as $POCl_3$ diffusion. The process is cost effective when compared with ion implantation while from a performance point of view it has been found to be superior over other surface in diffusion methods.

A schematic of the apparatus used in $POCl_3$ diffusion is shown in Figure 3 [21]. N_2 gas is bubbled through a bubbler which contains the liquid $POCl_3$ while O_2 is supplied separately. Typically the process is carried out in an inert environment (N_2) which is also supplied via a separate MFC (Mass Flow Controller).

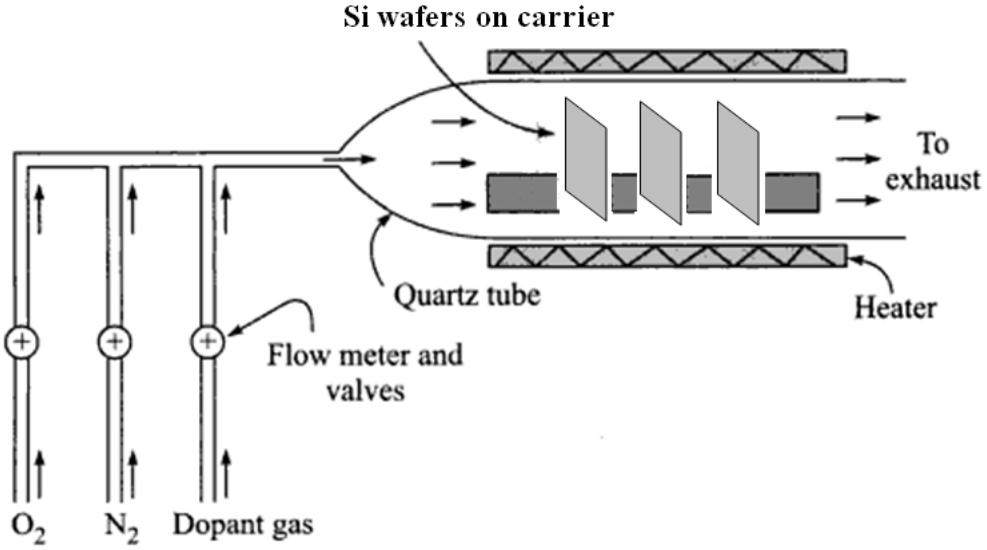


Figure 3: [21] Schematic of $POCl_3$ diffusion process. Oxygen, nitrogen and the dopant gas, $POCl_3$, are injected from one end of the tube and extracted at the other. Diffusion takes place at high temperatures inside the wafers placed in the quartz tube. The tube is heated electrically.

During $POCl_3$ diffusion the following reactions take place [22],

$$4POCl_3 + 3O_2 \rightarrow 2P_2O_5 + 6Cl_2 \quad \text{(R1.1)}$$

$$2P_2O_5 + 5Si \rightarrow 4P + 5SiO_2 \quad \text{(R1.2)}$$

$$Si + O_2 \rightarrow SiO_2 \quad \text{(R1.3)}$$

The amount of oxygen supplied is in excess to the $POCl_3$. However the process will take place even if dilute or no O_2 is used, but in that case $POCl_3$ distils into P_4O_{10}, PCl_3 and free Cl_2 which leads to silicon etching due to reaction with the pure chlorine [23]. In the case of excess O_2, etching is controlled by the formation of a phosphosilicate glass (*PSG*) which presents a barrier to Cl_2 attack. Since $POCl_3$ is very reactive, reaction R1.1 is expected to

occur near instantaneously and at temperatures much lower than the diffusion temperature [22]. One therefore expects to inject P_2O_5 and O_2 molecules only and extract (via exhaust) P_2O_5 and Cl_2 molecules.

The P_2O_5 formed will react with the silicon surface to generate the *P* dopant and also to form an SiO_2 layer on the *Si* surface, reaction R1.2. Further incoming P_2O_5 mixes with the SiO_2 to form a *PSG* glass of composition, $X \times P_2O_5 + (1 - X) \times SiO_2, \quad X \sim 0.15 - 0.3$. Excess oxygen in the gas stream will result in oxidation of the silicon surface, reaction R1.3. The *PSG* acts as a diffusion source for the underlying silicon.

1.5 Limitations of $POCl_3$ Doping and a Proposed Mechanism for Reducing Inactive P

The industrial practise to form shallow emitters comprises two steps [16]. In the first step, referred to as the deposition cycle, $POCl_3$ and O_2 gases are allowed to flow over the wafers at low temperatures (770-810 ^oC). In the second step, called drive-in, diffusion is carried out at high temperatures (840-880 ^oC) in either an inert ambient (N_2) or a partially oxidizing atmosphere. Due to the low temperatures, a shallow P profile in *Si* with very high surface concentration arises at the end of the deposition step. The second drive-in step pushes the dopant deeper within the wafer and increases the overall spread of the profile.

In this work, it was found experimentally that the $POCl_3$ process results in a highly doped PSG film but the amount of phosphorus in the *PSG* after the deposition cycle is almost independent of the $POCl_3$ partial pressure. Figure 4 shows the P profile for processes 10 and 12 (as listed in Appendix A) where only the $POCl_3$ partial pressure was changed (from 0.0536% for process 10 to 0.5311% for process 12) while all remaining processing conditions (total gas flow rate, oxygen partial pressure, temperature and time) were the same for the two processes. The profile to the right of the respective P peaks represents the

substrate (*Si*) region while that prior to it is the *PSG*. A more detailed explanation of the *PSG/Si* system and the P profiles is given in section 3.1.2 where it is explained that the *Si* surface concentration can be taken as the concentration of the dopant at a point 4nm to the right of the P peak. The $POCl_3$ partial pressure for process 12 is approximately an order of magnitude greater that of process 10. However, the total amount of P in the two *PSG* films is almost the same since the *PSG* from process 10 has almost twice the dopant and half the thickness of the *PSG* film arising after process 12.

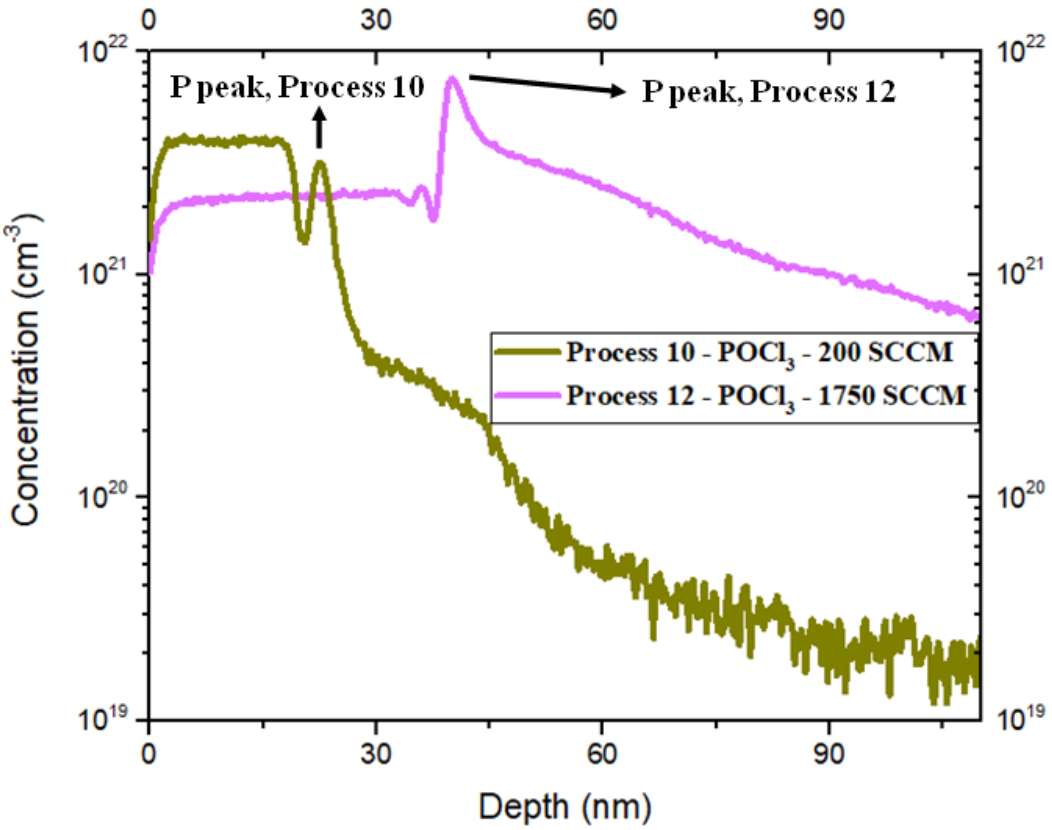


Figure 4: SIMS (Secondary ion mass spectroscopy) profile of *P* in the *PSG/Si* system for process 10 (green) and process 12 (purple) as obtained after in-diffusion from *$POCl_3$* source at 890 ºC for 9.25 minutes with N_2 flows through bubbler of 200 SCCM (standard cubic centimetres per minute) and 1750 SCCM, respectively. Flat P profiles to the left of the respective P peaks represent the *PSG*. The *Si* substrate is located to the right of the P peak (after the dip). Regions between the *PSG* and *Si* are the interfacial regions (see section 3.1.2 for more details).

From Figure 4 it is clear that increasing the $POCl_3$ partial pressure significantly increases the amount of P that penetrates into the underlying substrate. This is consistent with the findings of Negrini *et al.* [24] where the authors had found the amount of dopant in the *Si* substrate to scale exponentially with the $POCl_3$ partial pressure. Therefore, the very high $POCl_3$ contents

that are used in industrial practices result in significant amounts of P to enter into the *Si* substrate and with an almost constant high P dose in the PSG.

Due to the very low temperatures used for the deposition cycle, most of this P should be located close to the *Si* surface (thereby forming a phosphorus rich phase) as opposed to being pushed deeper into the wafer as is the case for process 12 in Figure 4. In the following high temperature drive-in cycle, P from the rich phase at the surface and from the *PSG* diffuses deeper into the wafer. For conventional drive-in cycles (840-880 ^{o}C, 7-20 mins) we expect the *Si* surface concentration not to fall significantly from the concentration level that was acquired after the deposition cycle. This we expect from the very high amounts of P in the *PSG* that is available to the *Si* substrate during drive-in and the moderate thermal budgets of drive-in cycles that result in only a modest spreading (and small decrease in the surface concentration) of the profile in *Si*. Therefore, the overall diffusion profile after the two-step method is a heavily doped emitter with significant amounts of inactive P.

The above description might explain why industrial emitters have a very high amount of inactive P but the fundamental question remains: why does the industrial practise require a significant proportion of the dopant to be inactive? The issue is that the gaseous process at low concentrations results in non-homogeneous doping across wafers and within wafers. By supplying the dopant in excess to the substrates, one ensures that all wafers (and wafer parts) are doped to at least the solubility limit (maximum electrically active P). This results in more or less a uniform distribution of electrically active phosphorus after drive-in, despite the fact that the total $POCl_3$ concentration reaching the wafers may not have been uniform. Consequently, one obtains uniform distribution of sheet resistance across and within wafers, which is one of the most important customer (PV manufacturers) requirements for the $POCl_3$ process. Several authors have reported heavily doped substrates to have very good uniformity compared to lightly doped emitters formed using low $POCl_3$ partial pressures [16, 25, 26].

One way of improving uniformity of the $POCl_3$ concentration reaching the wafers, so enabling lower concentrations to be used, would be to introduce the gas in the tube using multiple injectors instead of a single spigot. Injectors placed along the entire length of the tube, instead of a single spigot, can supply the gases locally. Such an approach might therefore be able to reduce the gas non-homogeneity within the tube; however, this method might also require local ejection (exhaustion) of gases throughout the tube length. Controlling gas flows within the tube is a complex topic. In this work, I assume that future furnace designs aided by computational fluid dynamics might overcome this obstacle.

The subject of this work is to determine the conditions that can reduce inactive P without significantly compromising the electrically active P. If an in-diffusion method like $POCl_3$ is used then for the two (electrical and total P) profiles to bear resemblance it is important that the phosphorus surface concentration does not increase significantly beyond the solubility limit ($3 - 5 \times 10^{20} cm^{-3}$ at diffusion temperatures) throughout the diffusion process. However, it is also desirable that the electrically active phosphorus concentration is at or near a maximum (the solubility limit) in the surface regions in order to ensure the lowest possible contact resistance, which in turn requires that the surface concentration does not fall much below the solubility limit during diffusion. Ideally then, the total P surface concentration must remain near the solubility limit throughout $POCl_3$ diffusion.

Since electrically inactive P is immobile, the diffusion of P takes place via the electrically active (mobile) species. Therefore, the profile of electrically active P profile is determined by the electrically active P concentration at the surface rather than the total P concentration at the surface. If the total P surface concentration remains at (close to) solubility during diffusion, there will theoretically be no (very little) discrepancy between the total P profile and the electrically active P profile, with the electrically active P still flattening out in the near surface regions. Note that the plateau in the electrical profile arises due to a very high diffusivity at these donor concentrations and will arise even if the total P was less but the

electrically active P was the same. This will be discussed in more detail in section 2.5 and in chapters 4 and 5.

A method of maintaining the surface concentration close to the solubility limit is proposed in this study. It involves using a single deposition cycle with low to moderate $POCl_3$ contents in the gas phase at high temperatures (greater than 945 ^oC). Based on the findings of Negrini *et al.* [24] we expect the surface concentration to rise rapidly beyond the solubility limit in the initial few minutes of the process. During deposition the *Si* surface concentrations, as found in this work and discussed in chapters 4 and 5, have been found to increase rapidly from low to high levels even under low to moderate $POCl_3$ partial pressures. Therefore, the duration for which the surface concentration remains close to solubility is small. In order to achieve significant diffusion depths of the electrically active P within such short durations, the diffusion temperature needs to be increased.

At this point, it should be mentioned that in the very first kinetic study of the $POCl_3$ process by Negrini *et al.* [24] it was found that the ratio of the total P to electrically active P decreases with increasing temperature for a given gas composition. However, that study was aimed at studying the process rather than decreasing the inactive P and typically involved large diffusion durations. On the other hand, the proposed method in this study involves higher temperatures but reduced durations (~5 minutes) as compared to standard processing and is aimed at reducing the inactive P for shallow junction emitters. The processing costs of the proposed method and of conventional processes are expected to be of the same magnitude.

1.6 Project Aims

It is beyond the scope of this thesis to completely model phosphorus diffusion from the gas phase in the *PSG/Si* system. Nonetheless, this thesis presents a framework that can help the

development of such a model in the future as it improves upon state of the art phosphorus diffusion modelling in silicon. The primary aims of this thesis are to

(i) develop a quantitative phosphorus diffusion model in *Si* that is consistent with state of art observations and theory

(ii) validate the model with experiments

(iii) and determine, by simulation, whether high temperature short anneals can reduce inactive P.

1.7 Thesis Outline

This thesis concerns high concentration phosphorus in-diffusion (*HCPD*) in silicon.

Chapter 2 gives a background of phosphorus diffusion mechanisms in *Si*. Chapter 3 describes the methodology and experimental techniques while Chapter 4 gives a detailed description of phosphorus diffusion mechanism as understood in this work via simulations. The simulations consider dopant precipitation and require the determination of the *Si* surface concentration empirically, which has made using a wide range of experimental data. The simulation methodology and the empirical determination of the surface concentration are discussed in chapter 4. The results of the simulations are discussed in Chapter 5 where the various model parameters are compared with previously proposed values in the literature. A discussion on the electrically active P is given in end of Chapter 5 where the ability of the high temperature process to reduce inactive P has also been demonstrated. Chapter 6 concludes this thesis and suggests that future work should consider modification of the furnace design in order to improve the $POCl_3$ diffusion process.

CHAPTER 2
BACKGROUND

Diffusion of substitutional, Group III & V, dopants in *Si* has received considerable attention since the start of the microelectronics industry. This is because their incorporation in the *Si* lattice renders the material either p-type or n-type and such regions are required for practical devices. The diffusion of these elements is meditated by native point defects (self interstitials and vacancies). Point defect concentrations are therefore critical in the study of dopant diffusion. However, the actual concentration of these defects is one of the most controversial subjects in *Si* and their reported values vary up to 8 orders in magnitude [27]. A more practical approach in modelling dopant diffusion (which is explained in this chapter) is to use the concentration of point defects relative to their concentration in an undoped (intrinsic) material. Such an approach is helpful in predicting dopant diffusion despite being limited to the specific case of point defect equilibrium. Also discussed in this chapter is high concentration phosphorus in-diffusion.

2.1 Fick's Law

Diffusion can be described as the processes whereby a system attempts to homogenize the concentration of its constituents. Any chemical gradient within the system will thus over time even out. In 1855 Adolf Fick showed [28] that the flux of species, J, is equal to the product of the gradient in concentration, C, and diffusivity, D,

$$J = -D\frac{\partial C}{\partial x} \tag{2.1}$$

The above relation is known as Fick's first law where the negative sign means that mass transfer will take place in the direction of decreasing concentration. On the other hand, mass conservation requires that in the absence of internal sinks or sources the accumulation rate $\partial C/\partial t$ of species within a given volume must equal the net flux of diffusant entering the volume (flux into the volume minus flux out of the volume).

$$\frac{\partial C}{\partial t} = -\frac{\partial J}{\partial x} \tag{2.2}$$

Substituting equation 2.1 in 2.2 gives Fick's second law as,

$$\frac{\partial C}{\partial t} = -D\frac{\partial^2 C}{\partial x^2} \tag{2.3}$$

The diffusion coefficient or diffusivity, D, is a measure of the rate with which atoms can spread. When dealing with silicon it is usually expressed in units of $cm^2 s^{-1}$.

2.2 Point Defects

A point defect (interstitial or vacancy) is a deviation from an ideal crystal. A *Si* atom displaced from its lattice site into an interstitial site is referred to as a silicon self-interstitial, I, while the empty lattice site is called a vacancy, V. Point defects play a crucial role in the diffusion of substitutional dopants in *Si*. In this section the diffusion mechanisms of substitutional dopants is discussed but first the interaction of various impurities with point defects is explained.

Diffusion coefficients of important elements at low concentrations in *Si* are shown in Figure 5 [29]. These elements can be classified into three categories: the fast interstitial diffusers which are the 3d transition elements, the intermediate or hybrid diffusers namely gold (Au) and platinum (Pt) and the important substitutional dopants of Group III & V which are classed as slow diffusers.

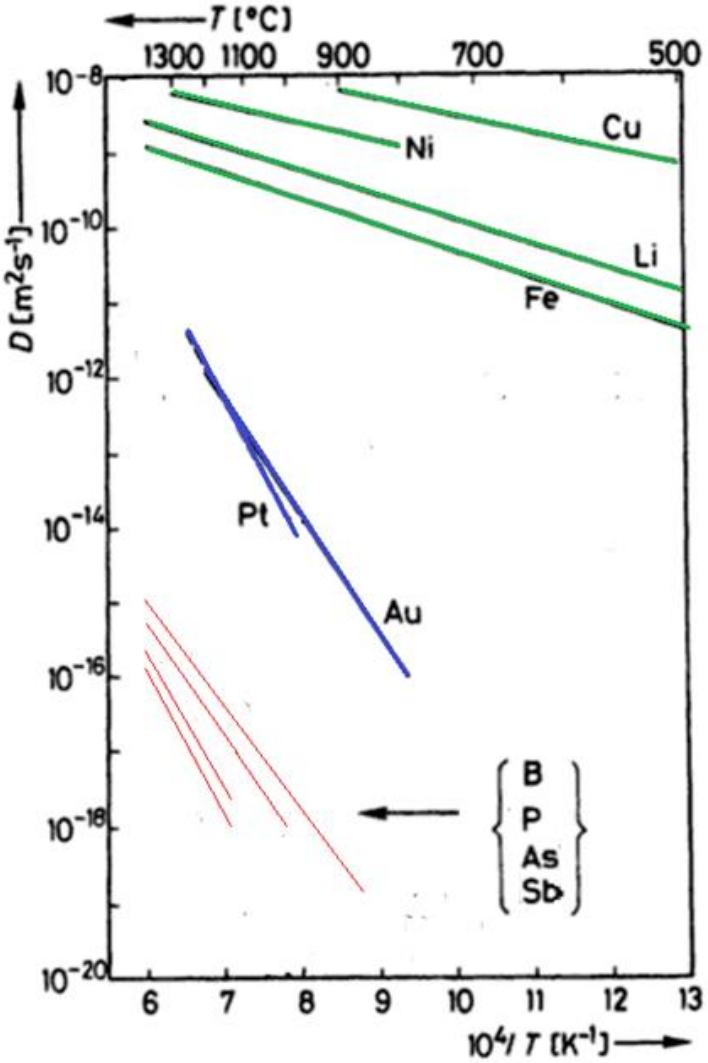


Figure 5: [29] Diffusion coefficients of important elements in Si at low concentrations. Transition elements in green: nickel (Ni), copper (Cu), iron (Fe) and lithium (Li). Hybrid impurities in blue: gold (Au) and platinum (Pt). Important substitutional dopants in red: boron (B), phosphorus (P), arsenic (As) and antimony (Sb).

The 3d transition elements dissolve in *Si* on interstitial sites and diffuse rapidly via hopping from one interstitial site to another [29]. This mechanism is called direct interstitial diffusion and does not require the presence of crystallographic defects (or native point defects). Hybrid elements also diffuse via the direct interstitial mechanism but these elements dissolve on substitutional sites [29]. They therefore need to be first displaced into an interstitial site by either a V or I. Since such a reaction requires additional energy and so hybrid impurities diffuse slower than 3d transition elements.

A substitutional dopant, A_S, can be kicked from a lattice site to an interstitial site (A_i) by a self interstitial, I. The self interstitial in this case takes up the substitutional (lattice) site, i.e. becomes a *Si* atom,

$$A_S + I \Leftrightarrow A_i \qquad \text{(R2.1)}$$

Reaction R2.1 is referred to as the kick out reaction.

The dopant in the interstitial site, A_i, can now hop between interstices but the very high solubility of Group III and V elements in *Si* means that migration from one interstitial site to another is inhibited by the reverse kick out reaction. That is, the dopant in the interstitial site, A_i, soon becomes substitutional (so releasing a self interstitial), prior to traversing significant distances. Substitutional dopants are thus the slowest diffusers in *Si* among the three categories discussed. Their migration is in fact assisted by point defects themselves and the dopant is often said to migrate by pairing with a point defect. This can be understood by analyzing the individual cases of vacancy assisted and interstitial assisted substitutional dopant diffusion.

A vacancy can pair with a dopant atom on a substitutional site, A_S, and the two can diffuse together in the crystal as a A_SV pair.

$$A_S + V \Leftrightarrow A_SV \qquad \text{(R2.2)}$$

On approaching the substitutional atom the vacancy will exchange lattice sites with it, but in order for diffusion to proceed by this pair mechanism it is important that after exchanging lattice sites with the dopant the vacancy moves [30, 31, 32, 33] away from the dopant to a third nearest neighbour site and then return via a different path, Figure 6. In other words, a partial dissociation of the dopant vacancy pair is required for diffusion to take place. In the case of no partial pair dissociation the vacancy will return to its previous site by again exchanging lattice sites, resulting in no net diffusion.

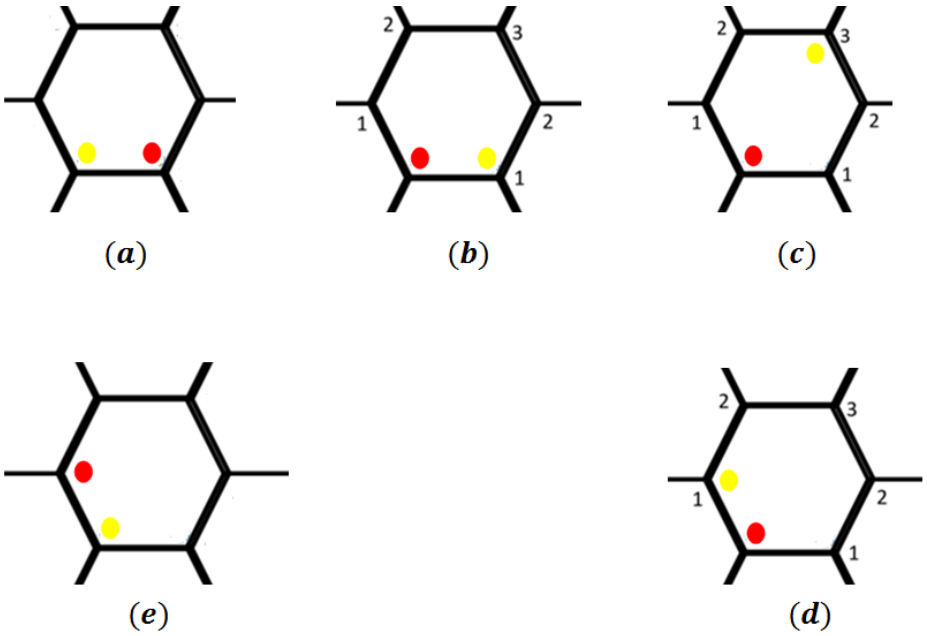


Figure 6: Vacancy diffusion mechanism in an equivalent picture of the silicon lattice represented by a two dimensional hexagonal structure. Clockwise: (a) A vacancy (yellow) approaches an impurity atom (red) and (b) exchanges lattice sites with it resulting in a diffusional hop of the dopant to the left. The vacancy then (c) diffuses away from the dopant atom to a third nearest neighbour site and (d) returns via a different path. The dopant and vacancy again exchange lattice sites (e) resulting in resulting in a second diffusional hop of the dopant to the left.

The dopant and interstitial, $A_S I$, pair is also partially bound and can be formed by the reaction,

$$A_S + I \Leftrightarrow A_S I \qquad \text{(R2.3)}$$

The dopant can also diffuse in the crystal like hybrid impurities do, i.e. it can diffuse as A_i but would become substitutional without traversing significant lengths and would require a self interstitial to knock it back into an interstitial site. However, it is not experimentally possible to distinguish between diffusion as A_i and diffusion as $A_S I$. From the viewpoint of qualitatively or quantitatively predicting the diffusion behaviour, it does not make any difference in knowing if either of these is the dominant mechanism [31]. They are collectively referred to as, interstitial type diffusion and reactions R2.1 and R2.3 are both termed as kick-out reactions [31].

2.3 Extrinsic Diffusion

Extrinsic diffusion takes place when the carrier concentration in the wafer is above the intrinsic carrier concentration. Such a situation can arise if the dopant is introduced in an already heavily doped wafer and/or when the introduced dopant is itself in high concentrations. The electron, n, and hole, p, concentrations in an extrinsically doped semiconductor are given by [34],

$$n = \frac{C_A^+ + \sqrt{{C_A^+}^2 + 4n_i^2}}{2} \tag{2.4a}$$

$$p = \frac{C_A^- + \sqrt{{C_A^-}^2 + 4n_i^2}}{2} \tag{2.4b}$$

where C_A^+ is the ionized donor concentration, C_A^- is the ionized acceptor concentration and n_i is the intrinsic carrier concentration in pure *Si* which is given by [35],

$$n_i = 1.8 \times 10^{21}\, exp\left({-0.66eV}/{KT}\right) cm^{-3} \tag{2.4c}$$

C_A^+ & C_A^- are given by [13, 34],

$$C_A^+ = \frac{C_A}{1 + 2exp\left({E_F - E_d}/{KT}\right)} \tag{2.5a}$$

$$C_A^- = \frac{C_A}{1 + 4exp\left({E_a - E_F}/{KT}\right)} \tag{2.5b}$$

where C_A is the total dopant concentration in substitutional sites, E_F is the Fermi energy and E_d and E_a are the donor and acceptor energy levels, respectively. The factors of $\frac{1}{2}$ and $\frac{1}{4}$ are the spin degeneracy factors.

Note that at room temperature $C_A^{\pm} \sim C_A$ for low doping levels ($< 10^{16} cm^{-3}$) and $C_A^{\pm} < C_A$ for moderate doping levels ($10^{16} - 10^{18} cm^{-3}$), as predicted by equations 2.5. However, at

doping levels of $3 \times 10^{18} cm^{-3}$ and above the ionization energy of shallow dopants of Groups III and V becomes zero due to increased screening of dopants by majority carriers [27]. The overall effect is that the impurity level merges with the conduction (valence) band and all donor (acceptor) atoms are ionized [27, 36]. At practical diffusion temperatures (750 – 1000 ºC), the concentration at which complete ionization takes place ($3 \times 10^{18} cm^{-3}$) is approximately the same as the intrinsic carrier concentration. Thus in the study of extrinsic diffusion $C_A^{\pm} \sim C_A$ is an implicit condition and equations 2.5 are not used.

The only problem that can then arise in determining $C_A^{\pm}$, if C_A is known, is that some of the dopant might be clustered and therefore electrically inactive. C_A in equation 2.5 refers to the total un-clustered dopant on substitutional sites. In general, clustered phosphorus is immobile. The clusters themselves can grow (dissolve) by the addition (removal) of the solute $C_A^{\pm}$. Precipitation/clustering will be discussed in sections 2.5.2.1, and in section 5.2.

From the perspective of Fick's Law, it is the substitutional/ionized dopant concentration which is important rather than the total dopant concentration. This is because the ionized dopant concentration influences point defect concentrations and thus dopant diffusivity as is shown in section 2.3.2.

2.3.1 Field Enhancement Factor

The gradient in the diffusion profile generates a gradient in carrier concentration. The electrons (holes) will tend to diffuse in this gradient in a background of an otherwise static donor (acceptor) profile (due to the very high diffusivity of carriers dopant atoms by comparison can be regarded as immobile). This tendency of carriers to move away from dopants is counterbalanced by the electrostatic attraction between the two, which in turn gives rise to an internal electric field. In the following, this additional drift force is discussed quantitatively for the case of electrons and donors, where it is shown that an additional

factor, namely the field enhancement factor, needs to be included in the flux equation for the case of extrinsic diffusion.

It is pertinent to mention that the following derivation is valid for a constant diffusivity. Where that is not the case, the direct use of the field enhancement factor in the flux equation needs to be justified. This is usually done by making appropriate approximations. Alternatively, the direct use of the field enhancement should be avoided and the flux equation should be solved using both diffusion and drift components (as has been done in section 4.3).

The flux of donors is given by the flux due to diffusion and the flux due to drift of donor atoms [37],

$$J = -D\frac{\partial C_A^+}{\partial x} + C_A^+ v \tag{2.6a}$$

where v is the velocity of the donor atom in an electric field [37], $\boldsymbol{\varepsilon}$. The electric field can be determined using the Boltzmann approximation,

$$v = \mu\boldsymbol{\varepsilon} = \frac{q}{KT}D\frac{\partial \phi}{\partial x} = \frac{q}{KT}D\frac{\partial}{\partial x}\left[-\frac{KT}{q}ln\left(\frac{n}{n_i}\right)\right] \tag{2.6b}$$

$$v = -D\frac{\partial}{\partial x}\left[ln\left(\frac{n}{n_i}\right)\right] = -D\frac{n_i}{n}\frac{\partial}{\partial x}\left(\frac{n}{n_i}\right) = -\frac{D}{n}\frac{\partial n}{\partial x} \tag{2.6c}$$

The flux term then becomes

$$J = -D\frac{\partial C_A^+}{\partial x} - \frac{DC_A^+}{n}\frac{\partial n}{\partial x} \tag{2.6d}$$

It can be shown by differentiating equation 2.4a that,

$$\frac{\partial n}{\partial x} = \frac{n}{\sqrt{C_A^{+2} + 4n_i^2}}\frac{\partial C_A^+}{\partial x} \tag{2.6e}$$

Substituting the above result, equation 2.6e, in the flux equation 2.6d we have,

$$J = -D\frac{\partial C_A^+}{\partial x} - \frac{DC_A^+}{\sqrt{{C_A^+}^2 + 4n_i^2}}\frac{\partial C_A^+}{\partial x} \tag{2.6f}$$

$$J = -D\left[1 + \frac{C_A^+}{\sqrt{{C_A^+}^2 + 4n_i^2}}\right]\frac{\partial C_A^+}{\partial x} \tag{2.6g}$$

$$J = -hD\frac{\partial C_A^+}{\partial x} \tag{2.6h}$$

The factor h is known as the field enhancement factor. It varies between 1 ($for\ C \ll n_i$) and 2 ($for\ C \gg n_i$) and is clearly not a significant effect compared to the up to 4 orders in magnitude variation in diffusivity that arises due point defect concentrations as is discussed in section 2.4.

2.3.2 Point Defect Concentrations

Point defects have energy levels within the bandgap. They can thus be charged by capturing an electron or a hole. For instance, a neutral point defect, X^0 (denoting either a vacancy or a self-interstitial), can become negatively charged X^- by capturing an electron [31],

$$X^0 + e^- \Leftrightarrow X^- \tag{R2.4}$$

Exactly which charged or neutral defects will pair with a dopant atom is determined by Columbic interaction and lattice distortion. The diffusivity of the pair (and thus that of the dopant), as shall be shown in the following section, scales with the concentration of that point defect which pairs up with the dopant. However, the concentration of point defects and their energy levels is the subject of intense discussions [27]. The reported interstitial and vacancy concentrations vary up to several orders in magnitude [27]. Moreover, the reported discrepancies refer to the total (charged plus neutral) interstitials and vacancies under

equilibrium conditions. Concentrations of individual (charged or neutral) defects and those under non-equilibrium conditions are thus far from known.

A more practical approach to dopant diffusion modelling requires knowledge of the relative (rather than the actual) concentration of point defects, which can be determined using the condition of local equilibrium. The condition of local equilibrium states that electronic processes are rapid compared to mass transfer such that we can represent the electronic process via a mass action relationship. Using the law of mass action on reaction R2.4, we have,

$$\frac{C_X^0\, n}{C_X^-} = K^*(T) \tag{2.7a}$$

where $K^*(T)$ is the equilibrium constant for the particular reaction ($K^*(T)$ is a function of temperature only), C_X^0 and C_X^- are the concentrations of neutral and negatively charged point defects, respectively, and n is the electron concentration.

Since the constant is a function of temperature only, we can write for the intrinsic case [13, 31],

$$\frac{(C_X^0)_i n_i}{(C_X^-)_i} = K^*(T) \tag{2.7b}$$

where $(C_X^0)_i$ and $(C_X^-)_i$ are the concentrations of the neutral and negatively charged point defects under intrinsic conditions, respectively, and n_i is the intrinsic carrier concentration. Equating equations 2.7a and 2.7a and noting that the concentration of neutral point defects does not change with doping ($C_X^0/(C_X^0)_i = 1$) [13, 31] we find,

$$\frac{C_X^-}{(C_X^-)_i} = \left(\frac{n}{n_i}\right) \tag{2.7c}$$

Similar treatment can be applied to the doubly negatively charged point defect,

$$X^- + e^- \Leftrightarrow X^{--} \tag{R2.5}$$

$$\frac{C_X^{--}}{(C_X^{--})_i} = \left(\frac{n}{n_i}\right)^2 \tag{2.7d}$$

where C_X^{--} is the concentration of the doubly negatively charged point defect and $(C_X^{--})_i$ is the concentration of the defect under intrinsic conditions.

From equations 2.7c and 2.7d it is clear that with increasing n-type doping the concentration of negatively charged defects will increase. Using the same principle it is a simple matter to show that the concentration of positively charged defects decreases with increasing electron concentration, i.e.,

$$\frac{C_X^{+}}{(C_X^{+})_i} = \left(\frac{n_i}{n}\right) \tag{2.7e}$$

The concentration of charged point defects depends on the position of the Fermi level while that of the neutral defects is independent of the doping level. The total concentration of point defects (charged plus neutral) thus changes with the Fermi level.

2.4 Defect Mediated Dopant Diffusion Equations

In the 1960s, researchers found increased self-and impurity diffusion coefficients in *Si* under extrinsic conditions [38, 39] that could not be explained with a simple field enhancement factor. Moreover, the increase in diffusion coefficients over their intrinsic values was consistent with the form, $D_{ext} = D_{int}\left(n/n_i\right)^m$ *or* $D_{ext} = D_{int}\left(p/n_i\right)^m$ [40]. Since it was known that the concentration of charged point defects would increase over its intrinsic value with the ratio$\left(n/n_i\right)^m\{or\ \left(p/n_i\right)^m\}$, Masters and Fairfield [40] stated that to a first approximation the diffusivity of the dopant should scale with point defect concentration and that S. M. Hu [41] in 1968 had found this mathematical form to be feasible.

A theoretical approximation of extrinsic diffusivity of dopants is given by [13, 31],

$$D_{ext}^{eff} = D_i^{AX^{++}}\left(\frac{n_i}{n}\right)^2 + D_i^{AX^{+}}\left(\frac{n_i}{n}\right) + D_i^{AX^{0}} + D_i^{AX^{-}}\left(\frac{n}{n_i}\right) + D_i^{AX^{--}}\left(\frac{n}{n_i}\right)^2 \quad (2.8a)$$

$D_i^{A^+X^m}$ is known as the diffusivity of the dopant, $A^{\pm}$, due to pairing with X^m under intrinsic conditions.

Since point defect concentrations do not change under intrinsic doping conditions, intrinsic diffusivities are independent of the doping level. Intrinsic diffusivity is given by [13, 30],

$$D_i^{eff} = D_i^{AX^{++}} + D_i^{AX^{+}} + D_i^{AX^{0}} + D_i^{AX^{-}} + D_i^{AX^{-}} \quad (2.8b)$$

Experimentally one determines D_{ext}^{eff} and D_i^{eff} under extrinsic and intrinsic conditions, respectively.

A mathematical proof of equation 2.8a for the case of dopant diffusion appeared later in 1989 in Fahey *et al.* review [31]. In the context of this thesis the proof of equation 2.8a is important rather than the final result (equation 2.8a) itself. This is because the diffusion model discussed in chapter 4 is derived using the same principles and approximations as has been done in deriving equation 2.8a but the final diffusivity equations are different. This difference arises due to non-equilibrium effects during P diffusion, as has been discussed in section 4.3. The current section is limited to the conventional derivation of equation 2.8a, which can be found in references [13] and [31]. The proof is shown from the point of view of phosphorus diffusion, which is the subject of this thesis. By analogy, the same applies for other substitutional dopants. It begins with a simple treatment of the pairing reaction between the dopant and a point defect with charge $-m$,

$$P^+ + X^{-m} \Leftrightarrow P^+X^{-m} \quad (R2.6)$$

where $-m$ is the charge on the point defect.

Diffusion is a nonequilibrium process. However, local equilibrium (*) between P^+, X^{-m} and the pairs P^+X^{-m} is thought to exist throughout the diffusion field if there are no additional sources of point defects and if a mass action relation between P^+, X^{-m} and the pairs P^+X^{-m} persists,

$$\frac{C_P^+ C_{X^{-m}}}{C_{P^+X^{-m}}} = K^*(T) \tag{2.9}$$

where $C_{P^+X^{-m}}$ is the concentration of the dopant defect pair in charge state $(1-m)$.

By taking the derivative of equation 2.9 it can be shown that [13, 31, 42],

$$\frac{\partial C_{P^+X^{-m}}}{\partial x} = \frac{C_{P^+X^{-m}}}{C_P^+}\frac{\partial C_P^+}{\partial x} + \frac{C_{P^+X^{-m}}}{C_X^{-m}}\frac{\partial C_X^{-m}}{\partial x} \tag{2.10}$$

The resultant flux of the pair is then just the product of the pair diffusivity, $d_{P^+X^{-m}}$, and the gradient in its concentration,

$$J_{P^+X^{-m}} = -d_{P^+X^{-m}}\frac{\partial C_{P^+X^{-m}}}{\partial x} \tag{2.11a}$$

$$= -d_{P^+X^{-m}}\frac{C_{P^+X^{-m}}}{C_P^+}\frac{\partial C_P^+}{\partial x} - d_{P^+X^{-m}}\frac{C_{P^+X^{-m}}}{C_{X^{-m}}}\frac{\partial C_{X^{-m}}}{\partial x}$$

Under intrinsic conditions when the gradient in the point defect concentration is zero, equation 2.11a reduces to [13, 31, 42],

$$(J_{P^+X^{-m}})_i = -d_{P^+X^{-m}}\frac{(C_{P^+X^{-m}})_i}{C_P^+}\frac{\partial C_P^+}{\partial x} \tag{2.11b}$$

According to Fick's first law the flux is just the negative product of the diffusion coefficient and the gradient in dopant concentration. It then follows that the dopant diffusivity under intrinsic conditions is [13, 31, 42],

$$D_{(P^+X^{-m})_i^*} = -d_{P^+X^{-m}}\frac{(C_{P^+X^{-m}})_i}{C_P^+} \tag{2.12}$$

Equation 2.12 is an important result. $D_{(P^+X^{-m})_i^*}$ is understood to be the diffusivity of P^+ via interactions with the point defect X^{-m} under equilibrium (*) and intrinsic conditions [13, 31, 42].

The total flux of dopant defect pairs (or of phosphorus) is the sum of Fickian flux (diffusion) and the flux due to drift [13, 31, 42],

$$J_{P^+X^{-m}} = -d_{P^+X^{-m}} \frac{\partial C_{P^+X^{-m}}}{\partial x} + (1-m)\mu_{P^+X^{-m}} C_{P^+X^{-m}} \vec{E} \qquad (2.13)$$

where $\mu_{P^+X^{-m}}$ is the mobility, $\vec{E}$ is the electric field that arises due to a gradient in the potential (electron concentration) and is $(1-m)$ the net charge of the pair P^+X^{-m}.

The pair diffusion model uses the Boltzmann's approximations, i.e. [13, 30, 41],

$$C_P = C_P^+ = n \qquad (2.14a)$$

$$E = -\frac{\partial \phi}{\partial x} = -\frac{KT}{q}\frac{\partial [ln(n/n_i)]}{\partial x} = -\frac{KT}{q}\frac{n_i}{n}\frac{\partial (n/n_i)}{\partial x} = -\frac{KT}{qC_P^+}\frac{\partial C_P^+}{\partial x} \qquad (2.14b)$$

It was pointed out earlier that $C_P = C_P^+ = n$ will hold at diffusion temperatures and heavy doping. The first condition above, equation 2.14a, is then not exactly due to the Boltzmann approximation as is often noted [13, 31]. Nonetheless, using assumptions 2.14a and 2.14b and inserting equation 2.10 in equation 2.13, the flux equation becomes,

$$J_{P^+X^{-m}} = -d_{P^+X^{-m}} \frac{C_{P^+X^{-m}}}{C_P^+}\frac{\partial C_P^+}{\partial x} - d_{P^+X^{-m}} \frac{C_{P^+X^{-m}}}{C_{X^{-m}}}\frac{\partial C_{X^{-m}}}{\partial x} \qquad (2.15)$$

$$- (1-m) d_{P^+X^{-m}} C_{P^+X^{-m}} \frac{\partial [ln(n/n_i)]}{\partial x}$$

where the Einstein relationship ($\mu_{P^+X^{-m}} = q d_{P^+X^{-m}} / KT$) has been used for mobility,

Diffusivity analysis from experimental studies have suggested that under equilibrium conditions the concentration of dopant defect pairs scales with the concentration of point defects [31],

$$\frac{C_{P^+X^-}}{(C_{P^+X^-})_i} = \frac{C_X^-}{(C_X^-)_i} = \left(\frac{n}{n_i}\right) \tag{2.16a}$$

$$\frac{C_{P^+X^{--}}}{(C_{P^+X^{--}})_i} = \frac{C_X^{--}}{(C_X^{--})_i} = \left(\frac{n}{n_i}\right)^2 \tag{2.16b}$$

Equilibrium conditions refer to the case when there are no additional sources or sinks for point defects. In such situations, point defect concentrations will scale with temperature and the Fermi level. Non-equilibrium point defect concentrations can arise due to ion implantation, oxidation, nitridation, etc. The current understanding is that approximations 2.16a and 2.16b do not hold under some non-equilibrium conditions [31]. This will be elaborated upon in chapter 4. Nevertheless, the assumption limits the use of equation 2.8a for the case of point defect equilibrium.

The gradient in the point defect concentration is given by,

$$\frac{\partial C_{X^{-m}}}{\partial x} = m(C_{X^{-m}})_i \left(\frac{n}{n_i}\right)^m \frac{\partial[ln(n/n_i)]}{\partial x} \tag{2.17}$$

Substituting equations 2.16a, 2.16b and 2.17 in the flux equation 2.15 we have,

$$\begin{aligned} J_{P^+X^{-m}} = & -d_{P^+X^{-m}} \frac{(C_{P^+X^{-m}})_i}{C_P^+} \left(\frac{n}{n_i}\right)^m \frac{\partial C_P^+}{\partial x} \\ & - m d_{P^+X^{-m}} \frac{(C_{P^+X^{-m}})_i}{(C_{X^{-m}})_i} (C_{X^{-m}})_i \left(\frac{n}{n_i}\right)^m \frac{\partial[ln(n/n_i)]}{\partial x} \\ & - (1-m) d_{P^+X^{-m}} (C_{P^+X^{-m}})_i \left(\frac{n}{n_i}\right)^m \frac{\partial[ln(n/n_i)]}{\partial x} \end{aligned} \tag{2.18a}$$

$$\begin{aligned} J_{P^+X^{-m}} = & -d_{P^+X^{-m}} \frac{(C_{P^+X^{-m}})_i^*}{C_P^+} \left(\frac{n}{n_i}\right)^m \frac{\partial C_P^+}{\partial x} \\ & - d_{P^+X^{-m}} \frac{(C_{P^+X^{-m}})_i^*}{C_P^+} C_P^+ \left(\frac{n}{n_i}\right)^m \frac{\partial[ln(n/n_i)]}{\partial x} \end{aligned} \tag{2.18b}$$

$$J_{P^+X^{-m}} = -d_{P^+X^{-m}} \frac{(C_{P^+X^{-m}})_i^*}{C_P^+} \left(\frac{n}{n_i}\right)^m \frac{\partial C_P^+}{\partial x} \tag{2.18c}$$

$$- d_{P^+X^{-m}} \frac{(C_{P^+X^{-m}})_i^*}{C_P^+} \left(\frac{n}{n_i}\right)^m \frac{\partial C_P^+}{\partial x}$$

$$J_{P^+X^{-m}} = -2D_{(P^+X^{-m})_i^*} \left(\frac{n}{n_i}\right)^m \frac{\partial C_P^+}{\partial x} \tag{2.18d}$$

where the factor of 2 is the field enhancement factor, h, for $C >> n_i$. Equation 2.18b is often solved [13, 31] in a different manner to introduce h directly into the flux equation,

$$J_{P^+X^{-m}} \tag{2.19a}$$

$$= -D_{(P^+X^{-m})_i^*} \left(\frac{n}{n_i}\right)^m \frac{\partial C_P^+}{\partial x} - D_{(P^+X^{-m})_i^*} C_P^+ \left(\frac{n}{n_i}\right)^m \frac{\partial [ln(n/n_i)]}{\partial x}$$

For the case of extrinsic doping when $C_P \gg n_i$, it can be shown that,

$$\frac{\partial [ln(n/n_i)]}{\partial x} \sim \frac{1}{2n_i} \left[\left(\frac{C_P^+}{2n_i}\right)^2 + 1\right]^{-1/2} \frac{\partial C_P^+}{\partial x} \tag{2.19b}$$

The flux equation now becomes,

$$J_{P^+X^{-m}} = -D_{(P^+X^{-m})_i^*} \left(\frac{n}{n_i}\right)^m \frac{\partial C_P^+}{\partial x} \left\{ 1 \right. \tag{2.19c}$$

$$\left. + \frac{C_P^+}{2n_i} \left[\left(\frac{C_P^+}{2n_i}\right)^2 + 1\right]^{-1/2} \right\}$$

The term $\left\{1 + \frac{C_P^+}{2n_i} \left[\left(\frac{C_P^+}{2n_i}\right)^2 + 1\right]^{-1/2}\right\}$ is simply the field enhancement factor.

$$J_{P^+X^{-m}} = -hD_{(P^+X^{-m})_i^*} \left(\frac{n}{n_i}\right)^m \frac{\partial C_P^+}{\partial x} \tag{2.19d}$$

Equations 2.18d and 2.19d are the pair diffusion equations under equilibrium conditions. The extrinsic diffusivity given in equation 2.8a can now be understood to arise from the flux equation, i.e.,

$$J_{P^+X^{-m}} = -hD_{ext}^{eff}\frac{\partial C_P^+}{\partial x} \tag{2.20}$$

where $D_{ext}^{eff} = D_{\left(P^+X^{-m}\right)_i^*}\left(\frac{n}{n_i}\right)^m$

2.5 High Concentration Phosphorus in-diffusion (HCPD)

Phosphorus diffusion in *Si* received considerable attention prior to 1980. In the early years of silicon integrated circuits (ICs), phosphorus was the primary dopant to form diffused junctions. Later arsenic replaced phosphorus as the preferred diffusant since it diffused more slowly and was therefore more controllable. Nonetheless, the advent of ion implantation in early 1980s regenerated interest in the study of phosphorus diffusion. Most of these studies [9, 43, 44, 45] were purely of academic interest and were aimed to address the controversies pertaining to P diffusion that had arisen as a result of the Fair & Tsai model [15].

The 1977 model of Fair [15] had some theoretical shortcomings and was inconsistent with several experimental findings. It therefore received widespread criticism from the research community [9, 43, 44, 45, 46, 47]. From a scientific point of view, the model is regarded incorrect. For a detailed critical review of the model, the reader is referred to the review of Hu *et al.* [44]. However, if the purpose is either ease of implementation and/or simulation accuracy, then the Fair & Tsai model [15] is still the best available P diffusion model. For the industrial practises of the time that required relatively deep junctions and high thermal budgets, the model of Fair was able to achieve reasonable simulation accuracies over a wide a range of processing conditions with a well-defined and limited set of fitting parameters

which, to date, no other P diffusion model has been able to demonstrate. It is pertinent to mention that even the Fair model [15] is not accurate enough for the shallow emitter profiles of solar cells. In addition, one still has to experimentally determine the surface electron concentration and assume that it is fixed throughout the diffusion process.

New investigations began into P diffusion after the advent of ion implantation in 1980. In the 1980s and early 1990s, significant advances in the understanding of P diffusion were made and several diffusion models were proposed. However, none of these models were able to demonstrate accurate modelling of P diffusion over a wide range of processing conditions and interest of the research community was slowly shifting from P diffusion studies. By the mid 1990s, interest in P diffusion modelling died out. At the time, modelling of some high concentration effects during arsenic diffusion was becoming important and experimental evidence for these effects had also previously been reported for phosphorus. Therefore, the models aimed at explaining high concentration effects in arsenic also attempted to explain these effects in phosphorus, thereby furthering the understanding of HCPD.

Recently, phosphorus diffusion has regained interest of the research community due to its use in forming solar cell emitters but very little work has been done to address the fundamental issues that have persisted in modelling the process. These studies attempt to tailor the diffusion recipe to give optimum solar cell performance with little emphasis on diffusion modelling and the actual diffusion mechanisms. In the following subsections, the different features of high concentration P in-diffusion and the simultaneous modelling of these features are discussed.

2.5.1 The electrically active phosphorus profile

The study of high concentration P diffusion modelling has primarily remained limited to that of the mobile (electrically active) specie. As early as the first study on the subject by Tannenbaum in 1962 [38], it was thought that all of the inactive P is in a precipitated phase and is immobile. The diffusion mechanisms of phosphorus were therefore studied by

analysing the diffusion behaviour of the mobile species. A simulated profile of the electrically active P, as one would obtain after in-diffusion from a high concentration surface source, is shown in Figure 7 as an example for illustration purposes.

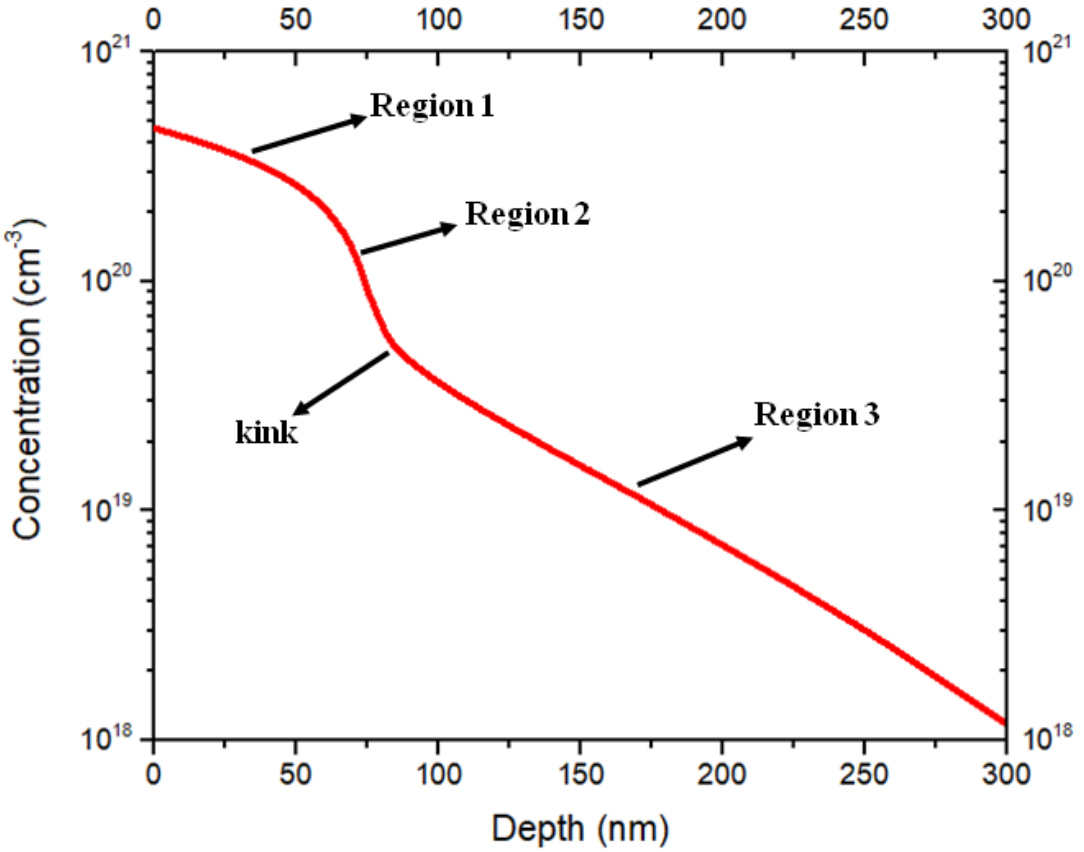


Figure 7: Simulated electrically active *P* profile for process 6 as listed in Appendix A (890 °C, 14.25 mins) as obtained in this work. Region 1 is also referred to as the plateau region. Intersection between regions 2 & 3 is referred to as the kink.

Early studies on P diffusion had found that the plateau in the HCPD profile (Region 1) might only be explained [15, 48, 49, 50, 51, 52, 53] with a quadratic dependence of diffusivity on the electron concentration, i.e. $(n/n_i)^2$. These studies had used surface in-diffusion methods ($POCl_3$ and SiP powders) and the $(n/n_i)^2$ dependence was determined using the Boltzmann-Matano (BM) analysis, wherein the surface concentration is assumed to be a constant throughout diffusion. Such assumptions are erroneous, as will be discussed in section 4.2.

Since in the 1970s dopant diffusion was thought to only take place via interactions with vacancies (due to the very high estimates at that time for the formation energy of a silicon self interstitial [31]), these early diffusion models assumed P diffusion to be mediated by the

doubly negatively charged vacancy (V^{--}) in region 1 to account for the $(n/n_i)^2$ dependence of diffusivity. In addition, several authors [15, 54, 55] had reported the diffusion coefficient of P under intrinsic conditions and it was postulated that the diffusion mediating species in this case is the neutral vacancy (V^0) [15]. Later experimental evidence of an interstitial assisted diffusion mechanism for P under intrinsic conditions [56] (and in the tail region [45] of HCPD profiles) raised serious doubts regarding the validity of these early diffusion models.

In 1984, while examining the wafer bulk (regions several microns deep and away from the diffused emitter) of specimens that had undergone HCPD, Fahey *et al.* [45] found that boron (antimony) layers buried several microns deep within the wafer experienced an enhancement (retardation) in intrinsic diffusivity of more than one order in magnitude. The enhancement in boron diffusivity suggested an interstitial supersaturation ($S_I = C_I/C_I^*$, where the asterisk denotes equilibrium) of more than one order in magnitude while the retardation in antimony diffusivity suggested a corresponding vacancy undersaturation in accordance with the steady state relation,

$$C_I C_V = C_I^* C_V^* \tag{2.21}$$

Fahey *et al.* [44] also reported that the diffusion coefficient in the P tail (region 3) had increased by a similar magnitude (more than one order in magnitude) over the intrinsic diffusion coefficient of P. Their work suggested that P diffuses via interstitials under intrinsic conditions (later to be confirmed by oxidation and nitridation experiments [56, 57]) and that when P diffusion is carried out at high concentrations the interstitial concentration is in supersaturation in the tail region, resulting in a significant enhancement in the tail diffusivity. In addition, the supersaturation extends deep within the wafer (since point defects diffuse rapidly as compared to dopants) and is responsible for the emitter push effect [44] (enhancement in diffusivity of the boron base) that is observed during P diffusion.

Regarding the source of excess self-interstitials, it was argued on the basis of carefully designed experiments [44] that surface oxidation, precipitation and injection (displacement) of interstitials (silicon atoms by phosphorus) at the surface had no role in the generation of excess self-interstitials. It was therefore postulated that the only possible explanation of the excess interstitials was the reverse kick-out reaction in the bulk wherein a phosphorus atom knocks a silicon atom into an interstitial site and itself becomes substitutional. That is to say, that excess self-interstitial generation is not a surface phenomenon; it is rather a bulk phenomenon, which is inherent to the process.

In the following years, several theoretical attempts [58, 59, 60] were made in order to better explain the role of point defects in P diffusion. According to these studies, phosphorus interstitial pairs form at the *Si* surface and diffuse into the wafer bulk, wherein the pair dissociates resulting in the release (and therefore generation) of excess *Si* self interstitials that then diffuse into the wafer bulk and towards the surface. The *Si* surface would, as per the authors, act as an infinite sink for the excess interstitials thereby maintaining point defect equilibrium at the surface. Moreover, by virtue of the rapid interstitial diffusivity, this point defect equilibrium would not be limited to the *Si* surface only, and would rather extend to depths corresponding to the plateau depth. A graph of the theoretically proposed interstitial and vacancy profiles is shown in Figure 8 [58].

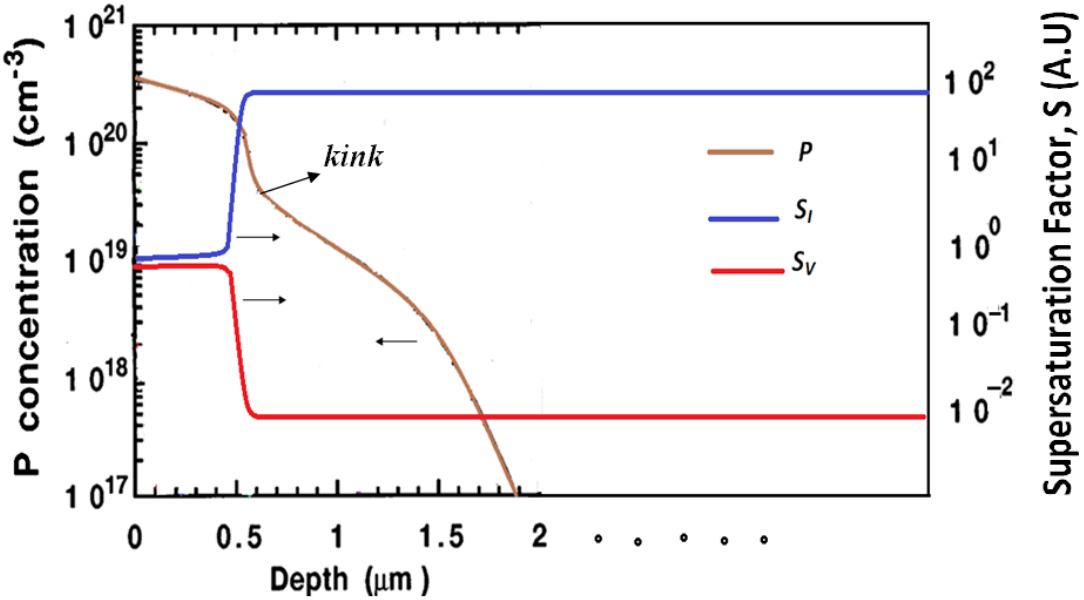


Figure 8: Theoretical depiction of P, S_I (interstitial supersaturation) and S_V (vacancy undersaturation) profiles in *Si* after in-diffusion from a surface source [58].

These early theoretical studies were instrumental in shaping the opinion that the concentrations of point defects in region 1 are in equilibrium. Since the sudden drop in diffusivity observed from region 3 to region 2 could best be explained by a rapidly vanishing interstitial supersaturation close to the kink (intersection of regions 2 & 3), it then seemed reasonable that point defect concentrations, in moving from region 3 to region 1, acquire close to equilibrium values somewhere in region 2. However, these early models were in contradiction with the experimental findings of Fahey *et al.* [45], in that they suggested the Si surface (as opposed to the wafer bulk) to be the source of the excess self interstitials.

In the following decades, several P diffusion models [46, 47, 60, 61] were proposed. These models were, in one way or another, inspired by the point defect concentration models [58, 59, 60] that have been discussed above and illustrated in Figure 8 [58]. However, these models have not been successful in accurately modelling P diffusion over a wide range of processing conditions. In addition, most of these models [46, 60, 61] require a large number of fitting parameters and have many unknown constants.

Accurate P diffusion modelling of solar cell emitters in the three regions is complicated due to several factors. First, the simplified approach of equation 2.8a is not able to capture the

rapid decrease in diffusivity in region 2. Using positively charged defects in equation 2.8a will result in a decrease in diffusivity with increasing n, however, the shape of the profile in the tail region will be affected considerably and a rapid decrease in diffusivity at the kink concentration can still not be achieved. On the other hand, a similar problem arises when one resorts to complex treatments where the actual concentration of point defects is taken into account. In such cases, additional IV recombination processes are required to account for the rapidly changing point defect concentrations in region 2. However, the associated changes in recombination rates with doping level will also affect the diffusion profile in regions 1 & 3. Secondly, the quadratic dependence $(n/n_i)^2$ does not predict a diffusion coefficient in region 1 that is rapid enough to account for the plateau in the electrical profile. Further, the quadratic dependence does not allow for a sudden decrease in diffusivity at the intersection of regions 1 & 2. Lastly, the diffusion coefficient in the tail region is not a constant and its dependence on the electron concentration is complex [47].

A serious problem with the diffusion models previously proposed [46, 59, 60, 61] is that they do not offer sufficient simplification of the continuity equations for dopant, defect and dopant defect pair concentrations. Since during P diffusion the defect concentrations are not in equilibrium throughout the diffusion profile these models use the actual point defect (instead of the relative to intrinsic) concentrations in order to simulate a more realistic coupling between impurity atoms and point defects. The concentration profile of point defects is simultaneously simulated and the transport governing equations require a large number of fitting parameters for the concentrations and diffusivities of point defects and dopant defect pairs in the different charged states. Given that the point defect concentrations are highly debated, these models have many unknown parameters. In addition, these models do not give a set of constants (activation energies and pre-exponential factors) for the determination of model fitting parameters for various temperatures (using Arrhenius expressions) and have, therefore, little practical applicability.

In 1982, when P diffusion was still considered to be mediated by vacancies only, Mathiot and Pfister [33] suggested a vacancy percolation effect to take place during HCPD. They noted that if the dopant concentration rises significantly, a dopant atom, *P2*, might be located on the 5th nearest neighbour site to another dopant atom, *P1*, which is already paired with a vacancy, Figure 9 [32]. In this case, the third nearest neighbour site (site *A*) from *P1* is also a second nearest neighbour site from *P2*. In such a situation then, as per Mathiot & Pfister, the vacancy will need not to return via a different path for dopant *P1* but instead it will move towards dopant *P2* and exchange lattice sites with it. That is to say, that the transition from site *B* to site *A* is energetically favourable since site *A* is also a second nearest neighbour site. If large number of dopants are connected in this way, a vacancy will simply percolate through the structure and the effect is an increase in the diffusivity of the vacancy and the dopant.

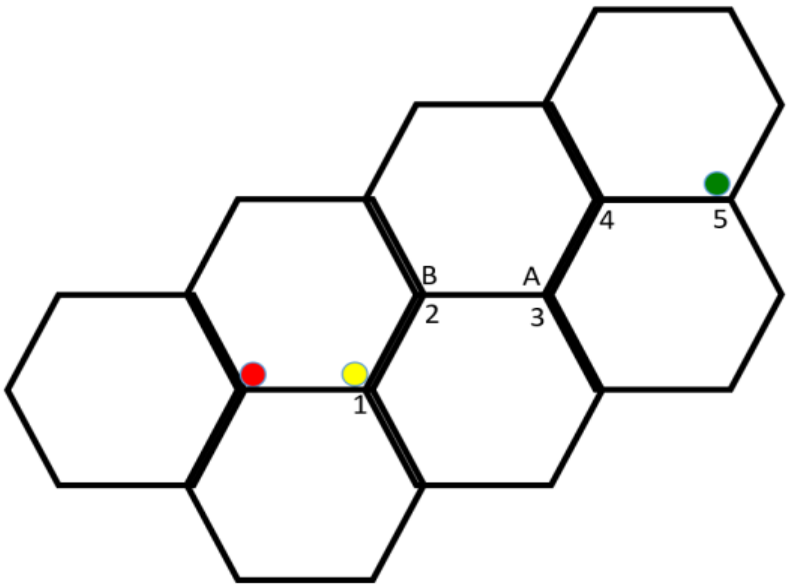


Figure 9: [33] The vacancy (yellow) will move from B (second coordination site from dopant P1, red) to A (second coordination site from dopant P2, green) and percolate through the structure.

The authors had suggested a donor threshold concentration ($3 \times 10^{20} cm^{-3}$) above which the percolation effect takes place, thereby explaining the rapid increase in diffusivity above the threshold concentration. The vacancy percolation theory was, as per the authors, able to explain the fast diffusivity in the plateau region and the slow diffusivity in the rapidly falling

region (region 2). The diffusion mechanism in both regions was the vacancy mechanism, but in region 1, the diffusivity enhanced significantly due to the percolation effect.

Despite the fact that the percolation theory was first developed to explain the P profile in regions 1 & 2 and despite the fact that the percolation theory would later go on to gain widespread acceptance in the study of most n-type dopants in *Si* and germanium, it has remained largely ignored in the study of P diffusion modelling. For example, the models of Jaeger [60], Dunham [46], Uematsu [61] and Bentzen [47] ignored vacancy percolation. One reason might be that at the time of the vacancy percolation paper a vacancy only diffusion mechanism had become highly controversial. However, a more significant factor was that the suggestion that the percolation effect could explain the profile shape in both regions 1 & 2 (without any need of resorting to changes in the equilibrium concentration of point defects) was quite optimistic.

Mathiot & Pfister demonstrated the ability of the percolation effect in simulating the profile shape in both regions (1 and 2) for only a certain experimental profile obtained at 1000 °C. Over a wider range of processing conditions, the percolation effect might only be able to explain the very rapid diffusivity in region 1, where the quadratic dependence of diffusivity on the electron concentration $\left({}^{n}/_{n_i}\right)^2$ is not sufficient to account for the plateau in the electrical profile. This is because at very high doping levels isoconcentration studies of vacancy diffusers like antimony and arsenic in n-type silicon and germanium wafers [62] have suggested the diffusivity to scale with the form $\left({}^{n}/_{n_i}\right)^4$.

In 1994 Dunham *et al.* [33] developed an atomistic theory of donor diffusion via vacancies. The authors validated their theory using lattice Monte-Carlo simulations based on the percolation theory. As per this model the effective dopant vacancy pair diffusivity can be expressed as [63],

$$D_{eff} = D^{/}\left[1 + \left(\frac{C_P^+}{C^*}\right)^m\right] \tag{2.22}$$

where $D^{/}$ is the diffusivity of the dopant vacancy pair when the vacancy interacts with only one dopant and D_{eff} is the diffusivity of the pair when the vacancy interacts with m number of dopant atoms in its vicinity. C^* is a concentration above which the diffusivity enhances significantly due to vacancy percolation. The Dunham percolation model has found widespread use in the study of arsenic diffusion and equation 2.22 is now known as the power law model.

Section 4.3 discusses a P diffusion model that, is consistent with previous experimental findings, requires a small set of well-defined fitting parameters, is derived from first principles using a simplified approach and is able to accurately model P diffusion over a wide range of processing conditions. The proposed diffusion model is thus able to overcome the shortcomings of previous models.

2.5.2 Inactive Phosphorus: precipitation, solubility & modelling

In 1982, Nobili *et al.* [9] using TEM (transmission electron microscopy) observations reported that all of the electrically inactive P forms precipitates. The authors also pointed out that under equilibrium conditions, acquired after prolonged anneals, the concentration level of the plateau in the electrical profile corresponded to the solubility limit, which is a function of temperature only. These authors demonstrated that the thermal history of the process would determine the plateau concentration and that the electrically active phosphorus could easily acquire concentrations exceeding the solubility limit. Their work not only clarified the discrepancies in the reported [10, 15, 38] active P levels but also explained the very high donor (higher that solubility) concentrations that are often observed after the relatively short $POCl_3$ diffusion process [15].

In order to account for the thermal history and inactive P, a dopant precipitation model was required that would take into account the growth and dissolution of precipitates of different sizes. In 1995, Dunham [64] developed a general kinetic precipitation model and validated his model for phosphorus and arsenic using the data of Nobili *et al.* [9, 65]. In the following subsections, the Dunham precipitation model is discussed. Also discussed is the proposed new solubility limit of P by Solmi *et al.* [66].

2.5.2.1 Physics of Precipitation

When the solute concentration within a matrix becomes high enough, the formation of a separate solute-rich phase can lower the system's overall free energy. The addition of a phosphorus atom to a growing precipitate changes the free energy of the system by an amount [64, 67, 68, 69], ΔG,

$$\Delta G_u = -uKTln\left(\frac{C_P^+}{C_{SS}}\right) + \Delta G_u^{excess} \tag{2.23}$$

where u represents the size of the precipitate (i.e. precipitate comprising of u phosphorus atoms), C_{SS} is the solubility limit and ΔG_u^{excess} is the excess energy which incorporates the effect of precipitate/matrix interface and strain energies on the free energy. The more general form of equation (1) uses the mobile solute concentration instead of C_P^+ (electrically active phosphorus). Therefore, equation 2.23 assumes that all of the electrically inactive P precipitates and is immobile [64]. This is a reasonable assumption and previously in section 2.3 I alluded to this fact by mentioning that at high doping levels all of the dopant is ionized (except for dopant atoms that are in precipitates). Complete ionization of substitutionally dissolved P occurs at high doping levels due to the screening effect. In addition, complete ionization is also expected to occur at diffusion (high) temperatures due to the shallow donor level of P. Moreover, only negligible concentrations of P atoms in interstitials sites are expected because, as was pointed out in section 2.2, P dissolves predominantly on substitutional sites.

The first term in equation 2.23 is the free energy change due to the driving force for phase transformation. When the solute (mobile or electrically active phosphorus) concentration is greater (less) than C_{SS}, the first term in equation is negative (positive) and there is a driving force for precipitates to grow (shrink).

An expression of the form given in equation 2.24 for the excess energy has been suggested by Dunham [64].

$$\Delta G_u^{excess} = a_1 u^{m_1} + a_2 u^{m_2} + a_3 u^{m_3} + \cdots \quad (2.24)$$

where a_1, a_2, a_3, m_1,m_2 and m_3 are constants. The first term in equation 2.24 accounts for the contribution of matrix/precipitate interface energy to the overall excess energy ($m_1 = 2/3$ for spherical precipitates). All other terms modify the behaviour of excess energy due to changes in strain relaxation and point defect interactions for small sized precipitates. Usually only the first three terms (with $m_2 = 1/3$ and $m_3 = -1$) are used to account for the change in excess energy associated with small sizes [64, 67, 68, 69].

In the following, determination of the growth and dissolution of precipitates using the kinetic rate equations is discussed. These rate equations allow one to determine the concentration of precipitates of all sizes, from u equal 2 to ∞.

2.5.2.2 Kinetic Rate Equations

Precipitates grow and shrink by the addition or dissolution of single solute atoms (ionized mobile phosphorus atoms),

$$E_{u-1} + P^+ \Leftrightarrow E_u \quad (R2.7)$$

where E_u is a cluster containing u solute atoms.

The change in concentration of precipitate of size u can be computed using the method outlined in references [64, 67, 68, 69],

$$\frac{\partial f_u}{\partial t} = R_{u-1} - R_u \qquad (u = 2 \ldots \infty) \tag{2.25}$$

where f_u is the concentration of precipitate of size u and R_u is the net growth rate of precipitates from size u to $u+1$. R_u takes into account the growth (dissolution) from size u ($u+1$) to $u+1$ (u). It is given by,

$$R_u = g_u f_u - d_{u+1} f_{u+1} \tag{2.26}$$

where $g_u$and $d_u$are the growth (from size u to $u+1$) and dissolution (from size u to $u-1$) rates, respectively. Therefore, equation gives the change in concentration of a precipitate of size u due to its net growth into precipitate of size $u+1$ and due to the net growth of precipitate of size $u-1$ into precipitate of size u.

The solute is involved in the growth of precipitates of all sizes. The change in concentration of the solute is given by [64],

$$\frac{\partial C_P^+}{\partial t} = -2R_1 - \sum_{u=2}^{\infty} R_u \tag{2.27}$$

A precipitate of size u ($u > 1$) grows into size $u+1$ by the addition of a solute atom to the size u precipitate. By the same analogy, the precipitate of size 1 grows into size 2 by the addition of a solute atom (size 1 precipitate) to a size 1 precipitate. The coming together of the two size 1 precipitates accounts for the factor of two in equation 2.27.

The growth rate is given by [69],

$$g_u = D\lambda_u C_P^+ \tag{2.28}$$

where D is the diffusion coefficient of the solute and a diffusion limited growth approximation (from Ham [70]) is used to determine the kinetic precipitation factor, λ_u, for a precipitate with effective radius, R_u^{eff},

$$\lambda_u \sim \frac{A_u}{R_u^{eff}} \tag{2.29a}$$

$$A_u = 4\pi\left(R_u^{eff}\right)^2 \tag{2.29b}$$

$$R_u^{eff} = r_u + b \tag{2.29c}$$

where b is the reaction distance taken as the atomic spacing (2.71 A^0). Assuming a spherical precipitate the radius is approximated as,

$$r_u = \left(\frac{3u}{4\pi C_{ppt}}\right)^{1/3} \tag{2.29d}$$

where C_{ppt} is the concentration of *P* inside a precipitate. It can be taken as half the silicon atomic concentration ($C_{ppt} = 2.5 \times 10^{22}\ cm^{-3}$) since the precipitates comprise both *P* and *Si* atoms.

A derivation for the dissolution rate can be found elsewhere [64, 67, 68, 69]. It is given by,

$$d_{u+1} = g_u \frac{C_{SS}}{C_P^+} exp\left(\frac{\Delta G_{u+1}^{excess} - \Delta G_u^{excess}}{KT}\right) \tag{2.30}$$

Using equation 2.24 to compute the excess energy allows one to find the dissolution rate from equation 2.30, provided the solubility limit is known. Using the generation and dissolution rates the net growth rate of precipitates, equations 2.26, and therefore the precipitate concentrations of various sizes, equation 2.25, can be computed.

2.5.2.3 Solid Solubility of Phosphorus

In 1996, Solmi *et al.* [66] reported a new solubility limit of *P* in *Si* that was higher than the maximum electrically active concentration. Solmi *et al.* implanted very heavy doses of *P* in *Si* and after thermal annealing of these specimens at different temperatures subjected the samples to secondary neutral mass spectroscopy (*SNMS*). From the shoulder in the resulting profiles Solmi *et al.* [66] determined the solubility limit. Since the concentration at the shoulder remained fixed with annealing time, it corresponded (as per Solmi *et al.* [66]) to the concentration at which the dopant is in equilibrium with the precipitates and with the free

dopant in the bulk. The dropping profile prior to the shoulder represented a region with low diffusivity and high precipitation.

In their paper Solmi *et al.* [66] also reported the discrepancy between the maximum electrically active phosphorus concentration n_{max} (previously known as the solubility limit) and what they referred to as the solubility limit. Their results are shown in Figure 10. Solmi *et al.* [66] suggested that the discrepancy can be explained by the presence of agglomerates, i.e. small clusters of phosphorus that form along with large rod like *SiP* precipitates [9, 71]. As discussed in section 4.5, agglomerates are electrically inactive and in the precipitation model of Dunham they count as small sized precipitates (u equal to a small number but greater than 1). Therefore, in that analysis the previously accepted solid solubility should be used and not the limit suggested by Solmi *et al* [66]. However, as noted in section 4.5, Solmi *et al* [66] were able to achieve the best experimental conditions for obtaining the true solid solubility limit (solute concentration in equilibrium with an infinitely large precipitate), which is given by the maximum electrically active P in Solmi *et al* [66] study (black curve in Figure 10). Therefore, the solubility limit to be used in the Dunham precipitation model [64] is the value of the maximum electrically active P in Solmi *et al* [66] study. This is discussed in section 4.5.

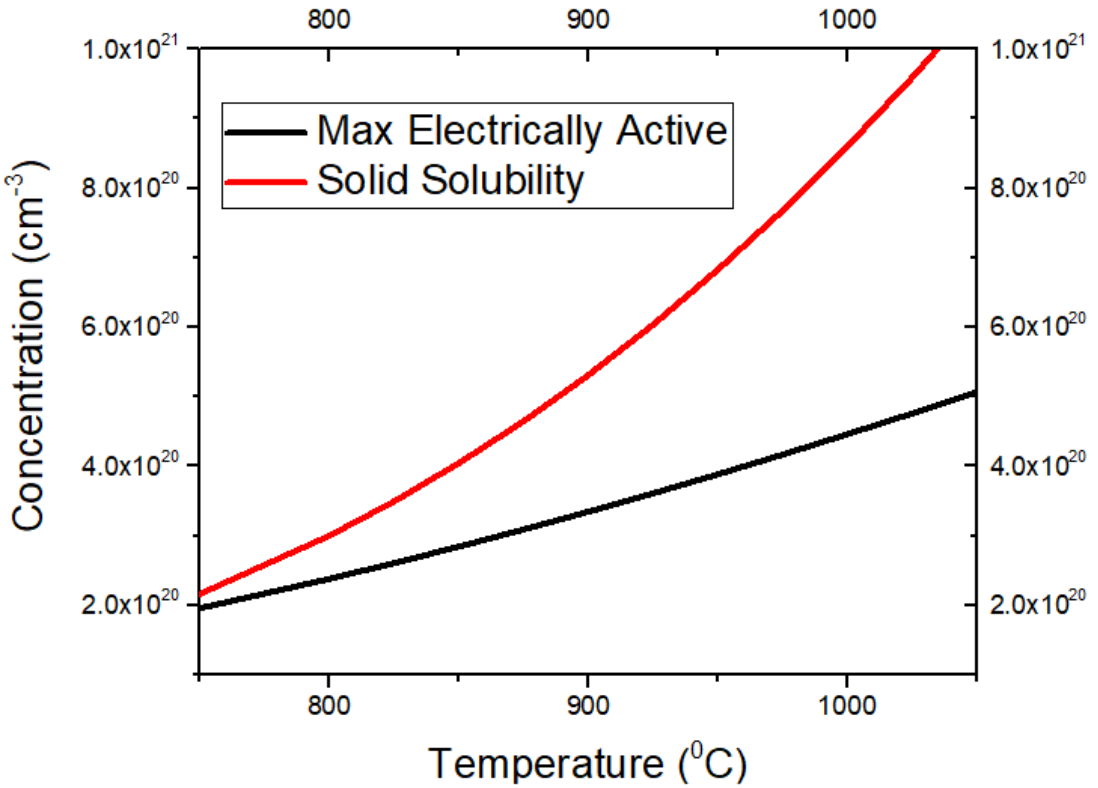


Figure 10: Solubility limit and maximum electrically active level of *P* as defined in [66] for the temperature range 750-1100 °C.

2.5.3 Summary of HCPD

Based on the discussion on previous studies in the above sections, the literature indicates that phosphorus diffuses via a dual diffusion mechanism. In region 3, the dominant mechanism for P diffusion is via interactions with *Si* self-interstitials. A supersaturation of interstitials significantly enhances diffusivity of P via interstitials over its equilibrium value. Some dopant assisted and/or direct *IV* annihilation processes are able to rapidly suppress the interstitial supersaturation at the kink, thereby restoring point defect equilibrium. In region 1, where point defect concentrations are in equilibrium, contribution of self interstitials to dopant diffusivity is negligible and diffusion in these regions is mediated by vacancies. The small diffusivity in region 2 is often explained using close to equilibrium point defect concentrations and insufficient electrons concentrations to account for the small interstitial and vacancy diffusivities, respectively.

Several considerations are important in the development of a P diffusion model. Since the Si surface has been experimentally ruled out [45] to have a significant role in the generation of excess self-interstitials during P diffusion, a P diffusion model must not assume interstitial injection at the surface as the source of excess interstitials. Instead, excess interstitial generation via the kick out reaction (which is the most likely reason for excess interstitials) should be taken into account. If so, the kick out reaction takes place throughout the diffusion profile and appropriate explanations must be provided for the complete suppression of the kick out reactions at concentrations exceeding the concentration level corresponding to the kink. Moreover, the IV annihilation processes required for the interstitial suppression should simultaneously allow accurate modelling in the tail region, where the diffusion coefficient has a complex dependence on the electron concentration.

A comprehensive P diffusion model should allow co-modelling of dopant precipitation and of P diffusion into the wafer bulk such that, very good agreement with experimental P profiles is observed over a wide range of processing conditions and with limited number of fitting parameters that could be determined using Arrhenius expressions. The model should therefore use a first principle approach and determine the donor precipitation flux and donor concentration gradient flux via an effective diffusivity for all the three regions.

CHAPTER 3
EXPERIMENTAL TECHNIQUES

Diffusion profiles, i.e. dopant concentration vs depth profiles, are required for a wide range of processing conditions in order to facilitate a study of high concentration phosphorus in-diffusion. Shallow emitters of commercial solar cells are typically formed in the temperature range 840-880 ºC. As discussed in section 1.5, the probable reason for this is to provide a balance between the electrically active and inactive P, without compromising sheet resistance uniformity. It was also pointed out in section 1.5 that emitters formed at high temperatures and small durations would contain lower concentrations of electrically inactive *P* since the high diffusion temperatures would allow significant diffusion depths within the short intervals, which are in turn required to ensure that the surface concentration does not rise considerably beyond the solubility limit throughout the process. The resulting total and electrically active P profiles are then expected to closely resemble the electrically active P profile of industrial emitters. Hence, in this work, the diffusion process was studied at relatively higher temperatures (865-968 ºC) that enable rapid formation of shallow emitters. In this chapter, the experimental techniques used to acquire diffusion profiles and the basis for their selection are presented.

3.1 Characterization Techniques

The characterization techniques used in this work were the 4-point probe and *SIMS* (secondary ion mass spectroscopy). 4 point probe was used for resistivity measurements on

wafers after diffusion while *SIMS* profiling was carried out on selected specimens for acquiring depth profiles.

3.1.1 Four Point Probe

The 4-point probe is used to measure resistivity of a semiconductor material. As shown in Figure 11 the apparatus comprises of four metal tips of finite radius [72]. Constant current is supplied through the outer two probes while voltage is measured across the inner two probes using a high impedance voltmeter.

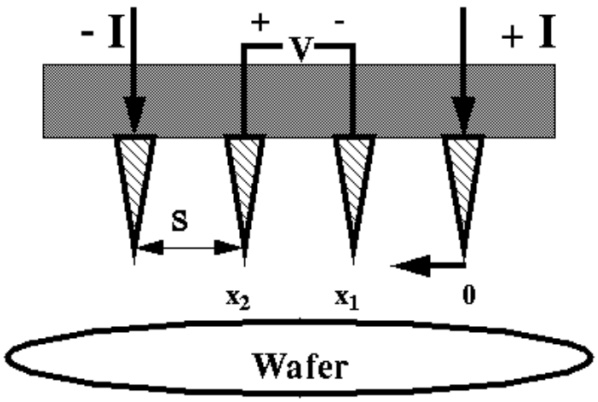


Figure 11: [72] Schematic of a four-point probe. The probe spacing is denoted by S. Inner probes at locations x_1 and x_2 measure voltage as current flows between the outer two probes.

For thin films where the film thickness, t, is very small compared to the probe spacing S, such as a diffused n+ emitter on a p-type substrate, one expects current rings emanating from the current probes instead of a spherical protrusion of current which will happen for bulk specimens. The differential resistance is given by,

$$\Delta R = \rho\left(\frac{dx}{dA}\right) \tag{3.1a}$$

where x is the lateral dimension along the wafer surface and ρ is the resistivity in units of Ω-cm. The area A of the protruding current rings is given by,

$$A = 2\pi xt \tag{3.1b}$$

The resistance R can then be determined by integrating equation 3.1a between the inner two probes,

$$R = \int_{x_1}^{x_2} \rho \frac{dx}{2\pi x t} = \int_{s}^{2s} \frac{\rho}{2\pi t} \frac{dx}{x} = \frac{\rho}{2\pi t} \ln(2) \tag{3.1c}$$

Also, current superposition at the two outer tips leads to the expression,

$$R = \frac{V}{2I} \tag{3.1d}$$

Equating equations 3.1c and 3.1d gives the expression for resistivity for a thin sheet,

$$\rho = \frac{\pi t}{ln2} \left(\frac{V}{I}\right) \tag{3.2a}$$

The commonly used parameter sheet resistivity, in units of Ω/□, is given by,

$$R_s = \frac{\rho}{t} = k \left(\frac{V}{I}\right) \tag{3.2b}$$

where k is the geometric factor with a value of 4.53 ($\pi/ln2$ from equation 3.2a) for a thin semi-infinite sheet.

3.1.2 Secondary Ion Mass Spectroscopy

Commonly used techniques for depth profiling of chemical phosphorus are *SIMS, AES* (Auger electron spectroscopy) and *RBS* (Rutherford backscattering). *SIMS* has the advantage of a higher depth resolution and good detection sensitivity due to which it has been in widespread use for the past four decades. In the case of dopant profiling *SIMS* has always been realised as a powerful tool, however, it requires accurate calibration.

The basic principle of *SIMS* is shown in Figure 12 [73]. It constitutes sputtering of a sample surface by an internally generated energetic primary ion beam. This results in the ejection of neutral and charged ions from close vicinity of the impacted surface. Most of the sputtered atoms/molecules are neutral, however, a small percentage are ionized (typical ionization probability is less than 5%) which are referred to as secondary ions. These secondary ions are

accelerated and analysed by a mass spectrometer. The rate with which the atomic layers of the specimen are removed is determined by (a) the chemical and physical characteristics of the specimen itself and (b) the mass, flux and energy of primary ions.

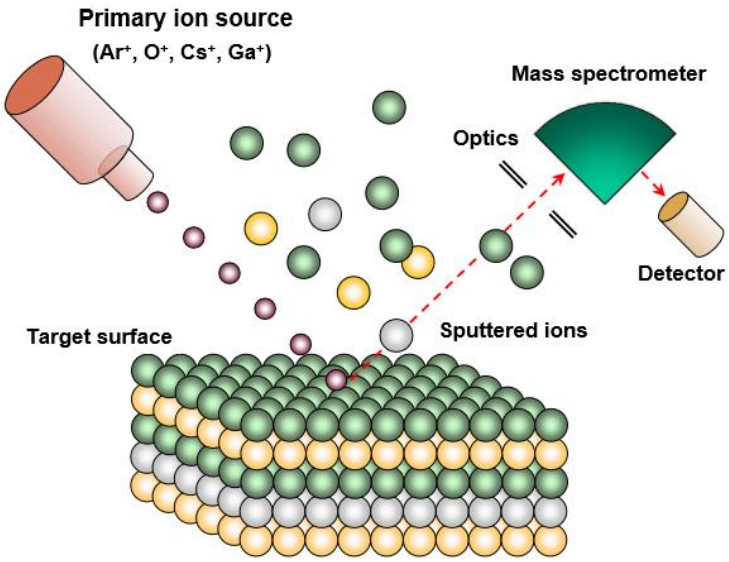


Figure 12: [73] Schematic of the *SIMS* technique. See text for explanation.

Depth resolution of *SIMS* is defined as the depth over which the concentration drops by 1 decade of concentration, measured using a well known sharp layer such as a delta layer. It is thus the ability of the instrument to discriminate between atoms in adjacent layers. Ion beam mixing, ion induced roughening and segregation effects adversely affect signal decays. The use of low energy primary beams, at an appropriate angle of incidence minimizes both the mixing and ion beam induced roughening effects.

Generally, the measurement of the concentration of dopants in semiconductors is undertaken by using either O (oxygen) or Cs (caesium) primary beams and recording the intensity of the various secondary ions, either as positively charged or negatively charged ions as a function of sputter erosion time. Positive Cs ions favour production of negative secondary ions while negative O ions favour generation of positive secondary ions. The secondary ion intensity, I_s, is given by [74],

$$I_s = I_p TC\alpha Y \tag{3.3}$$

where I_p is the primary ion current, T is the instrument's ion transmission efficiency from sample to the detector, C is the fractional concentration of the secondary particles (neutral and ionic) in the surface layer, α is the ionization probability and Y is the sputter yield which is given by the number of secondary particles sputtered by one primary particle. The product αT is called the useful yield, which is the number of secondary ions detected per secondary particle sputtered.

The intensity-time profile has to be converted into a concentration-depth profile. Usually the assumption of a constant sputter rate is used to establish the depth scale. The sputter rate is calculated after measuring the *SIMS* crater depth with the help of a stylus or an optical profilometer. On the other hand, the concentration of the element of interest, $c(E)$, is calculated [75] using the detected intensity of the element, $I(E)$,

$$c(E) = RSF(E,S)\frac{I(E)}{I(S)} \tag{3.4}$$

where $I(S)$ is the intensity of the sample matrix (substance within which the impurity E exists) and $RSF(E,S)$ denotes the relative sensitivity factors (and/or the calibration factors). $RSF(E,S)$ are determined using appropriate *SIMS* calibration reference materials. The calibration material must comprise a known concentration of the element of interest in the same matrix and should be analysed under the same conditions as the sample whose concentration has to be determined.

Prior to ejection from the surface, some of the ionized secondary particles can neutralize within the surface layers of the host matrix. The ionization probability of a certain species has therefore strong matrix dependence in that the ionization probability depends on the instantaneous local chemistry of the surface and can vary by several orders in magnitude [73, 76]. When the impurity content in a given matrix is very high (greater than ~ 1%) the local chemistry of the surface (and therefore the ionization probability) changes significantly with impurity concentration since the matrix concentration can no longer be regarded as a

constant [74]. A more pronounced change in the sputtered surface is present across interfaces [77]. The calibration factors are critically dependent on the matrix material and as a result, quantification of *SIMS* data becomes problematic (for the case of heterogeneous matrices and/or high impurity concentrations): a phenomenon commonly known as the *SIMS* matrix effect [73, 76, 77].

One of the strategies to minimise the *SIMS* matrix effects is the use MCs^+ method, which involves using a *Cs* primary beam and monitoring the intensity of MCs^+ clusters as positive ions, where M is the dopant to be measured. The MCs^+ method has been shown to minimise the *SIMS* matrix effects by a number of authors and significantly extends the concentration range in which the calibration is valid [78, 79]. The signal of MCs^+ clusters depends on the combination probability of Cs^+ ion and a neutral sputtered atom M^0 in the ejection process. The combination probability in turn depends on the affinity between the two species and the ionization probability of the complex MCs^+. Due to the low ionization potential of Cs, it has a high ionization probability. Hence the ionization probability of Cs, which under most conditions is independent of the matrix, dominates the ionization probability of the complex and since Cs is supplied uniformly throughout sputtering the ionization probability of the complex remains more or less uniform. Therefore, under steady state conditions the flux of MCs^+ complex directly represents the atomic concentration of M, C_M, and a linear relation [73, 76, 77] between the intensity of MCs^+ ions, I_{MCs^+}, and C_M is observed i.e.,

$$C_M = R_k I_{MCs^+} \tag{3.5}$$

where R_k is a constant.

Theoretically, MCs^+ *SIMS* is independent of the matrix effect and in one of the earliest studies of the technique Gnasner *et al.* [77] had reported that the intensity ratio of $SiCs^+$ in SiO_2 to that in *Si* is identical to the actual concentration ratio. Despite this early success, several researchers [80, 81] found that in materials with a low sputtering yield, such as silicon and oxides, the steady state Cs surface concentration under low bombardment energies can become very high, causing a decrease in the surface work function and thereby

lowering of the MCs^+ signal. Under such conditions then, the I_{MCs^+} signal becomes Cs (and therefore somewhat matrix) dependent and the accuracy of the linear relation between C_M and I_{MCs^+} is under question. For depth resolutions down to 1nm, primary ion energies in the range of 300-500 eV [82] are required and quantification using MCs^+ *SIMS* becomes problematic. Furthermore, intensity profiles of $SiCs^+$ and $AsCs^+$ in arsenic (As) doped *Si/SiO₂* structures have suggested that the MCs^+ signal also suffers from signal depletion at the *Si/SiO₂* interface [83].

When using MCs^+ *SIMS* the matrix effect for materials with low sputtering (and under low impact energies) can be circumvented by increasing [81, 82, 84] the angle of incidence to more than 60º off normal to the sample surface, thereby increasing the sputtering yield and resulting in a constant MCs^+/Cs^+ ratio. It should be noted that the trade off using MCs^+ *SIMS* compared to the conventional *SIMS* methods is higher detection limits by several orders of magnitude. The best detection limit for P (~$10^{16}cm^{-3}$) is achieved by using conventional *SIMS*, monitoring $^{31}P^-$ (negatively charged) under high mass resolution conditions using a high energy Cs primary ion beam. In comparison, MCs^+ *SIMS* suffers from a low useful yield resulting in high sensitivities. This is particularly true for electronegative elements like phosphorus. In such cases, detection of MCs_2^+ molecular ions has been found to offer better sensitivity compared to MCs^+ detection [83]. For example, Holliger *et al.* [83] have found that relative to MCs^+ the yield of n-type dopants with MCs_2^+ is increased by a factor of 10 in *Si* and by 10^2 in *SiO₂*. Using MCs_2^+ detection, the authors reported good depth resolution and minimal matrix effects in the range of impact energies 1–2 keV and incidence angles 44–56º. In addition, the authors did not find any MCs_2^+ signal depletion at the *Si/SiO₂* interface.

From the point of view of shallow emitters, dopant concentrations above $10^{20}cm^{-3}$ in *Si* are important. This is because in addition to all of the inactive dopant, most of the electrically active phosphorus of modern day shallow emitters is present above this concentration level [13]. Conventional *SIMS*, wherein quantification is only valid up to $5 \times 10^{20}cm^{-3}$, is not

suitable for profiling of shallow emitters where surface concentrations in excess of $10^{21} cm^{-3}$ are expected. On the other hand, PCs_2^+ detection with a detection limit of $2 \times 10^{19} cm^{-3}$ is ideal for profiling through the high concentration levels of state of the art shallow emitters. Moreover, PCs_2^+ detection offers the possibility of profiling in the *PSG/Si* system (i.e. in the *PSG*, across the *PSG/Si* interface and in *Si*).

Although it is beyond the scope of this thesis to model diffusion in the *PSG/Si* system, phosphorus profiles were still acquired in the *PSG/Si* system rather than in *Si* only. The primary reasons were two-fold. The first is that (a) the relationship between phosphorus concentration in the *PSG* and at the *Si* surface under different diffusion conditions is important and can facilitate future work on modelling diffusion in the *PSG/Si* system. In addition, (b) the *Si* surface concentration can easily be discerned from the P profile in the *PSG/Si* system (as will be discussed shortly) and as such acquiring the P profile in the *PSG/Si* system does not limit information regarding the P profile in *Si*.

In this work, PCs_2^+ detection has been used for profiling in the *PSG/Si* system. Characterization of all the experimental processes listed in appendix A was carried out using 1 keV Cs primary ions, incident at an angle of 40 degrees, and monitoring the appropriate PCs_2^+ clusters as a function of the erosion time. The experiments were conducted using a modified Cameca IMS 4F magnetic sector by Hamid Kheyrandish at Aystorm Scientific Ltd [85]. Calibration curves (intensity vs concentration plots), were obtained for P in *Si* and P in *PSG* using a series of reference samples that were measured using *ICP* (Inductively Coupled Plasma) analysis. The depth of the resulting *SIMS* craters has been measured using a Dektak surface profilometer, making appropriate corrections for the different erosion rates of the *PSG* compared to the *Si* substrate.

The *P* profile in the *PSG/Si* system is shown in Figure 13. According to several studies the peak in the phosphorus profile corresponds to the *PSG/Si* interface [86, 87, 88, 89] where dopant pile-up takes place. It has been found that *P* is trapped at the *oxide/Si* interface where the interface phase is characterized by a fixed total density of traps which are partly occupied

and partly unoccupied by dopants [87, 88, 90]. The dopant is trapped in 1-3 monolayer(s) [87, 89] and results in a peak in the *P* profile. This point of view is also supported from the SIMS data collected in this study; the location of the P peak also corresponds to the depth where the change in *Si* intensity (dI_{Si}/dx) is a maximum. The *Si* intensity decreases from substrate interface going into the *PSG*.

In Figure 13 much of the phosphorus profile in the *PSG* is essentially flat but then drops rapidly prior to the pile-up. The flat region corresponds to liquid phase *PSG* [86, 91, 92] while the rapid drop has been associated with a thin solid *PSG* layer sandwiched [86, 91] between the pile-up region and liquid *PSG*. The inset in Figure 13 depicts the complete profile in the *PSG/Si* system where the profile in *Si* is located to the right of the pile-up region.

In reality the pile up is sharp with a relatively lower peak concentration compared to the smeared out PCs_2^+ *SIMS* profile which is perhaps due to interface roughness and/or the relatively poor depth resolution (4 nm) of the PCs_2^+ method for this very sharp interface feature. Higher depth resolutions at lower primary ion incident energies compromise the sensitivity of the technique. In the interfacial region the profile of *P* is expected to be closer to what is measured by GI-XRF profiles (grazing incidence x-ray fluorescence spectroscopy) [87, 89]. The expected true profile of *P* in the interface region is shown by the dotted red line in Figure 13.

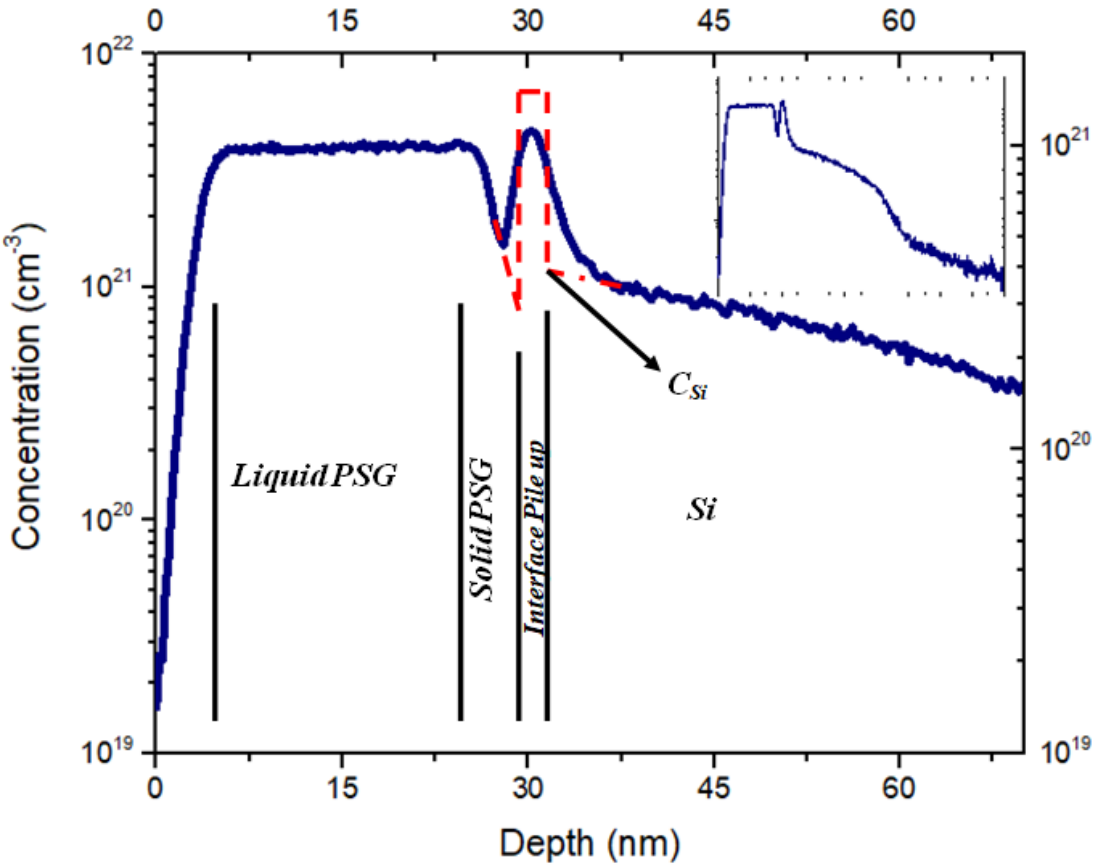


Figure 13: *SIMS* profile (blue) of *P* in the *PSG* & in the *PSG/Si* interface region for process 5 in Appendix A (890 ºC, 9.25 mins). Inset shows the complete profile in the *PSG/Si* system. Dotted red line in the pile up region depicts the expected profile in this region (see text for explanation).

The existence of the trapping layer allows one to determine the concentration of the dopant on the *Si* side of the *PSG/Si* system. The *Si* surface concentration, C_{Si}, is taken by extrapolating the concentration of the dopant at a point 4nm away from the pile up, as shown in Figure 13. Beyond the point of 4nm and away into the *Si* bulk, the *Si* intensity is a constant. Similarly, the *Si* intensity is a constant in liquid *PSG*, away from pile up region. The approximation that bulk *Si* concentration extrapolates continuously into the segregation layer is thought to be reasonable [87].

In one of the samples, the *PSG* was removed using HF and the *P* in the *Si* substrate was subsequently measured using conventional *SIMS*, monitoring $^{31}P^-$ (negatively charged) under high mass resolution conditions using a Cs primary beam. The *SIMS* calibration standard in this case was a NIST certified (*P* in *Si*) reference calibration sample. In Figure 14, the two profiles are shown where the sputtered depth of conventional *SIMS* profiles is offset by 5 nm.

Such an offset can be attributed to several factors including: (a) the HF dip that might not have removed interface layer(s), (b) the error in the determination of the *Si* surface discussed above, (c) the different depth resolutions (4 nm & 10 nm for conventional & PCs_2^+, respectively) and (d) the varying data densities of the two techniques that result in slightly different overall sputtered depths. The data density (number of data points per unit depth) decreases with increasing sputtering rates, which in turn increases with primary ion energy.

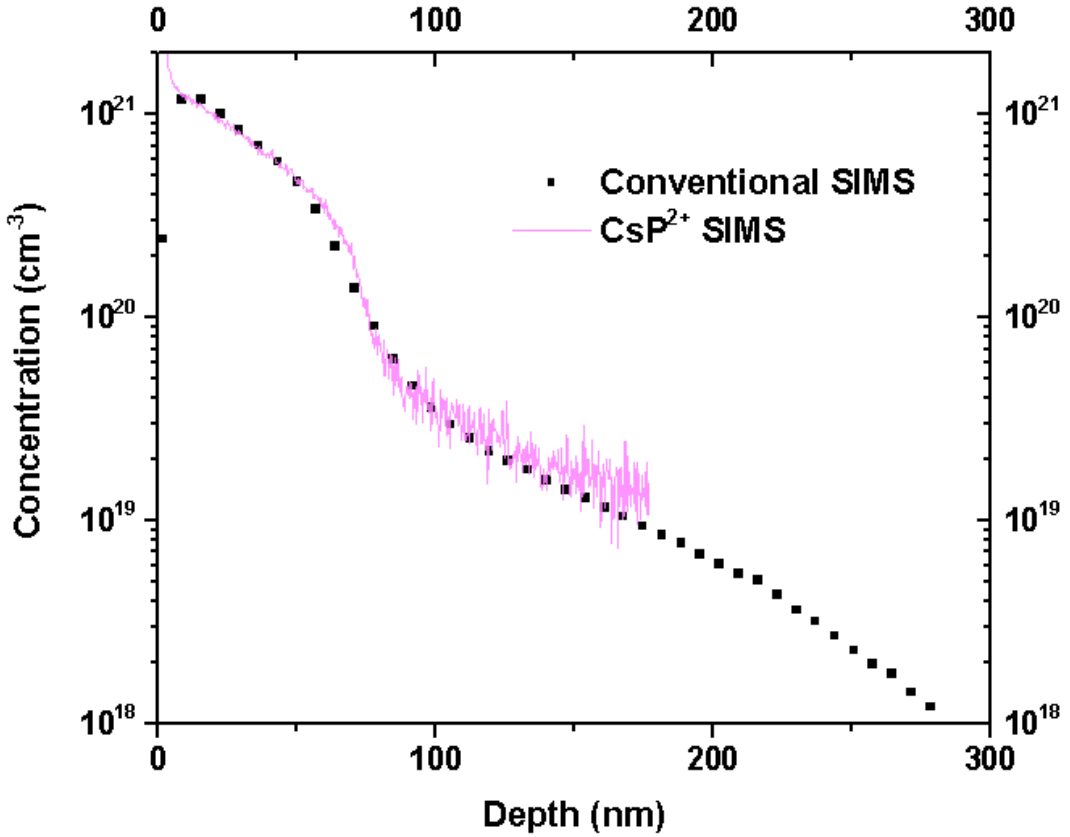


Figure 14: Conventional & PCs_2^+ *SIMS* profiles for process 6 in Appendix A (890 ºC, 14.25 mins).

Due to its poor depth resolution and low data density the conventional *SIMS* signal is not sharp in the concentration range $1 - 4 \times 10^{20} cm^{-3}$ where the signal begins to drop rapidly. At higher doping levels the conventional *SIMS* signal is in reasonable agreement with the PCs_2^+ signal but begins to deviate around the maximum concentration in the specimen (~$1 \times 10^{21} cm^{-3}$).

The PCs_2^+ signal is able to capture the sharp drop in dopant concentration due to improved depth resolution and high data density. It is also expected to be more accurate in the very high concentration range (greater than $10^{21}cm^{-3}$) since it is least affected by the *SIMS* matrix effect. However, as pointed out earlier, it is limited by the detection sensitivity $\sim 2 \times 10^{19}cm^{-3}$.

3.2 Diffusion Furnace

The diffusion furnace which has already been introduced in chapter 1, is shown here again in Figure 15.

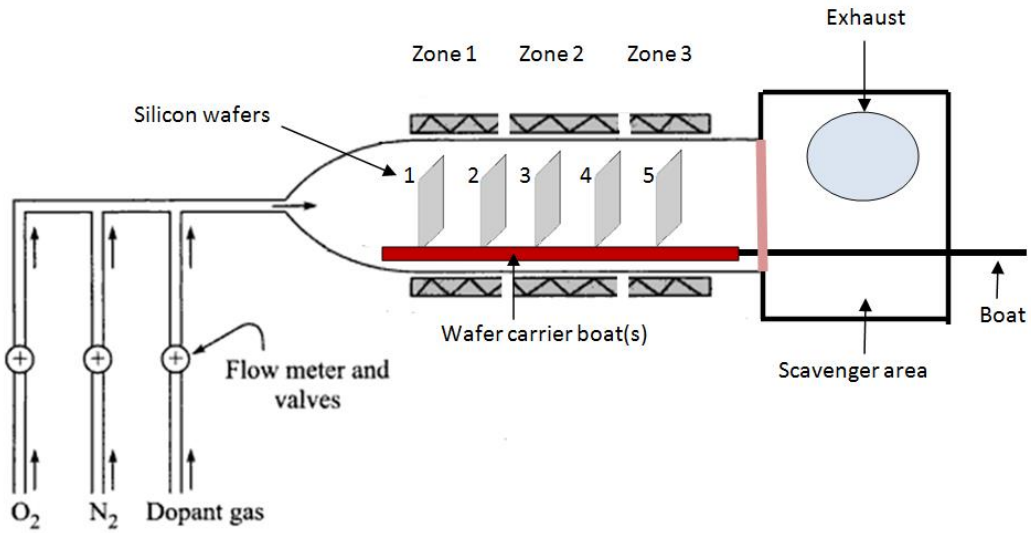


Figure 15: Schematic of the diffusion furnace used in this study. Furnace comprised of three heating zones. The tube was 1375 mm long and had an internal diameter of 205 mm. For each diffusion run, wafers were loaded on five different slots on a wafer boat with a spacing of 10 cm between wafers.

The gases (99.99999% pure $POCl_3$, 99.9% pure O_2 and 99.998% pure N_2) were supplied via different mass flow controllers (MFCs). The main N_2 flow is large, typically 6-14 SLPM (standard litres per minute), and provides the inert ambient. The amount of $POCl_3$ coming out of the bubbler depends on the N_2 flow through the bubbler and the temperature of the bubbler. The pick-up rate of $POCl_3$ (in g/min), M_{POCl_3}, is given by [93],

$$M_{POCl_3} = \left[\frac{P_{vap}}{P_B - P_{vap}}\right]\left[(Q_{C_2})\left(\frac{MW}{22414}\right)\right] \tag{3.6}$$

where P_{vap} is the vapour pressure at bubbler temperature, P_B is the pressure in bubbler, MW is the molecular weight of $POCl_3$ and Q_{C_2} is the carrier flow in SCCM (standard cubic centimetres per minute).

For a maximum bubbler flow of 2 SLPM (2000 SCCM) the $POCl_3$ pick up rate is 0.5 g/min [93] which (at bubbler temperatures) translates into an actual flow of ~ 70 SCCM of pure $POCl_3$. $POCl_3$ contents in the gas stream are typically in the range 0.03-1% while oxygen concentrations are in the 1.5-6% range, and almost 93-98% of the total gas volume is N_2.

The diffusion furnace used in this work comprised of three zones as shown in Figure 15. The temperature in each zone was controlled directly by adjusting the power supplied to the corresponding heating element. All diffusion runs included the test specimen and four baffle wafers placed on a wafer carrier that was mounted on a boat. The wafer configuration will be discussed in section 3.3. The boat was loaded manually and a furnace door that was attached to the boat enclosed the rear end of the tube. The door was air tight but had small openings to allow the gas to be extracted into the scavenger area with the help of a fan. Since the extracted gases contain chlorine, they are filtered prior to being expelled through the fan.

The gas mixture was supplied via a spigot at the front end of the tube. Information regarding gas valve on/off states, gas flow rates, temperature, diffusion times, etc. was directly entered into a recipe on computer controller that was configured for the furnace. The bubbler temperature was set manually and for all diffusion runs reported in this work the bubbler temperature was set to 20 ºC.

3.3 Sample Preparation

In most cases, as was pointed out in section 1.5, the gas distribution inside a diffusion furnace is not homogeneous. Theoretically speaking, gases will acquire a homogeneous distribution within the tube after several minutes (expected to be ~ 7-15 minutes in practical systems under conventional processing conditions). This time is the residence time of the system, which is often approximately determined as the ratio of the tube volume to the flow

rate of the gas mixture. However, in real systems the residence time will also depend on the geometry of the wafer load, temperature and the rate of extraction of gases via the exhaust. For very long annealing times (an order of magnitude greater than the residence time of the system), the effects of gas non-homogeneity during the initial diffusion period on the diffusion profile in Si are negligible. However, for the short diffusion processes proposed in section 1.5 as a means to reducing inactive P, gas non-homogeneity with respect to diffusion duration cannot be ignored.

For very short diffusion durations where gas homogenization has not been completed, the diffusion process can be studied at a location closer to the gas inlet. Therefore, the post diffusion characterizations (*SIMS*) in this study were carried out on a silicon wafer, which was placed closer to the gas inlet. Each diffusion run comprised of five wafers, which included the actual specimen that later underwent *SIMS* characterization and additional four wafers which were used as baffle wafers. The wafer configuration is shown in Figure 15, where the specimen was placed in slot 2 while baffle wafers were placed in slots 1, 3, 4 and 5, with ~ 10-cm spacing between wafers. The wafer configuration shown in Figure 15 was found to be particularly useful in allowing the diffusion process to be uniform across the wafer in slot 2 for a certain diffusion process and a range of diffusion durations (1-14 mins). This is shown in Figure 16 where it can be seen that reasonable uniformity (error bars in Figure 16) for the specimen in slot 2 is achieved for all processes, including the very short diffusion durations. The diffusion processes in Figure 16 used the same gas mixture composition ($POCl_3$ flow rate 375 SCCM, O_2 flow rate 500 SCCM and N_2 flow rate 13.125 SLPM) and temperature (890 ^oC). The specimens were cooled rapidly at the end of the process.

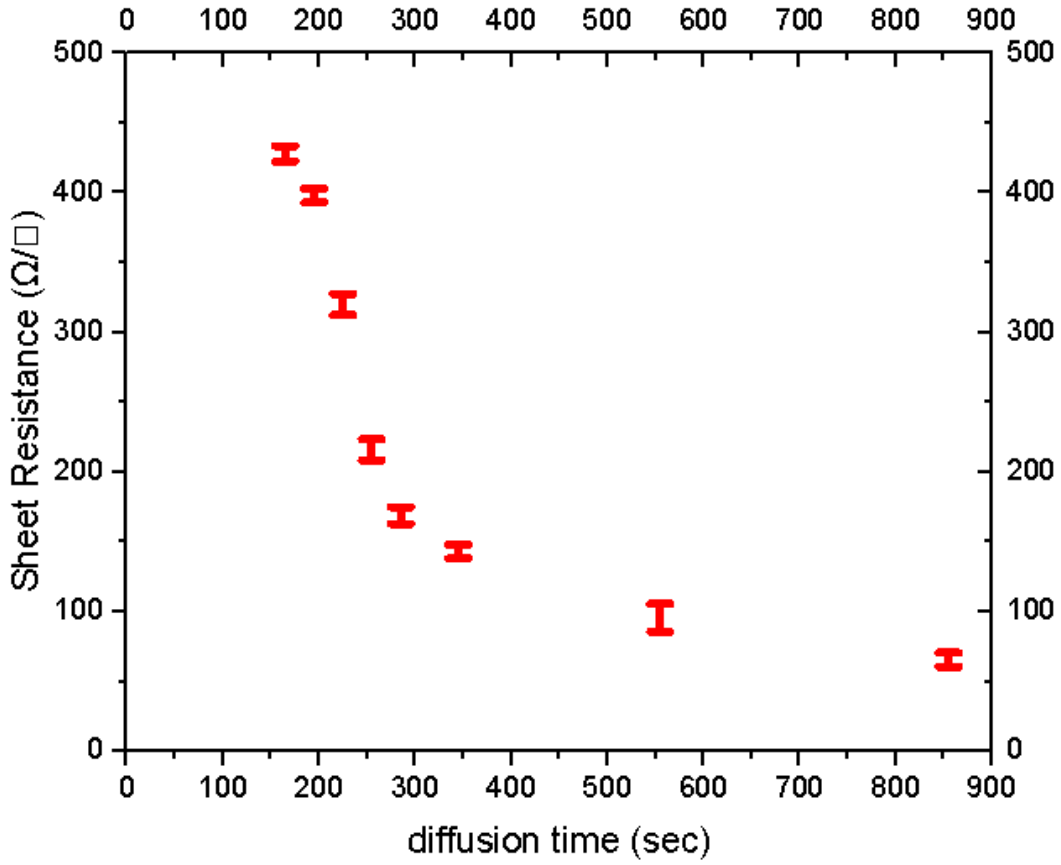


Figure 16: Sheet resistance versus diffusion time for the specimen in slot 2 (as illustrated in Figure 15) for diffusion processes conducted at 890 ºC. Error bar depict the maximum variation across the wafer. Clearly, shallow emitters with sheet resistances between 80-140 Ω/□ can be formed within 6-9 minutes at 890 ºC.

The temperature, $POCl_3$ flow and O_2 flow ranges considered in this study are 865-968 ºC, 200-1750 SCCM and 300-700 SCCM, respectively. A total of 15 processing runs were carried out where the baffle wafers were replaced after each diffusion run and a 1×1 mm sample was cut from the middle of the test wafer (in location 2) and subjected to depth profiling via PCs_2^+ *SIMS*. P-type float zone (FZ) polished 6" *Si* wafers with resistivity of around 10kΩcm were used for the specimens in slot 2. Details of the processing conditions for different diffusion runs can be found in Appendix A. While the wide range of gas flow compositions listed in Appendix A includes high $POCl_3$ contents that are typical of industrial processing, the temperatures and durations used in this study are markedly different than what are used in conventional processing. Typical industrial diffusion durations and temperatures are in the range 10 to 20 minutes and 840-880 ºC, respectively.

For each diffusion run listed in Appendix A and those shown in Figure 16, the furnace was loaded with wafers in the five slots depicted in Figure 15 and allowed to stabilize at the desired diffusion temperature, prior to opening the gas ($POCl_3$, O_2 and N_2) valves. At the end of the process, the supply of $POCl_3$ and O_2 gases was cut-off, allowing only N_2 gas to flow and resulting in a drive-in process. The drive-in cycle for each process lasted for only 15 seconds and was carried out to ensure that the toxic by product (chlorine) exits the tube prior to wafer extraction, which was done rapidly (less than five seconds) using an automated boat-loader. The delay of gases in reaching the wafers and the delays associated with gas valve on/off states and in pulling the wafers out of the furnace have been approximated and accounted for in the diffusion durations listed in Appendix A. Despite the fact that each run comprised of a drive-in process (where $POCl_3$ and O_2 gasses are off) of ~15 seconds, the diffusion runs in this work are treated as deposition runs only. In determining the P concentration at the Si surface (section 4.2), it has been assumed that the surface concentration is unaffected by the very small drive-in durations and that one can regard the entire process comprising of only the deposition cycle. This assumption might be erroneous for the very short (less than three minutes) diffusion durations where the drive-in durations (15 seconds) are not negligible in comparison to the deposition durations.

CHAPTER 4
A SIMULATION STUDY OF PHOSPHORUS DIFFUSION IN SILICON

Accurate modelling of high concentration phosphorus diffusion in silicon has, to date, not been possible due to several reasons. One of these is that the process cannot be modelled with the simplified diffusion equation that uses the relative concentration of point defects (relative to the intrinsic concentration of these defects as was discussed in chapter 2), as these equations are only valid for the case of point defect equilibrium which is not present throughout the phosphorus profile. Where actual point defect concentrations are used as fitting parameters to allow for the incorporation of non-equilibrium effects, two issues are often encountered in modelling of P diffusion in *Si*. The first is the very large number of fitting parameters and the lack of experimental data to validate these models over a wide range of conditions. In addition, the substantial variations reported in the literature for the actual point defect concentrations will result in the diffusion model using a large number of unknown parameters. The second, and perhaps the most important issue faced in the modelling of P diffusion, is that determination of the chemical reaction(s) that govern(s) the changeover from point defect equilibrium to non-equilibrium, as the electron concentration decreases, has remained a problem. It was pointed out in chapter 2 that P diffuses predominantly via a (an) vacancy (interstitial) diffusion mechanism at high (low) electron concentrations where the point defect concentrations are in equilibrium (non-equilibrium). Therefore, it is important to consider the chemical reactions (mechanisms) responsible for point defect non-equilibrium at low doping levels and those responsible for restoring

equilibrium at high doping levels. These reactions must be consistent with experimental and theoretical studies conducted on the subject over the last six decades. In addition, the subsequent mass action relationships (of these reactions) should allow accurate modelling of the P concentration profile.

Other reasons that complicate modelling of high concentration P diffusion include dopant precipitation and difficulties with the determination of the surface concentration. Inclusion of phosphorus precipitation to dopant diffusion modelling is important since phosphorus precipitates can act as a sink or source to the electrically active (mobile) phosphorus, thereby modifying the overall diffusion profile in *Si*. However, incorporation of dopant precipitation increases the number of fitting parameters of the model. The choice of dopant diffusion and precipitation related parameters should be such that they should (a) have an Arrhenius dependence in most cases, (b) allow for the accurate determination of total P and (c) result in reasonable agreement with the electrically active P profiles that have been previously reported using $POCl_3$ sources.

Diffusion studies conducted on ion-implanted specimens are often complicated by the presence of implantation damage that perturbs the point defect equilibrium. Note that the damage-induced perturbation is different from the perturbation induced by phosphorus diffusion itself, which was discussed above and in chapter 2. Implanted specimens, however, have the advantage that the exact amount of dopant in the material prior to annealing is known. On the other hand, in-diffusion from a surface source does not induce a (significant) point defect perturbation but the flux of dopant entering *Si* is then under question. The simplest, and the most common [15, 46, 47, 61], approach is to assume that the dopant source is infinitely rich with dopant and that the surface concentration remains constant throughout diffusion. Such approximations, however, might only be somewhat useful when diffusion studies are conducted for elongated times wherein the surface concentration attains an almost stable value after a certain initial duration.

The mathematical model developed in this chapter uses the relative (to intrinsic) concentration of point defects, thereby significantly reducing the fitting parameters. It is shown that inclusion of the appropriate changeover phenomenon responsible for restoring point defect equilibrium allows accurate modelling of the process without resorting to the actual point defect concentrations. The dopant precipitation and clustering model [64], as discussed in chapter 2, has been used with careful reconsideration of the solubility limit of P. As a result, the electrically active P profiles are in reasonable agreement with those previously reported. In addition, an empirical relationship for the phosphorus concentration at the silicon surface has been used and very good modelling accuracy, compared to all previous studies [15, 46, 47, 60, 61], has been demonstrated.

In this chapter, the simulation methodology and the silicon surface concentration is first discussed. The effective diffusivity of phosphorus in *Si* is explained in section 4.3 while extraction of diffusion, precipitation and surface concentration related constants is discussed in section 4.4.

4.1 Simulation Methodology

In this work simulations have been carried out using *Visual C#*. The simulations are based on the finite difference method (FDM) where depth into the wafer is discretized into cells of width dx. Two and three dimensional arrays are used for dopant $C(i,t)$ and precipitate $f(i,t,u)$ concentrations (where u refers to the size of the precipitate.), respectively. In Figure 17 the flux of C_P^+ $(f(i,t,1))$ at time t is shown for cell i.

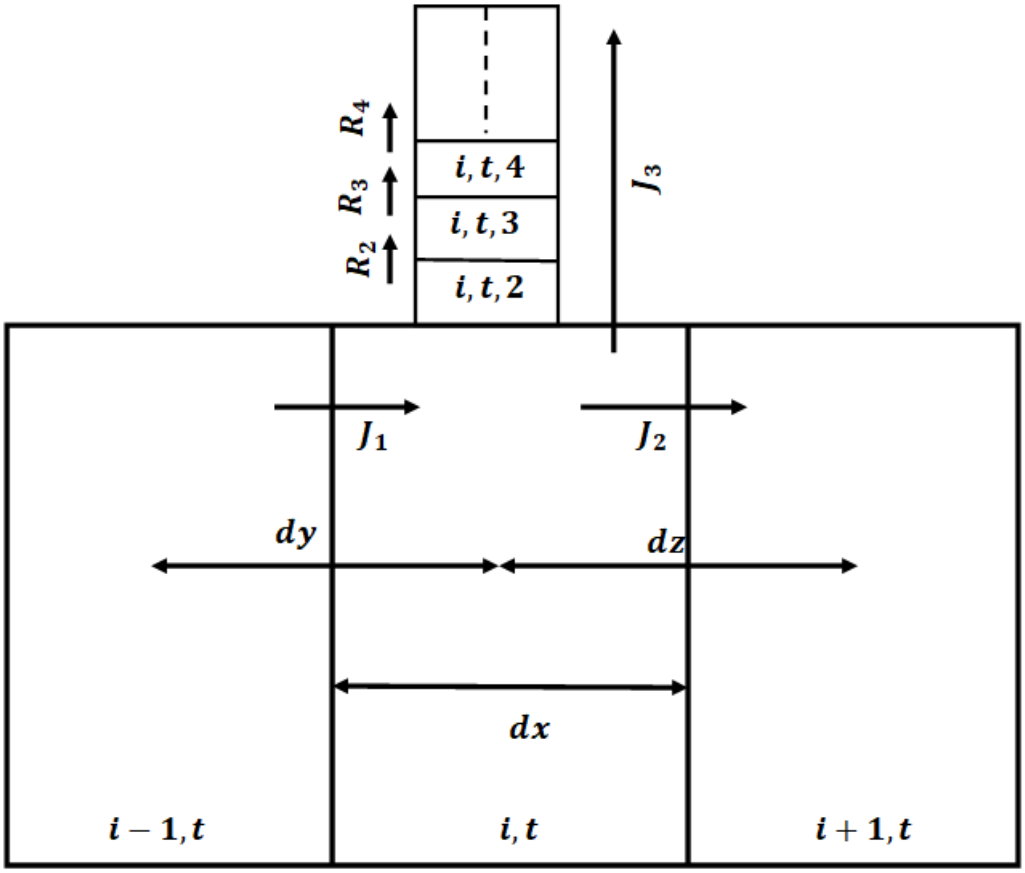


Figure 17: Schematic of FDM where flux of the solute C_P^+ flowing across cell i is shown. R_u is the flux of solute involved in the net growth from precipitate of size u to $u+1$ due to the addition (removal) of solute atoms to (from) the u $(u+1)$ sized precipitate. J_3 represents the sum of the individual solute fluxes (sum of individual R_u) that are involved in the growth of precipitates of all sizes. Therefore, J_3 represents the total solute flux due to precipitation/dissolution.

J_1 is the flux of dopant entering cell i from left $i-1$ and J_2 is the flux from cell i to $i+1$.

$$J_1 = -hD\left(\frac{f(i,t-1,1)-f(i-1,t-1,1)}{dy}\right) \tag{4.1a}$$

$$J_2 = -hD\left(\frac{f(i+1,t-1,1)-f(i,t-1,1)}{dz}\right) \tag{4.1b}$$

where dx is the width of cell i, dy is the distance from the midpoint of cell i to that of cell $i+1$ and dz is the distance from the midpoint of cell $i-1$ to that of cell i. The cell width dx is kept 1 nm up to a certain depth (145 nm), i.e. $dx = dy = dz$ for the first 145 cells. Beyond that dx is increased to larger widths to improve the simulation speed.

The net growth rate of precipitates (R_u) of size u into size $u+1$ is given by equation 2.26. It has been reproduced below, and as discussed in section 2.5.2.2, equation 2.26 takes into account both the growth and dissolution terms.

$$R_u = g_u f_u - d_{u+1} f_{u+1} \tag{2.26}$$

where the growth, g_u, and dissolution, d_u, rates can be determined using equations 2.28 and 2.30, respectively and f_u refers to $f(i,t,u)$.

The accumulative solute flux, J_3, which is used in the growth of precipitates [64] of all sizes was discussed in section 2.5.2.2. (equation 2.27) and has been reproduced below,

$$J_3 = 2R_1 + \sum_{u=2}^{\infty} R_u \tag{2.27}$$

where R_1 represents the net growth rate (including dissolution) from size 1 to 2. The solute C_P^+ (cm^{-3}) at t then becomes,

$$f(x,t,1) = f(i,t-1,1) + \left({}^{J_1}/_{dx}\right) - \left({}^{J_2}/_{dx}\right) - J_3 \tag{4.2}$$

The total P concentration is given by the sum of the solute C_P^+ (cm^{-3}) concentration and the concentration of P atoms in all precipitates at time t,

$$C(i,t) = \sum_{u=2}^{\infty} u f(i,t,u) + f(i,t,1) \tag{4.3}$$

where $f(i,t,u)$ can be computed using the method described in section 2.5.2.2.

The solute concentration in the first cell is determined using the empirically determined surface concentration, C_{Si}, which is discussed in section 4.2.

$$f(0,t,1) = C_{Si} - \sum_{u=2}^{\infty} u f(0,t,u) - \left({}^{J_2}/_{dx}\right) \tag{4.4}$$

where the second term on the right hand side is the total precipitated *P* in the first cell.

The overall fitting parameters are the effective diffusivity, solubility limit and constants (a_1, a_2, a_3) for the determination of precipitate excess energy. These parameters are given in Tables 1 and 2 (section 4.4) and will be discussed further in sections 4.3 and 5.2.

While the treatment explained in section 2.5.2.2 for the determination of $f(i,t,u)$ is quite comprehensive, the full system described by the equations can become very large for large precipitate sizes, thereby reducing the simulation efficiency. In order to overcome this problem, the system is considered continuous [64] over all sizes and the size distribution is rediscretized such that each point in the size distribution represents a range of sizes ($u[z]$) rather than a single size (u). Accordingly, the growth rate of precipitates from size distribution $u[z]$ to size distribution $u[z+1]$ is given by [64],

$$R_{u[z]} = \frac{1}{2}\left[\frac{\left(\left(g_{u[z]} + d_{u[z]}\right)f_{u[z]} + \left(g_{u[z+1]} + d_{u[z+1]}\right)f_{u[z+1]}\right)}{u[z+1] - u[z]} + \left(\left(g_{u[z]} - d_{u[z]}\right)f_{n[z]} + \left(g_{u[z+1]} - d_{u[z+1]}\right)f_{u[z+1]}\right)\right] \quad (4.5)$$

where $f_{u[z]}$ represents precipitate concentrations between sizes $((u[z-1] + u[z])/2)$ and $((u[z] + u[z+1])/2)$, $g_{u[z]}$ represents the growth rate of precipitates at size distribution $u[z]$ and $d_{u[z]}$ represents the dissolution rate of precipitates at size distribution $u[z]$. The above equation reduces to equation 2.26 for $z = 1$. The value of z is kept 1 for up to precipitates of size 30 and is increased for larger sizes.

The highest precipitate size is kept greater than the largest precipitates that would form. In the work, the highest precipitate size is taken as that precipitate size whose concentration is less than $10^{-15}\ cm^{-3}$ at a given instant. The highest allowable precipitate size is incremented with diffusion time based on careful observations of the precipitate size

evolution at the surface where the solute concentration is highest. Since precipitation is diffusion limited (from Ham [70]), the largest precipitate size that would form at a particular instant in time depends on temperature, time and the solute concentration. In some cases, a highest precipitate size of 30 atoms was sufficient while in the case of heavily diffused wafers the highest precipitate size was more than 30,000 atoms. Due to the very small diffusion durations (often less than 10 minutes), very large precipitates do not form in most cases.

At higher temperatures and high solute concentrations, the diffusion coefficient can be very large. In addition, the very small width of cells (1 nm), required for good simulation resolution, result in very large flux terms. This is particularly true during the start of the process when the concentration in a neighbouring cell (or in a neighbouring precipitate size of the same cell) is zero, which generates a large gradient in concentration and hence a very large flux term. Such large flux terms can cause the concentrations to become negative and therefore the diffusivities (which in this study are concentration dependent) undefined. In order to avoid such instabilities, the time step needs to be reduced from 1 second. Therefore, each second in the simulation is divided into further time steps. For lightly doped substrates and/or low temperature processes, the duration of a time step can vary between 1 to 3 ms. For heavily doped substrates and/or high temperature processes the time step often varies in the range 0.05-0.3 ms. Moreover, the time step is not a constant throughout a particular simulation. Depending upon the flux terms, the duration of the time step can be increased (decreased) after several seconds/minutes in order to increase (avoid) simulation speed (instabilities). Similarly, the largest allowable precipitate size is dynamically changed to allow for faster simulation speeds.

During $POCl_3$ diffusion thermal oxidation results in the *PSG/Si* interface moving into *Si* and effectively *Si* is consumed in the process. The thickness of *Si* consumed is 0.46 times the total *PSG* thickness, which is the ratio of the volumes of the two materials. As the *PSG/Si*

interface moves into the substrate, the silicon layer adjacent to the interface (and the P content in it) will become part of the *PSG*; a phenomenon often referred to as the snowploughing effect. The snowploughing effect can perhaps be better understood in the discrete space-time domain, which is also important in the current context. If at time t the *PSG/Si* interface (trapping layer as discussed in section 3.2) moves by a unit cell, the silicon layer adjacent to the interface (and the P content in it) will become part of the *PSG/Si* interface. Moreover, the very large P concentration that was present at the *PSG/Si* interface at time $t-1$ will now become part of the newly formed *PSG* layer and will result in rapid trapping of P at the new interface. Consequently, we expect a push out effect to subsequently follow the snowplough effect, wherein the dopant is pushed back from the *PSG* to the Si via the trapping layer.

Studies pertaining to dopant trapping concentrations at the interface often ignore transient effects [87] like the snow-ploughing and push out effects owing to the rapid equilibrium that is established across the interface. However, if the amount of Si consumed is not negligible compared to the diffusion depth (which is especially true at the beginning of the $POCl_3$ process), then the Si consumption should not be ignored in any P in-diffusion simulation study. Therefore, in the context of this work only the Si consumption is taken into account, by considering that a pointer gives the location of the first (surface) cell in the array, and as oxidation proceeds, the value of the pointer is incremented. The value of the pointer at a particular time is given by,

$$Pointer = Floor\left\{\frac{PSGthickness \times 0.46}{dx}\right\} \tag{4.6}$$

where dx is the cell width taken to be 1nm and the function $Floor\{\}$ rounds the value to the smallest integer.

The simulations of P diffusion in *Si*, presented here are the first comprehensive simulations of the problem undertaken in the sense that these simulations co-model P precipitation

kinetics and P diffusion in the bulk. As was noted earlier, the inclusion of dopant precipitation increases the number of constants used in the model. Therefore, several considerations (which are discussed in more detail in section 4.4) were taken into account in determining the overall fitting parameters.

4.2 Phosphorus Concentration at the Si surface

Modelling diffusion in the *PSG/Si* structure allows the determination of the dopant concentration at the *Si* surface. However, this approach is quite complex since mass transport across several interfaces (gas/liquid-*PSG*, liquid-*PSG*/solid-*PSG*, solid-*PSG*/trapping-layer and trapping-layer/*Si*) needs to be taken into account. The P concentration at the Si surface, C_{Si}, is the concentration of the dopant on the Si side of the trapping (pile-up) layer. As was discussed in section 3.2, the P concentration at the Si surface, C_{Si}, is noted from the P profile by extrapolating the bulk concentration to the *PSG/Si* interface where the dopant pile up is present. In this work, C_{Si} is determined empirically using the relationships which are discussed in this section and are given in Appendix B.

In Figure 18, data for the phosphorus concentration at the silicon surface, C_{Si}, are shown for processes where only the diffusion duration was changed while all other parameters were kept constant. Also shown are the corresponding *PSG* thicknesses for the same processes. These processes are numbered 1 to 6 in Appendix A. The phosphorus concentration at the silicon surface remains low during the initial stages when the oxide growth rate is rapid. The rate with which C_{Si} increases rises rapidly after this initial diffusion time before stabilizing at a constant value for larger durations. As per this study C_{Si} does not achieve a constant value throughout the process, which is the assumption in most diffusion models [15, 46, 47, 61].

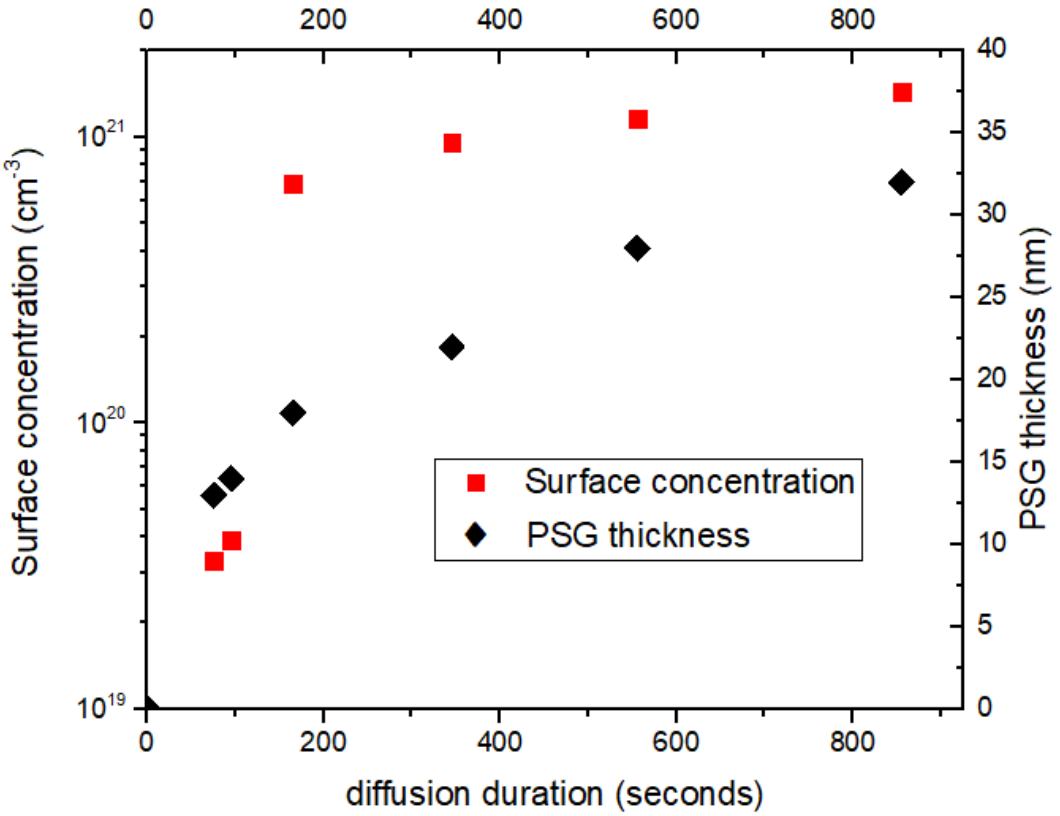


Figure 18: Phosphorus concentration at the silicon surface, C_{Si}, and *PSG* thickness vs diffusion time for processes with the same temperature and gas flow composition. Processes 1-6 in appendix A. The *PSG* thicknesses were obtained by recording the depth of the P *SIMS* signal from the *PSG* surface to the *PSG/Si* interface (pile up) while C_{Si} was (as explained in section 3.2) recorded by extrapolating the concentration in the Si bulk to the pile up region.

Due to the movement of the *PSG/Si* interface, a motion-induced flux, J_B, is present across the *PSG/Si* interface [94],

$$J_B = -v_{ox}(C_{PSG} - \alpha C_{Si}) \tag{4.7}$$

where v_{ox} is the oxidation rate and α is the ratio of the volumes of the two materials ($\alpha = 0.46$). J_B is directed from the *PSG* to Si and refers to the snow ploughing effect that was discussed in section 4.1. Equation 4.7 suggests that a large motion-induced flux will flow from the *Si* into the *PSG* when v_{ox} is large and when $C_{PSG} >> \alpha C_{Si}$. If the motion-induce flux is large it can significantly reduce the net flow of the dopant from *PSG* into Si. This in turn can explain the slow rise in C_{Si} during the initial stages of diffusion (since at the beginning of the process $C_{PSG} >> \alpha C_{Si}$ and v_{ox} is maximum).

In this work, the determination of the oxide thickness is made using equations similar to the Deal & Grove oxidation model [95]. For durations longer than 1 minute, the oxide thicknesses scale according to the Deal and Grove model as is shown by the blue line in Figure 19 for processes 1-6, where only the diffusion duration was changed while all other parameters were kept constant. For shorter durations, a rapid increase in the oxide thickness is accounted for by using a quadratic relationship (similar to the Deal and Grove equation), as shown by the orange line in Figure 19. The empirically determined *PSG* thickness (black dashed line in Figure 19) is given by the lower of the two *PSG* thickness values, equation 4.8a, which can be seen to agree reasonably well with the experimental thicknesses (red markers).

$$X\ (nm) = Min\big(h(t), k(t)\big) \tag{4.8a}$$

where $h(t)$ gives the oxide thickness for larger durations using the Deal and Grove equation and $k(t)$ accounts for the initial rapid growth,

$$h(t) = \frac{A}{2}\left(\sqrt{1 + \frac{4B_k}{A^2}(t+\tau)} - 1\right) \tag{4.8b}$$

$$k(t) = \frac{A}{2}\left(\sqrt{1 + \frac{4E_k t}{A^2}} - 1\right) \tag{4.8c}$$

$$\tau = \frac{x_i^2 + Ax_i}{B_k} \tag{4.8d}$$

where the constant B and E_k are the parabolic rate constants, B/A and E_k/A are the linear rate constants, t is the diffusion time in seconds, x_i is the initial oxide thickness and τ is a time constant associated with the initial oxide thickness. Values of the constants A and x_i are 1 nm and 12 nm, respectively, for all diffusion processes.

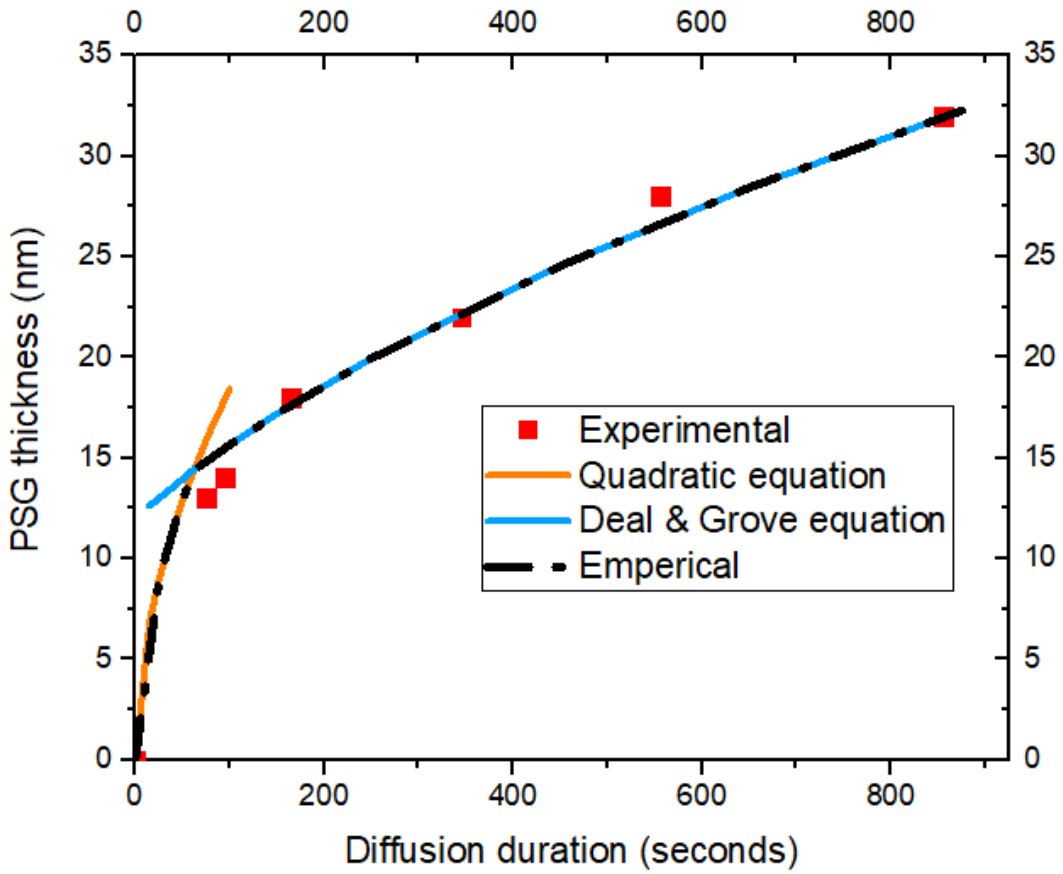


Figure 19: Oxide thickness vs diffusion time for processes with the same temperature and gas flow composition. Processes 1-6 in appendix A.

Incorrect estimates of the true instantaneous phosphorus surface concentration in Si can cause large variations in the simulated diffusion profiles. On the other hand, small discrepancies in the instantaneous oxide thickness will have a negligible effect on the overall P diffusion profile. This becomes more apparent when oxidation is completely ignored and only slight differences in diffusion depths are observed. From a simulation point of view, this means that the available oxide thickness data is sufficient to account for the effect of the *PSG/Si* interface movement and equation 4.8a need only reasonably predict the final *PSG* thicknesses, even if it does not accurately predict the instantaneous *PSG* thicknesses.

The oxidation model used in this work requires only two constants (B_k, E_k) and is able to reasonably determine the final oxide thicknesses for all processes listed in Appendix A. Equations for the determination of B_k and E_k for the different processing conditions are given in Appendix B. As will be discussed in section 4.4, the constants for the determination

of C_{Si} had to be selected based on the results of the simulations and are effectively fitting parameters in the diffusion model. On the other hand, the constants used in the oxidation model (B_k, E_k) are not used as fitting parameters in the diffusion model but are pre-determined using the equations listed in Appendix B such that the final oxide thicknesses are in good agreement with those determined experimentally.

The surface concentration data in Figure 18 are shown again in Figure 20 (red markers) along with the empirically determined surface concentration (dashed black line) that has been determined using equation 4.9a.

$$C_{Si}(cm^{-3}) = \begin{cases} (4.5 \times 10^{19})t, & t \leq t_0 \\ Min\big(f(t), g(t)\big), & Otherwise \end{cases} \quad (4.9a)$$

where t is the diffusion duration in seconds, t_0 is a time constant and the Operator $Min()$ returns the smaller value of the two values.

The functions $f(t)$ and $g(t)$ are given by,

$$f(t) = 10^{19} D_k \sqrt{(t - t_0)} \quad (4.9b)$$

$$g(t) = \frac{A_k}{0.1 + exp(-C_k t)} \quad (4.9c)$$

Equation 4.9a was found to provide the best fit to experimental data in the three regions (A, B and C) that are labelled in Figure 20. Region A represent the initial stages of diffusion where the supposed motion induced phenomena limits a significant increase in the surface concentration. In this region, the surface concentration is assumed to increase linearly with time (as is shown by the blue line). This linear increase takes place only for a certain initial duration, t_0, beyond which the *Si* surface concentration increases with the square root (the function $f(t)$) of diffusion time (region B, green line). For larger diffusion durations, region C, the increase in the *Si* surface concentration, region C, is explained by an S-curve ($g(t)$, orange line). For diffusion durations longer than t_0, the lower of the two values (determined using the root equation $f(t)$ and the S-curve $g(t)$) gives the surface concentration.

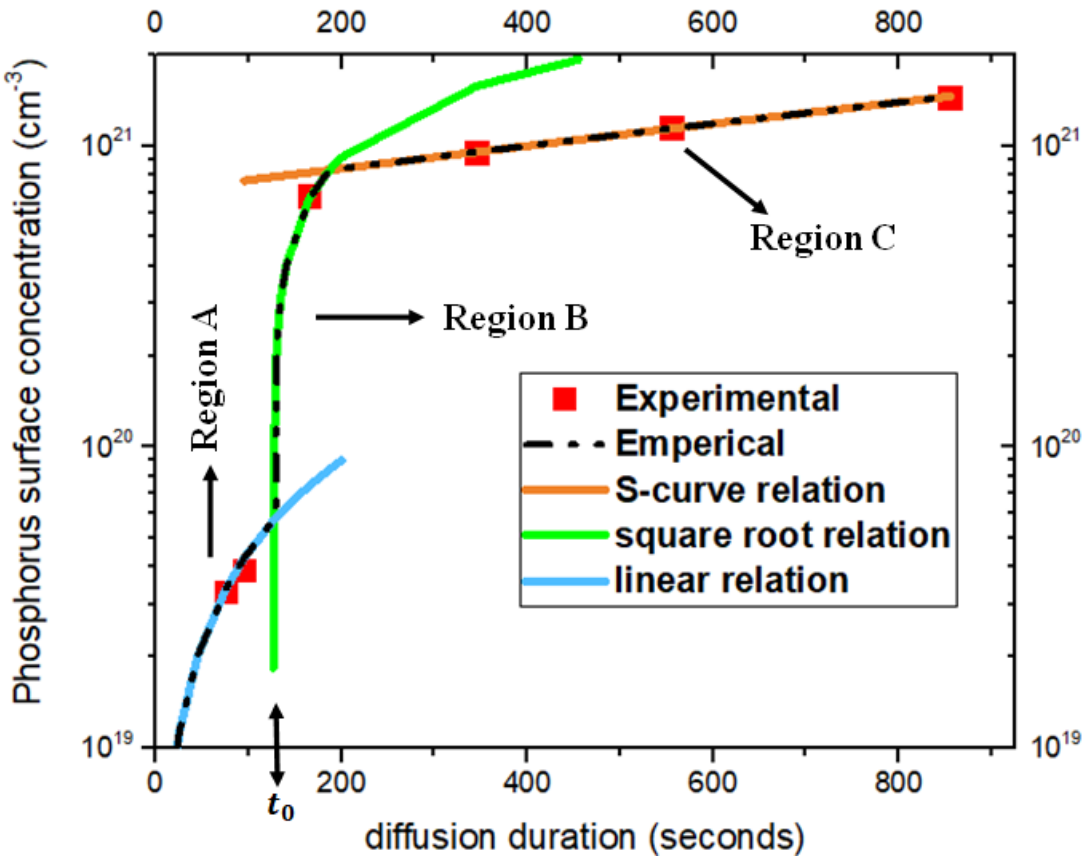


Figure 20: Phosphorus concentration at the silicon surface vs diffusion time for processes with the same temperature and gas flow composition. Processes 1-6 in appendix A.

The evolution of the P profile (processes 1-6 in appendix A) has been studied at a particular gas flow composition ($POCl_3$ = 375 SCCM, O_2 = 500 SCCM, N_2 = 13.125 SLPM) and temperature (890 ºC). For other gas flow compositions and temperatures (processes 7-15 in appendix A), data for the time evolution of the P profile was not available. The assumption of a constant surface concentration for processes 7-15 is not appropriate since it is clear from Figure 18 and Figure 20 that the surface concentration does not attain a constant value at any (obtained) point in time during $POCl_3$ diffusion. Therefore, based on available data and the motion-induced phenomena, it has been assumed in this work that the phosphorus concentration at the silicon surface for processes 7-15 scales in a manner similar to the one reported in Figure 20. That is to say that C_{Si} for processes 7-15 scales according to equation 4.9a. Moreover, the four constants (A_k, C_k, D_k and t_0) that are used in equations 4.9b and 4.9c (and given in Appendix B) are chosen such that very good agreement between empirically and experimentally determined C_{Si} is obtained.

It is obvious that several values of the constants can allow for good agreement between the final empirical surface concentration and that obtained experimentally. Therefore, the determination of the instantaneous P surface concentration (and thus the surface concentration associated constants) was only possible by carrying out P diffusion simulations using various values for the four constants in the three equations that determine the surface concentration. If the resulting simulation was sufficiently accurate, it was inferred that the instantaneous surface concentration used in the simulations was close to the actual instantaneous surface concentration for most of the simulated time. In section 4.4, I discuss the various considerations required in selecting the fitting parameters for the surface concentration, P effective diffusivity (which is discussed next in section 4.3) and P precipitation kinetics (that was discussed in section 2.5.2).

4.3 Effective Diffusivity of Phosphorus

The profile of electrically active phosphorus in the three regions is shown again in Figure 21. In chapter 2, a detailed explanation was given as to why P diffusion is thought to be mediated by vacancies in the high concentration region (region 1) and by interstitials in the low concentration region (region 3). In addition, the point defect concentrations are thought to be in equilibrium in region 1 while in region 3 there exists a supersaturation of interstitials that extends deep into the wafer. This changeover from a supersaturated interstitial concentration to point defect equilibrium is required to account for the rapid change in diffusivity at the kink. In most cases, diffusion models consider the injection of excess interstitials at the surface, which is inconsistent with experimental findings. Moreover, complex mathematical approaches are used that require a large set of fitting parameters which are not defined over a wide temperature range.

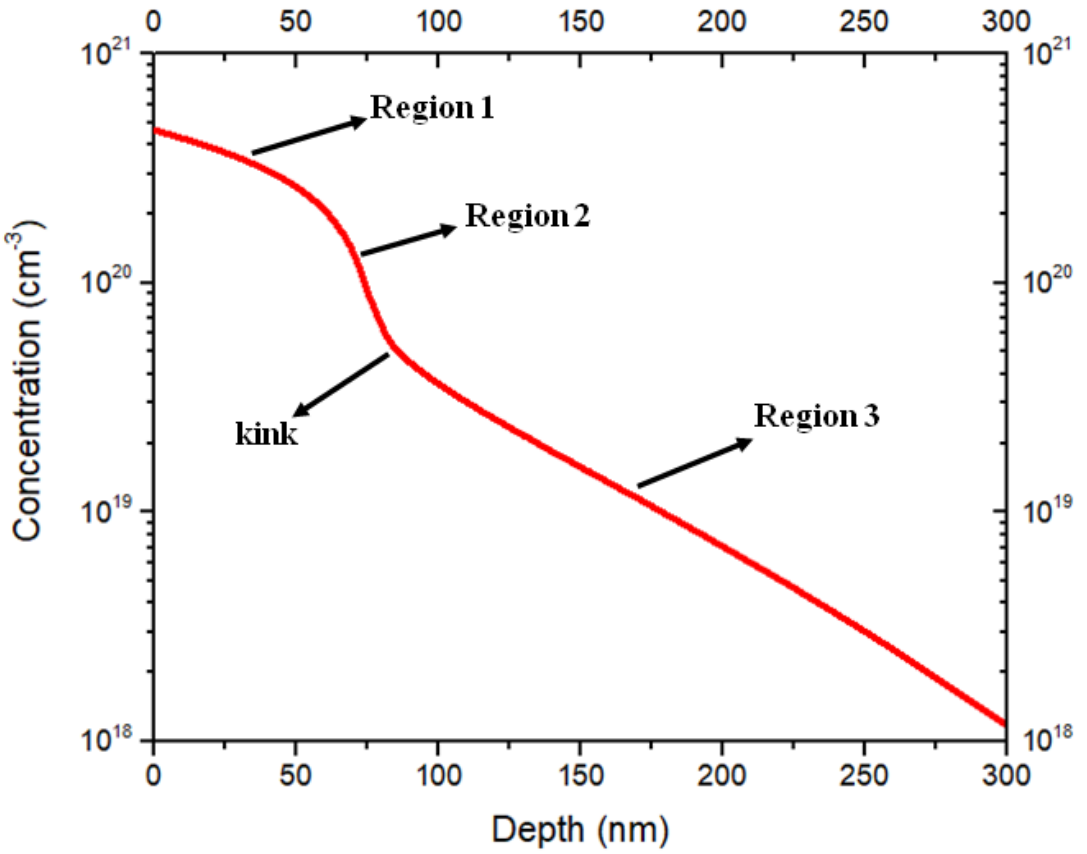


Figure 21: Simulated electrically active *P* profile for process 6 as listed in Appendix A (890 °C, 14.25 mins) as obtained in this work. Region 1 is also referred to as the plateau region. Intersection between regions 2 & 3 is referred to as the kink.

In the following subsections, a simplified model of P diffusion is explained. The model assumes that excess interstitials form due to the kick-out reaction which, as per the experimental findings of Fahey *et al.* [45], is the most likely mechanism for excess interstitial generation. It is shown that by using the pair flux equations (that were described in section 2.4), it is possible to account for non-equilibrium effects and derive an effective P diffusivity using the simplified approach of section 2.4. The suggested quantitative treatment is, however, limited to cases where the source of non-equilibrium point defect concentrations is inherent to the system. This approach might therefore find use in other studies of elemental diffusion where non-equilibrium point defect concentrations arise because of the diffusion process itself (and not because of external effects like oxidation and/or ion implantation).

The mathematical treatment explained in this section is based on the assumption that only I^0, I^-, V^- & V^{--} mediate *P* diffusion and that contribution from other point defect charged

states ($I^+, I^{++}, V^0, V^+ \,\&\, V^{++}$) are negligible. The concentration of I^+, I^{++}, V^+ and V^{++} are expected to be very low in n-type *Si* [31] and are therefore always ignored in the study of P diffusion [15, 46, 47, 60, 61]. Moreover, the contribution of V^0 to P diffusivity is also ignored in all P diffusion models [15, 46, 47, 60, 61]. Since P does not diffuse via vacancies under intrinsic conditions, there is no reason why it should diffuse via V^0 under extrinsic conditions, given that the concentration of V^0 does not change with doping. In addition, since the energy level of $I^=$ is thought to not lie within the band gap [31, 42], $I^0, I^-, V^- \,\&\, V^{--}$ are therefore the only likely point defect charged states responsible for mediating P diffusion. The overall effective diffusivity of P is then given by the sum of interstitial ($D_{(PI)^+}$and $D_{(PI)^0}$) and vacancy ($D_{(PV)^0}$ and $D_{(PV)^-}$) components of diffusivity,

$$D_P^{eff} = D_{(PI)^0} + D_{(PI)^+} + D_{(PV)^0} + D_{(PV)^-} \tag{4.10}$$

where the net charge on the P^+I^-, P^+I^0, P^+V^- and P^+V^{--} pairs is 0, +1, 0 and -1, respectively.

In most diffusion models $I^0, I^- \, and \, V^{--}$ are considered [15, 46, 47, 61] as the primary mediating species. The contribution of V^- to P diffusivity is often found to be negligible [15, 46, 47, 61]. In section 4.4, I have explained that excluding the contribution of V^- to P diffusivity improves the overall simulation accuracy over a wide range of processing conditions, and its inclusion distorts the simulated profiles for the case of very heavy doping. Therefore, in chapter 5 where the results of the simulations are discussed, the simulations have been conducted by ignoring any significant contribution of V^- vacancies to P diffusivity. However, for completeness purposes, the mathematical treatment proposed in this section takes into account P diffusivity via V^- vacancies. It must be added, that if contribution of V^- to P diffusivity is ignored, it does not mean that V^- vacancies play no role in the diffusion of P. This is because they can be involved in interstitial vacancy annihilation processes and can thus alter point defect concentrations.

In the following subsections, I begin by introducing the chemical reactions that are involved in reducing the interstitial supersaturation and are responsible for restoring point defect equilibrium. I then discuss the concentration of dopant defect pairs, since such concentrations play a crucial role in the determination of defect concentrations and thus of dopant diffusivity. The interstitial concentrations in the P diffused emitter and the subsequent diffusivity of P via interstitials is, therefore, explained after the discussion on dopant defect pair concentrations. The vacancy concentrations and the vacancy-mediated diffusivities are given in the end of this section.

4.3.1 IV Recombination during P Diffusion

We know from previous studies [46, 60, 61] that as the doping level increases there is some mechanism that reduces the interstitial supersaturation significantly (if not to its equilibrium value). This understanding arises from the P diffusion profile itself since otherwise the rapid drop in diffusivity in going from region 3 to region 2 cannot be explained. However, an important question remains. What is the mechanism that causes a suppression of the interstitial supersaturation?

In this work, it is proposed that the interstitial supersaturation associated with heavy *P* doping is not a low energy configuration for the *Si* substrate and that as the doping level increases it becomes possible for the surface injected vacancies (discussed in detail in subsection 4.5.3.2) to lower the substrate's free energy with the help of reactions R4.1 and R4.2.

$$(PI)^{+} + 2V^{0} + e^{-} \Leftrightarrow (PV)^{0} \quad \text{(R4.1)}$$

$$(PI)^{0} + 2V^{0} + e^{-} \Leftrightarrow (PV)^{-} \quad \text{(R4.2)}$$

where the pairs are formed according to the reactions,

$$P^{+} + I^{0} \Leftrightarrow (PI)^{+} \quad \text{(R4.3)}$$

$$P^+ + I^- \Leftrightarrow (PI)^0 \qquad \text{(R4.4)}$$

In the subsection 4.5.3.2, more details are given about how these reactions, and in particular the vacancies, are involved in establishing point defect equilibrium. However, it is clear from reactions R4.1 and R4.2 that as the doping level increases the rate of IV annihilation will increase.

4.3.2 Dopant Defect Pair Concentrations

The pair diffusion equations introduced in Chapter 2 were derived using the assumption that the ratio of concentration of dopant defect pairs (PX) over their intrinsic concentration is equal to the ratio of the point defect (X) concentration over its intrinsic value. For the negative interstitial and ionized phosphorus pair, this means,

$$\frac{C_{(PI)^{0,*}}}{C_{(PI)_i^{0,*}}} = \frac{C_{I^{-,*}}}{C_{I_i^{-,*}}} = \left({}^{n}/_{n_i}\right) \qquad \text{(4.11a)}$$

where the subscript (i) refers to the intrinsic case, $0/-$ is the net charge on the defect (or the dopant defect pair) and the asterisk $(*)$ is the equilibrium notation. Equation 4.11a expresses the equilibrium (*) extrinsic concentration of the defect (or the dopant defect pair) relative to its concentration under equilibrium and intrinsic (i) conditions. However, there are no P^+ ions and therefore no PI pairs in the undoped material (i). These equations only give the doping dependence factor of defect (or dopant defect pair) concentrations in an extrinsically doped material. The doping dependence of these defects arises due to the condition of local equilibrium where a defect can become charged by capturing an electron/hole, as was discussed in chapter 2.

Equation 4.11a has been experimentally found to be true under equilibrium conditions. In Appendix D of their review on diffusion theory in *Si*, Fahey *et al.* [31] examine the same assumption for the non-equilibrium case. The authors base their investigation on arsenic diffusion studies. For a dopant (A) interstitial (I) pair, the assumption examined is,

$$\frac{C_{AI}}{C_{AI^*}} = \frac{C_I}{C_{I^*}} \tag{4.11b}$$

Fahey argues that in most experimental conditions equation 4.11b is true, i.e. the assumption would hold for the non-equilibrium case as well. However, it is still not clear (from studies on arsenic diffusion [31]) whether equation 4.11b would hold if the dissociation of AI pairs, due to reaction with vacancies, reaction R4.5, takes place at a rate comparable to the rate of pair formation, reaction R4.6,

$$V + AI \Leftrightarrow A \tag{R4.5}$$

$$I + A \Leftrightarrow AI \tag{R4.6}$$

Despite the overwhelming experimental support for their validity, the problem with assumptions 4.11a and 4.11b is that they violate the law of mass action. On applying the law of mass action on reaction R4.4 we have,

$$\frac{C_{(PI)^{0,*}}}{C_{(PI)_i^{0,*}}} = \left(\frac{n}{n_i}\right)\frac{C_{I^{-,*}}}{C_{I_i^{-,*}}} = \left({}^{n}/_{n_i}\right)^2 \tag{4.11c}$$

which is in contradiction with assumption 4.11a that is actually used in pair diffusion models for the reaction R4.4.

Recently Brogioli [96] has reported on violations of the law of mass action in dilute chemical solutions. It has been found that the concentration of the products scale with the concentration of the dilute reactant only [96], given that the concentration of the dilute reactant is negligible. The reported equilibrium point defect concentrations $10^8 - 10^{15} cm^{-3}$ [27] at diffusion temperatures are negligible and if under nonequilibrium conditions the point defect concentrations are still negligible compared to dopant concentrations then equation 4.11b will hold, if the situation is treated from the perspective of violation theory. The violation theory might be helpful in explaining that equations of the type 4.11a and 4.11b can exist in real systems, however, it is still not clear to this author if the violation theory will hold for the current system.

In this work reactions R4.1 and R4.2 are used to determine the effective interstitial concentrations. It just so happens that reactions R4.1 and R4.2 are the same reactions of Fahey *et al.* [31] for the *P* dopant. If we assume the same principal for phosphorus, then as per Fahey *et al.* [31] equation 4.11d will hold if the rate of $(PI)^0$ pair formation, R4.4, is rapid compared to reaction R4.2.

$$\frac{C_{(PI)^0}}{C_{(PI)^{0,*}}} = \frac{C_{I^-}}{C_{I^{-,*}}} \tag{4.11d}$$

Likewise, if the rate of $(PI)^+$ pair formation, R4.3, is rapid compared to reaction R4.1, then we can write,

$$\frac{C_{(PI)^+}}{C_{(PI)^{+,*}}} = \frac{C_{I^0}}{C_{I^{0,*}}} \tag{4.11e}$$

where (* & i) represent the undoped (intrinsic, i) material under equilibrium (*) conditions. The absence of intrinsic (i) refers to the extrinsically doped material, i.e., the material with electron (donor) concentration greater than the intrinsic carrier concentration at diffusion temperatures.

4.3.3 Interstitial Concentrations

Excess interstitial generation takes place throughout the P emitter due to kick out reactions. It is argued, that due to their electron concentration dependence, reactions R4.1 and R4.2 are not able to significantly reduce the interstitial supersaturation at low doping levels (region 3) but are able to completely suppress the supersaturation at high doping levels (region 1). The excess interstitial concentrations are then simply given by the differences in their generation rates due to the kick out reactions and their annihilation rates via reactions R4.1 and R4.2.

The overall effect of these two opposing types of reactions is an increasing interstitial concentration (supersaturation) with decreasing electron concentrations. The maximum supersaturation of self interstitials is then expected to be located at the diffusion front (at the

diffusing junction or at low doping level). Owing to their very high diffusivity, interstitials generated at the diffusion front will be able to diffuse rapidly into the wafer bulk, thereby resulting in an almost flat interstitial profile beyond the diffusion front. The interstitial supersaturation thus falls from a maximum constant value in the bulk to its equilibrium value at the very high doping levels near the surface.

In this subsection, an approximation for the interstitial profile in the diffused *P* regions is explained. This is done by first defining a constant interstitial supersaturation factor defined in the absence of reactions R4.1 and R4.2. The interstitial profile inside the emitter is determined by an effective supersaturation factor that takes into account the *IV* recombination processes associated with reactions R4.1 and R4.2. The effective supersaturation is seen as a reduction over the constant supersaturation factor observed in the wafer bulk.

4.3.3.1 Supersaturation Factor

Consider the hypothetical chemical reactions, R0 and R1, that take place inside the emitter and are able to generate constant interstitial supersaturations, S_0 & S_1, that are functions of temperature only,

$$\frac{C_I^0}{C_I^{0,*}} = S_0 \tag{4.12a}$$

$$\frac{C_I^-}{C_I^{-,*}} = S_1 \tag{4.12b}$$

One is often interested in the actual concentration of these defects relative to their concentrations under equilibrium and intrinsic conditions. For reactions like R0 and R1 we can write this as the product of the supersaturation factor and the relative equilibrium concentration,

$$\left(\frac{C_{I^0}}{C_{I_i^{0,*}}}\right)_{R0} = \frac{C_{I^0}}{C_{I^{0,*}}}\frac{C_{I^{0,*}}}{C_{I_i^{0,*}}} = S_0 \times 1 = S_0 \tag{4.12c}$$

$$\left(\frac{C_{I^-}}{C_{I_i^{-,*}}}\right)_{R1} = \frac{C_{I^-}}{C_{I^{-,*}}}\frac{C_{I^{-,*}}}{C_{I_i^{-,*}}} = S_1\,\frac{n}{n_i} \tag{4.12d}$$

which is also true for the corresponding pairs due to relations 4.11d and 4.11e.

$$\left(\frac{C_{(PI)^+}}{C_{(PI)_i^{+,*}}}\right)_{R0} = \frac{C_{(PI)^+}}{C_{(PI)^{+,*}}}\frac{C_{(PI)^{+,*}}}{C_{(PI)_i^{+,*}}} = S_0 \tag{4.13a}$$

$$\left(\frac{C_{(PI)^0}}{C_{(PI)_i^{0,*}}}\right)_{R1} = \frac{C_{(PI)^0}}{C_{(PI)^{0,*}}}\frac{C_{(PI)^{0,*}}}{C_{(PI)_i^{0,*}}} = S_1\,\frac{n}{n_i} \tag{4.13b}$$

where the subscript R0 (R1) refer to the fact that the associated concentration ratio is due to reaction R0 (R1), as one would expect in the absence of external influences.

The hypothetical reactions R0 and R1 suggest that the generation rate of I^0 is a constant and that of I^- increases with the electron concentration. This is consistent with the reported phenomena responsible for excess interstitial generation [45]. In [45] it was reported that the most likely candidate for excess interstitial generation is the reverse kick out reaction,

$$Si + P_i \Leftrightarrow P_s + I^0 \tag{R4.7}$$

$$Si + P_i + e^- \Leftrightarrow P_s + I^- \tag{R4.8}$$

where Si is a silicon lattice atom and P_s and P_i are P atoms in substitutional and interstitial sites, respectively. Interstitial profiles in the wafer bulk ahead of the diffused emitter ($n < n_i$) are essentially flat, due to the rapid interstitial diffusivities as was pointed out earlier, and supersaturated at S_0 & S_1.

4.3.3.2 Dissociation & Recombination Processes

In 1985 Hu [97] analyzed the relation,

$$C_I C_V = C_I^* C_V^* \tag{4.14a}$$

which Sirtl [98] had suggested would hold under steady state. From the point of view of self-interstitial injection during oxidation, Hu [97] concluded that the approximation in relation

4.14a would, under oxidizing conditions, only hold for regions away from the Si surface. In addition, both theoretical analysis of the point defect flux equations and experimental observations had suggested [97] that in regions close to the Si surface, relation 4.14a was invalid. Instead, theoretical results suggested relation 4.14b, which was later also obtained by Yeager and Dutton [99], to be valid near the Si surface. The normalized point defect concentration profile is plotted in Figure 22, wherein the vacancy undersaturation ($U = C_V/C_V^*$) is depicted by the solid red line while the dashed blue line represents the vacancy undersaturation according to equation 4.14a.

$$C_I C_V > C_I^* C_V^* \tag{4.14b}$$

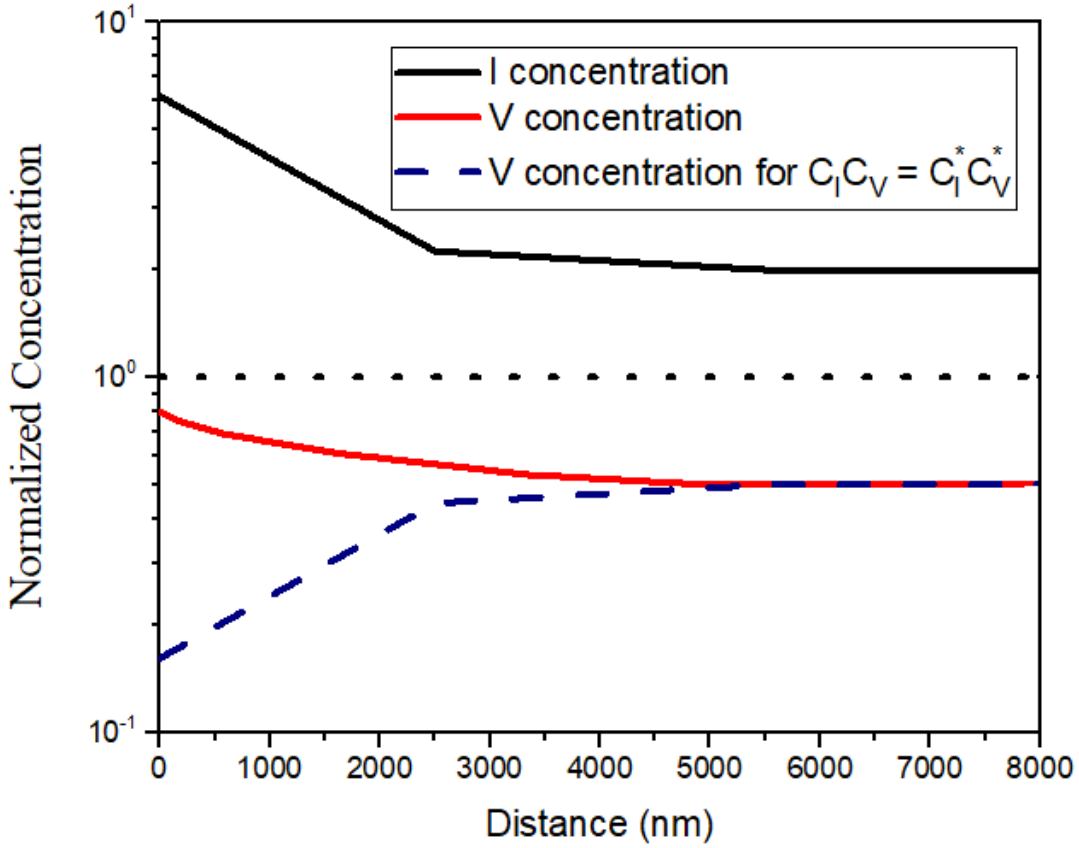


Figure 22: [97] Normalized interstitial (solid black) and vacancy (solid red) concentrations as a function of depth into the wafer. Dashed blue line represents the normalized vacancy concentrations as per relation 4.14a ($C_I C_V = C_I^* C_V^*$). The vacancy profile (solid red line) scales according to relation 4.14b ($C_I C_V > C_I^* C_V^*$) near the Si surface and according to relation 4.14a in regions further away from the Si surface. The dotted black line depicts the value of 1.

The reason for the increased vacancy concentration near the Si surface is that there exists a driving for the surface vacancy concentration to attain an equilibrium concentration. Under

equilibrium (non-oxidizing) conditions the flux of vacancies into the wafer equals the flux of vacancies out of the wafer. On the hand, during oxidation the excess interstitials result in a reduction in the vacancy concentrations (due to IV recombination) near the surface. This disturbs the balance between the flux in and the flux out at the surface, resulting in the injection of vacancies from the surface. The flux of injected vacancies can be expressed as,

$$J_V = -\sigma(C_V - C_V^*) \tag{4.15}$$

where σ is the surface recombination velocity with units of cms^{-1}.

The rate limiting factor for vacancy injection in equation is $(C_V - C_V^*)$ instead of σ. However, the IV recombination rate near the surface is not rapid in comparison to the vacancy influx, which gives rise to the vacancy concentration profile (solid red line) depicted in Figure 22. Moreover, due to the rapid diffusivities of point defects, equation 4.14b is valid for depths of a few micrometers (~5μm), for even very short annealing durations (1-10 seconds) [99]. Note that the depth to which equation 4.14b will hold stabilizes around a fixed value (e.g. ~5μm) as the annealing duration increases. Beyond this depth (~5μm) equation 4.14a holds since the vacancy influx is no longer rapid compared to the IV recombination rate.

The interstitial supersaturation ($S = C_I/C_I^*$) that exists during P diffusion is one to two orders in magnitude [45] as opposed to an interstitial supersaturation of 1.5-4 [100] that arises due to oxidation. The effect of the interstitial supersaturation due to thermal oxidation is likely to be suppressed in the background of the very large interstitial supersaturation arising due to (possibly) the kick-out reactions. In the context of P diffusion the interstitial supersaturation due to oxidation can therefore be ignored. We might also say that the deviation of the product $C_I C_V$ (from the product $C_I^* C_V^*$) due to thermal oxidation is of little significance during P diffusion. The very large undersaturation of vacancies inside the emitter, arising due to the kick out reactions, will result in a large driving force for vacancy injection from the surface (equation 4.15) into the emitter. If we assume that vacancies can be injected with a rate (σ)

similar to that of the kick out reactions (i.e., the rate of interstitial generation), then the *IV* recombination rate will determine the point defect concentration profile within the emitter.

When the P concentration at the Si surface is low such that regions 1 and 2 have not yet formed, the resulting P concentrations and the *IV* recombination rates (due to reactions R4.1 and R4.2) in the emitter would be low. As a result the point defect concentration profiles within the P diffused emitter are similar to that depicted in Figure 22, with the notable exceptions that the amount of interstitial (vacancy) supersaturation (undersaturation) is large and that the emitter itself is acting as the primary source of excess interstitial generation. In addition, it is noteworthy to point that the depth of the emitter is in most cases very shallow (~ 0.5 μm) compared to the depth beyond which equation 4.14a becomes valid. Therefore, for low surface concentrations, with the P profile comprising only of the tail region, we expect equation 4.14b to hold throughout the P concentration profile.

For high P concentrations near the Si surface, the *IV* recombination rates due to reactions R4.1 and R4.2 can become rapid compared to the vacancy influx from the surface. Therefore, in region 1 of the P profile where the doping level is high, the point defect concentrations conform to the form suggested in equation 4.14a. Moreover, since the vacancy concentration at the surface attempts to attain an equilibrium concentration, in region 1 of the P profile the point defect concentrations will approach their equilibrium values. As the doping level falls (away from the surface) and the *IV* recombination rates becomes slow with respect to the vacancy influx, the point defect concentrations will begin to scale according to equation 4.14b. A qualitative picture of the interstitial (blue) and vacancy (solid red) normalized concentration profile in the three regions of the P diffused emitter is shown in Figure 23, where for clarity purposes a deep hypothetical P profile is indicated.

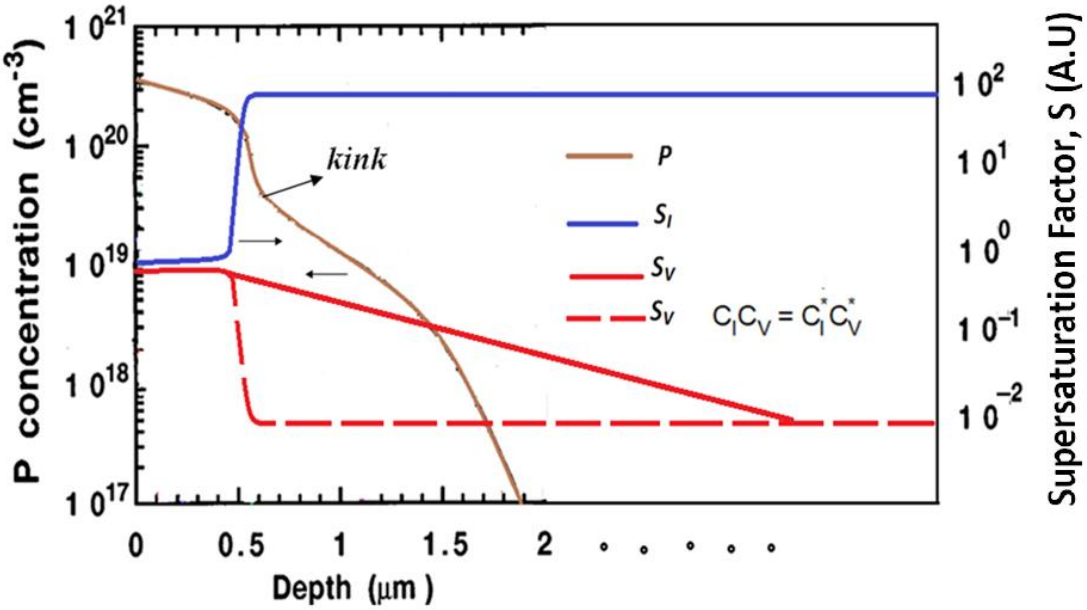


Figure 23: Phosphorus concentration (brown) and normalized interstitial (blue) and vacancy (solid red) concentrations as a function of depth into the wafer. Dashed red line represents the normalized vacancy concentrations as per relation 4.14a ($C_I C_V = C_I^* C_V^*$). The vacancy profile (solid red line) scales according to relation 4.14a in region 1 and according to relation 4.14b ($C_I C_V > C_I^* C_V^*$) in regions 2 and 3 of the P profile.

Since reactions R4.1 and R4.2 play a crucial role in the suppression of the interstitial supersaturation, it is important to take a closer look at these reactions. In the reaction sequences of R4.1

$$V^0 + e^- \Leftrightarrow V^-, \quad (PI)^+ \Leftrightarrow P^+ + I^0, \quad P^+ + V^- \Leftrightarrow (PV)^0, \quad I^0 + V^0 \Leftrightarrow Si$$

and R4.2,

$$V^0 + e^- \Leftrightarrow V^-, \quad (PI)^0 \Leftrightarrow P^+ + I^0 + e^-,$$

$$P^+ + V^- + e^- \Leftrightarrow P^+ + V^{--} \Leftrightarrow (PV)^-, \quad I^0 + V^0 \Leftrightarrow Si$$

V^- and V^{--} are thought to play a very important role in the suppression of I^0 and I^-, respectively. When V^- approaches a P^+I^0 pair, the ionized phosphorus atom can, due to increased Columbic attraction, pair with the vacancy to form the $(PV)^0$ pair. As a result of the higher attraction between P^+ and V^- the P^+I^0 pair will dissociate, thereby releasing the excess interstitial, I^0, which can now recombine with a neutral vacancy, V^0.

A slightly different, but otherwise similar, explanation follows for the case of $(PV)^-$ pair formation, which results in a reduction in the I^- concentration. In this case, V^- can approach the P^+I^- pair and can capture the electron from I^-, thereby becoming V^{--} and leaving the interstitial neutrally charged. The converse (I^- capturing an electron from the approaching V^-) is, however, not likely since the energy level of the doubly negative interstitial $I^=$ is not thought to lie within the bandgap [42]. The net effect in this case is then an increased Columbic interaction between the dopant, P^+, and the vacancy, V^{--}, which will result in the dissociation of the dopant interstitial pair and the subsequent recombination of the interstitial with a vacancy.

In general, the pair binding energy is both a function of the Columbic interaction and the lattice distortion. The most common opinion about [101] lattice distortion for the substitutional dopants (B, P, As, Sb) in Si is that the larger atoms (As, Sb) would be attracted to vacancies as opposed to the smaller atoms (B, P) that would be repelled by vacancies. However, for P an affinity for vacancies is thought to exist [102], as there appears to be an attraction between the two species beyond the expected Columbic interaction [42, 102]. This might be due to the similar size of P and Si. Nevertheless, we should still expect the binding energy of the PV pair, due to lattice distortion, to be less compared to that of the PI pair. Otherwise, P^+V^0 pairs instead of P^+I^0 pairs should mediate the diffusivity of P under intrinsic conditions, which is clearly not the case [56]. This implies that for the PI pair to dissociate and form a PV pair, as is argued in this work, the Columbic attraction for the PV pair must exceed that of the PI pair.

4.3.3.3 Effective Supersaturation Factors

In R4.1 and R4.2 the reaction sequences are lumped together as single reactions. We can use such reactions and determine the mass action relationships for PI pairs. In this subsection an approximation for the interstitial profiles inside the emitter is derived by taking into account both the supersaturation reactions and the recombination reactions. As was pointed out in

section 4.3.3.2, vacancy injection can be ignored when determining point defect concentrations due to their significantly lower rates compared to the kick out reactions and reactions R4.1 and R4.2.

It is assumed that PI pair formations is rapid compared to R4.1 and R4.2 so that we may use relations 4.11d and 4.11e. Moreover, pair formations are also assumed to be rapid compared to the reactions generating excess interstitials R0 and R1. This means that pair formation rates are not a limiting factor in the determination of pair concentrations, and we may write the effective pair concentration ratios as,

$$\left(\frac{C_{(PI)^+}}{C_{(PI)_i^{+,*}}}\right)_{effective} = \left(\frac{C_{(PI)^+}}{C_{(PI)_i^{+,*}}}\right)_{R0} - \left(\frac{C_{(PI)^+}}{C_{(PI)_i^{+,*}}}\right)_{(R4.1)} \tag{4.16a}$$

$$\left(\frac{C_{(PI)^0}}{C_{(PI)_i^{0,*}}}\right)_{effective} = \left(\frac{C_{(PI)^0}}{C_{(PI)_i^{0,*}}}\right)_{R1} - \left(\frac{C_{(PI)^0}}{C_{(PI)_i^{0,*}}}\right)_{(R4.2)} \tag{4.16b}$$

The term to the right in equations 4.16a and 4.16b are the ratios of the dissociated pair concentrations in the supersaturated extrinsic material to the dissociated pair concentrations in the intrinsic material (i) under equilibrium ($*$) conditions. However, there is no driving force for R4.1 and R4.2 in the intrinsic material under equilibrium. These terms are only approximations to account for the doping dependence of the recombination processes. A driving force for R4.1 and R4.2 only exists because of the non-equilibrium interstitial concentrations.

$\left(C_{(PI)^+}/C_{(PI)_i^{+,*}}\right)_{(R4.1)}$ can be interpreted as the dissociated concentration ratio due to R4.1 in a system with a constant driving force, S_0. Using the law of mass action we can determine such a ratio at a hypothetical electron concentration n_{k1} where the concentration of V^- is now high enough such that the reaction rate of R4.1 is equal to that of reaction R0.

$$\frac{C_{(PI)^+}(C_{V^0})^2 n_{k1}}{C_{(PV)^0}} = \frac{C_{(PI)_i^{+,*}}\left(C_{V_i^{0,*}}\right)^2 n_i}{C_{(PV)_i^{0,*}}} \tag{4.17a}$$

$$\left(\frac{C_{(PI)^+}}{C_{(PI)_i^{+,*}}}\right)_{(R4.1)} = \frac{C_{(PV)^0}}{C_{(PV)_i^{0,*}}}\left(\frac{C_{V_i^{0,*}}}{C_{V^0}}\right)^2 \frac{n_i}{n_{k1}} \tag{4.17b}$$

$$\left(\frac{C_{(PI)^{+,*}}}{C_{(PI)_i^{+,*}}}\right)_{(R4.1)} = \frac{1}{S_0}\frac{n}{n_i}(S \times 1)^2 \frac{n_i}{n_{k1}} \tag{4.17c}$$

$$\left(\frac{C_{(PI)^{+,*}}}{C_{(PI)_i^{+,*}}}\right)_{(R4.1)} = S_0 \frac{n}{n_{k1}} \tag{4.17d}$$

Using the same method at n_{k2} where the concentration of V^{--} is now high enough such that reaction rate of R4.2 is equal to that of reaction R1.

$$\left(\frac{C_{(PI)^{0,*}}}{C_{(PI)_i^{0,*}}}\right)_{(R4.2)} = S_1 \frac{n^2}{n_i n_{k2}} \tag{4.17e}$$

The effective concentration of pairs then becomes,

$$\left(\frac{C_{(PI)^+}}{C_{(PI)_i^{+,*}}}\right)_{eff} = S_0 \times \left[1 - \frac{n}{n_{k1}}\right] \tag{4.18a}$$

$$\left(\frac{C_{(PI)^0}}{C_{(PI)_i^{0,*}}}\right)_{eff} = S_1 \times \left[\left(\frac{n}{n_i}\right) - \frac{n^2}{n_i n_{k2}}\right] \tag{4.18b}$$

where equations 4.13a and 4.13b have been substituted for the terms $\left(C_{(PI)^+}/C_{(PI)_i^{+,*}}\right)_{R0}$ and $\left(C_{(PI)^+}/C_{(PI)_i^{+,*}}\right)_{R1}$, respectively.

Due to conditions 4.11a, 4.11b and 4.11c, the interstitial concentrations must also scale accordingly,

$$\left(\frac{C_{I^0}}{C_{I_i^{0,*}}}\right)_{eff} = S_0 \times \left[1 - \frac{n}{n_{k1}}\right] \tag{4.19a}$$

$$\left(\frac{C_{I^-}}{C_{I_i^{-,*}}}\right)_{eff} = S_1 \times \left[\left(\frac{n}{n_i}\right) - \frac{n^2}{n_i n_{k2}}\right] \tag{4.19b}$$

Using equations 4.18a – 4.19b we can find the ratio of the actual concentration of the defect/pair inside the emitter to its concentration under equilibrium & intrinsic conditions. Such ratios can be used directly in the diffusivity equation.

Equations 4.18a – 4.19b are not valid for the entire range of electron concentration and only extrapolate the interstitial and pair concentrations with n. In an equilibrium system there is no net driving force for R4.1 and R4.2. The interstitial and thus the pair concentrations cannot fall below their equilibrium values.

Using equations 4.19a and 4.19b we can also approximate the effective supersaturation factors,

$$S^0_{eff} = \left(\frac{C_{I^0}}{C_{I^0,*}}\right)_{eff} = S_0 \times \left[1 - \frac{n}{n_{k1}}\right] \tag{4.20a}$$

$$S^1_{eff} = \left(\frac{C_{I^-}}{C_{I^-,*}}\right)_{eff} = S_1 \times \left[1 - \frac{n}{n_{k2}}\right] \tag{4.20b}$$

The effective supersaturation factors do not fall below 1.

4.3.4 Interstitial Mediated Diffusion Equations

The flux of PI pairs can be computed using the method outlined in Chapter 2 and by using the effective concentrations in 4.18a – 4.19b. In the following the diffusivity due to $(PI)^+$ pairs is derived from the flux equation,

$$J_{(PI)^+} = -d_{(PI)^+}\frac{\partial C_{(PI)^+}}{\partial x} + (1-m)\mu_{P^+I^0} C_{(PI)^+}\vec{E} \tag{4.21a}$$

$$J_{(PI)^+} = -d_{(PI)^+}\frac{C_{(PI)^+}}{C_P^+}\frac{\partial C_P^+}{\partial x} - d_{(PI)^+}\frac{C_{(PI)^+}}{C_I^0}\frac{\partial C_I^0}{\partial x} + (1-0)\left(\frac{q}{KT}d_{(PI)^+}\right)C_{(PI)^+}\left(-\frac{KT}{qC_P^+}\frac{\partial C_P^+}{\partial x}\right) \tag{4.21b}$$

$$J_{(PI)^+} = -d_{(PI)^+}\frac{C_{(PI)^+}}{C_P^+}\frac{\partial C_P^+}{\partial x} - d_{(PI)^+}\frac{C_{(PI)^+}}{C_I^0}\frac{\partial C_I^0}{\partial x} - d_{(PI)^+}\frac{C_{(PI)^+}}{C_P^+}\frac{\partial C_P^+}{\partial x} \tag{4.21c}$$

$$J_{(PI)^+} = -2d_{(PI)^+}\frac{C_{(PI)^+}}{C_P^+}\frac{\partial C_P^+}{\partial x} - d_{(PI)^+}\frac{C_{(PI)^+}}{C_I^0}\frac{\partial C_I^0}{\partial x} \tag{4.21d}$$

Using 4.18a – 4.19b, we replace $C_{(PI)^+}$ and C_I^0 with the following,

$$C_{(PI)^+} = C_{(PI)_i^{+,*}} S_0\left(1 - \frac{n}{n_{k1}}\right) \tag{4.21e}$$

$$C_{I^0} = C_{I_i^{0,*}} S_0\left(1 - \frac{n}{n_{k1}}\right) \tag{4.21f}$$

The flux equation becomes,

$$J_{(PI)^+} = -2d_{(PI)^+}\frac{C_{(PI)_i^{+,*}}}{C_P^+} S_0\left(1 - \frac{n}{n_{k1}}\right)\frac{\partial C_P^+}{\partial x} - d_{(PI)^+}\frac{C_{(PI)_i^{+,*}} S_0\left(1 - \frac{n}{n_{k1}}\right)}{C_{I_i^{0,*}} S_0\left(1 - \frac{n}{n_{k1}}\right)}\frac{\partial C_I^0}{\partial x} \tag{4.21g}$$

$$J_{(PI)^+} = -2D_{(PI)_i^{+,*}} S_0\left(1 - \frac{n}{n_{k1}}\right)\frac{\partial C_P^+}{\partial x} - d_{(PI)^+}\frac{C_{(PI)_i^{+,*}}}{C_P^+}\frac{C_P^+}{C_{I_i^{0,*}}}\left(-S_0 C_{I_i^{0,*}}\frac{1}{n_{k1}}\frac{\partial n}{\partial x}\right) \tag{4.21h}$$

$$J_{(PI)^+} = -2D_{(PI)_i^{+,*}} S_0\left(1 - \frac{n}{n_{k1}}\right)\frac{\partial C_P^+}{\partial x} + D_{(PI)_i^{+,*}}\left(S_0\left(\frac{n}{n_{k1}}\right)\frac{\partial C_P^+}{\partial x}\right) \tag{4.21i}$$

$$J_{(PI)^+} = -D_{(PI)_i^{+,*}} S_0\left(2 - 3\frac{n}{n_{k1}}\right)\frac{\partial C_P^+}{\partial x} \tag{4.21j}$$

$$J_{(PI)^+} = -2D_{(PI)_i^{+,*}} S_0 \left(1 - \frac{3n}{2n_{k1}}\right) \frac{\partial C_P^+}{\partial x} \tag{4.22a}$$

If it is desirable to write the flux equation inclusive of the field enhancement factor, we can write the flux and the corresponding effective interstitial diffusivity as,

$$J_{(PI)^+} = -2D_{(PI)_i^{+,*}} \frac{S_0}{h} \left(1 - \frac{3n}{2n_{k1}}\right) \frac{\partial C_P^+}{\partial x} \tag{4.22b}$$

$$D_{(PI)^+} = D_{(PI)_i^{+,*}} \frac{S_0}{h} \left(1 - \frac{3n}{2n_{k1}}\right) \tag{4.22c}$$

Alternately, the factor of 2 in equation 4.22a can be taken as the field enhancement factor as was discussed in section 2.4 (see discussion pertaining to equation 2.18b). The effective interstitial diffusivity then becomes,

$$D_{(PI)^+} = D_{(PI)_i^{+,*}} S_0 \left(1 - \frac{3n}{2n_{k1}}\right) \tag{4.22d}$$

The interstitial diffusivity extrapolates to zero prior to the extrapolation of interstitial concentration to zero in equation 4.19a i.e. the electron concentration at which $D_{(PI)^+}$ extrapolates to zero is smaller than the electron concentrations at which $C_{(PI)^+}$ extrapolates to zero. This difference arises because the diffusion component in the flux equation also scales with the gradient in point defect concentration. In reality, the interstitial diffusivity must not fall below its equilibrium value.

$$D_{(PI)^+} = \begin{cases} D_{(PI)_i^{+,*}} S_0 \left(1 - \dfrac{3n}{2n_{k1}}\right), & n \leq \dfrac{2}{3}\left(\dfrac{S_0 - 1}{S_0}\right) n_{k1} \\ D_{(PI)_i^{+,*}}, & elsewhere \end{cases} \tag{4.23}$$

Using the same procedure it can be shown that the diffusivity due to $(PI)^0$ pairs is given by,

$$D_{(PI)^0} = \begin{cases} D_{(PI)_i^{0,*}} S_1 \left(\left(\dfrac{n}{n_i}\right) - \dfrac{3n^2}{2n_i n_{k2}}\right), & n \leq \dfrac{2}{3}(S_1 - 1) n_{k2} \\ D_{(PI)_i^{0,*}} \left(\dfrac{n}{n_i}\right), & elsewhere \end{cases} \tag{4.24}$$

4.3.5 Vacancy Mediated P Diffusion

In section 4.3.3.2 it was pointed out that the use of equation 4.14a in determining the vacancy undersaturation ($U = C_V/C_V^*$) is only valid in region 1 of the P profile where IV recombination rates due to reactions R4.1 and R4.2 are rapid. However, in this subsection the vacancy diffusivity is determined by using equation 4.14a as an approximation for the vacancy concentrations in all the three regions of the P diffused emitter. As will be noted in the end of this subsection, this approximation results in a negligible error in the effective diffusivity of P.

The reaction sequences of reaction R4.1, that were explained in section 4.3.3.2, suggest that the IV annihilation process involves the interstitial I^0 and the vacancy V^-. Similarly the reaction sequences of reaction R4.2 involves the interstitial I^- and the vacancy V^{--}. The vacancy concentrations can thus be approximated by,

$$C_{I^0} C_{V^-} = C_{I^{0,*}} C_{V^{-,*}} \tag{4.25a}$$

$$C_{I^-} C_{V^{--}} = C_{I^{-,*}} C_{V^{--,*}} \tag{4.25b}$$

where $C_{I^0}/C_{I^{0,*}}$ and $C_{I^-}/C_{I^{-,*}}$ are the effective interstitial supersaturation factors in equations 4.20a – 4.20b. Therefore, the effective vacancy undersaturation factors are,

$$\frac{C_{V^-}}{C_{V^{-,*}}} = \frac{C_{I^{0,*}}}{C_{I^0}} = \frac{n_{k1}}{S_0(n_{k1} - n)} \tag{4.26a}$$

$$\frac{C_{V^{--}}}{C_{V^{--,*}}} = \frac{C_{I^{-,*}}}{C_{I^-}} = \frac{n_{k2}}{S_1(n_{k2} - n)} \tag{4.26b}$$

Recall that n_{k1} (n_{k2}) corresponds to that electron concentration where the reaction rate of reactions R4.1 (R4.2) is equal to the reaction rate of the kick out reaction that results in the generation of excess I^0 (I^-). The reaction rates for reactions R4.1 and R4.2 increase with electron concentrations.

The effective concentration of vacancies and of phosphorus vacancy pairs relative to their concentration in intrinsic (i) material under equilibrium conditions (*) then becomes,

$$\left(\frac{C_{V^-}}{C_{V_i^{-,*}}}\right)_{eff} = \left(\frac{C_{(PV)^0}}{C_{(PV)_i^{0,*}}}\right)_{eff} = \frac{n_{k1}}{S_0(n_{k1}-n)}\left(\frac{n}{n_i}\right) \tag{4.27a}$$

$$\left(\frac{C_{V^{--}}}{C_{V_i^{--,*}}}\right)_{eff} = \left(\frac{C_{(PV)^-}}{C_{(PV)_i^{-,*}}}\right)_{eff} = \frac{n_{k2}}{S_1(n_{k2}-n)}\left(\frac{n}{n_i}\right)^2 \tag{4.27b}$$

The concentrations of vacancies become,

$$C_{V^-} = C_{V_i^{-,*}}\ \frac{n_{k1}}{S_0(n_{k1}-n)}\left(\frac{n}{n_i}\right) \tag{4.28a}$$

$$C_{V^{--}} = C_{V_i^{--,*}}\ \frac{n_{k2}}{S_1(n_{k2}-n)}\left(\frac{n}{n_i}\right)^2 \tag{4.28b}$$

Using the method outlined in section 2.4 and described for the case of interstitials in section 4.3.4, it can be shown that the effective vacancy diffusivities are given by,

$$D_{(PV)^0} = D_{(PV)_i^{0,*}}\left(\frac{n}{n_i}\right)\frac{n_{k1}}{S_0 h(n_{k1}-n)}\left(\frac{nn_{k1}}{(n_{k1}-n)}+1\right) \tag{4.29a}$$

$$D_{(PV)^-} = D_{(PV)_i^{-,*}}\left(\frac{n}{n_i}\right)^2\frac{1}{S_1 h}\left(\frac{2n_{k2}^2-nn_{k2}}{(n_{k2}-n)^2}\right) \tag{4.29b}$$

Introducing the vacancy percolation effect by using the term from Dunham *et al.* [32], equation 2.22 in section 2.5.1, the new diffusivity equations are given by,

$$D_{(PV)^0} = D_{(PV)_i^{0,*}}\left(\frac{n}{n_i}\right)\frac{n_{k1}}{S_0 h(n_{k1}-n)}\left(\frac{nn_{k1}}{(n_{k1}-n)}+1\right)\left\{1 + \left(\frac{C_P^+}{C^{Th}}\right)^m\right\} \tag{4.30a}$$

$$D_{(PV)^-} = D_{(PV)_i^{-,*}}\left(\frac{n}{n_i}\right)^2\frac{1}{S_1 h}\left(\frac{2n_{k2}^2-nn_{k2}}{(n_{k2}-n)^2}\right)\left\{1+\left(\frac{C_P^+}{C^{Th}}\right)^m\right\} \tag{4.30b}$$

where C^{Th} refers to the vacancy percolation threshold concentration. It is pertinent to mention that similar to the case of interstitial diffusivities, the vacancy diffusivities are also limited by their equilibrium values.

$$D_{(PV)^0} \tag{4.31}$$

$$= \begin{cases} D_{(PV)_i^{0,*}}\left(\frac{n}{n_i}\right)\left\{1+\left(\frac{C_P^+}{C^{Th}}\right)^m\right\}, & S_0\left(1-\frac{n}{n_{k2}}\right) \le 1 \\ D_{(PV)_i^{0,*}}\left(\frac{n}{n_i}\right)\left\{1+\left(\frac{C_P^+}{C^{Th}}\right)^m\right\}, & \frac{n_{k1}}{S_0 h(n_{k1}-n)}\left(\frac{nn_{k1}}{(n_{k1}-n)}+1\right) > 1 \\ D_{(PV)_i^{0,*}}\left(\frac{n}{n_i}\right)\frac{n_{k1}}{S_0 h(n_{k1}-n)}\left(\frac{nn_{k1}}{(n_{k1}-n)}+1\right)\left\{1+\left(\frac{C_P^+}{C^{Th}}\right)^m\right\}, & elsewhere \end{cases}$$

$$D_{(PV)^-} \tag{4.32}$$

$$= \begin{cases} D_{(PV)_i^{-,*}}\left(\frac{n}{n_i}\right)^{22}\left\{1+\left(\frac{C_P^+}{C^{Th}}\right)^m\right\}, & S_1\left(1-\frac{n}{n_{k2}}\right) \le 1 \\ D_{(PV)_i^{-,*}}\left(\frac{n}{n_i}\right)^2\left\{1+\left(\frac{C_P^+}{C^{Th}}\right)^m\right\}, & \frac{1}{S_1 h}\left(\frac{2n_{k2}^2-nn_{k2}}{(n_{k2}-n)^2}\right) > 1 \\ D_{(PV)_i^{-,*}}\left(\frac{n}{n_i}\right)^2\frac{1}{S_1 h}\left(\frac{2n_{k2}^2-nn_{k2}}{(n_{k2}-n)^2}\right)\left\{1+\left(\frac{C_P^+}{C^{Th}}\right)^m\right\}, & elsewhere \end{cases}$$

In section 4.4, it is discussed that the contribution of $D_{(PV)^0}$ to overall dopant diffusivity must be negligible in order to account for the shape of the P profile under various diffusion temperatures and doping levels. In addition, the diffusivity of vacancies in general and of $D_{(PV)^-}$ in particular is very small in region 2 and negligible in region 3 due to the low electron concentrations in these regions. This implies that the error introduced in the vacancy diffusivities in regions 2 and 3 by the use of relation 4.14a is negligible in the context of the overall P diffusivity. As will be discussed in chapter 5, the overall effective P diffusivity is dominated by $D_{(PI)^0}$ in region 2 and by $D_{(PV)^-}$ in region 1, where point defects are in equilibrium. This in turn means that we can approximate the vacancy diffusivity, $D_{(PV)^-}$, by its equilibrium value without any need of taking into account the vacancy undersaturation and that equation 4.33 is sufficient to account for the vacancy mediated diffusion of P.

$$D_{(PV)^-} = D_{(PV)^{-,*}} = D_{(PV)_i^{-,*}} \left(\frac{n}{n_i}\right)^2 \left\{1 + \left(\frac{C_P^+}{C^{Th}}\right)^m\right\} \quad (4.33)$$

4.4 Considerations in the determination of constants

The diffusion model developed in this work and discussed in section 4.3 requires ten constants. On the other hand, the equations (that were discussed in section 4.2) for the determination of the phosphorus concentration at the silicon surface, C_{Si}, and the Dunham precipitation model (discussed in sections 2.5.2.1 and 2.5.2.2) each require four constants. The constants used in the equations for the determination of C_{Si} are given in Appendix B while the constants for the diffusion and precipitation models are given at the end of this section in Tables 1 & 2, respectively.

The constants reported in the Dunham precipitation model [64] are a_1, a_2, a_3 and C_{ss}, where a_1 is a constant for the precipitate/matrix interface energy, a_2 and a_3 are constants for the strain energy and C_{ss} corresponds to the solubility limit. The values reported for these constants by Dunham allowed reasonable agreement of simulated precipitation kinetics with the experimental data of Nobili *et al.* [9]. Dunham assumed the constants a_1, a_2 and a_3 to be temperature independent but pointed out that some of the constants pertaining to the precipitate strain energy might not be temperature independent. Despite the assumptions and the very different temperature range (300-750 ºC) used in the Dunham study, the constants reported in that work can be used as a good starting point in the determination of the actual (best possible) constant values.

Several key issues need to be considered in the determination of the constants that are used in the precipitation model (discussed in sections 2.5.2.1 and 2.5.2.2) and the P diffusion model (discussed in section 4.3). The first is that the constants must be defined by a single Arrhenius expression and should, therefore, have the same value at a given temperature (i.e. for processes 1-6 and 10-15, which were all conducted at 890 ºC). Secondly, very good

agreement between simulated and experimental total P should be obtained. Good agreement between simulated and experimental electrically active P profiles is also important. However, since experimental electrically active P profiles could not be obtained in this work, the simulated electrical profiles cannot be validated.

The correlation between total and electrically active P obtained by Fair & Tsai [15] can only be used as a first order approximation and not as a validity check for the simulated electrical profiles. This is because the empirical form of Fair & Tsai does not account for the thermal history (i.e. it is independent of temperature and time), which is clearly incorrect as per the findings of Nobili *et al.* [9]. In addition, the Fair & Tsai correlation was obtained using $POCl_3$ diffusion for relatively larger diffusion durations but otherwise similar diffusion temperatures to the ones used in this study. Therefore, an empirical correlation (similar to the one proposed by Fair & Tsai) can only be regarded as a loose approximation that would serve as a guide for the eye rather than a validation method. The reason why empirical forms of the type suggested by Fair & Tsai can be used as a first order check is that such forms can also be inferred from recent studies [103, 104, 105] that have used a $POCl_3$ source for emitter formation in solar cells.

The considerations in the determination of the constants that are used in the determination of C_{Si} are markedly different from those required for the diffusion and precipitation models. The C_{Si} related constants are not only a function of the diffusion temperature (unlike the constants used in the diffusion and precipitation models) but also of the overall gas composition. Moreover, all the constants pertaining to C_{Si} may not have a straightforward (Arrhenius, linear, parabolic, etc) relationship with the processing conditions since the surface concentration is a lumped parameter incorporating the effects of several interfaces.

In the context of this study, it was important to obtain a relationship between the processing conditions and the constants used in the determination of C_{Si} so that the final diffusion model should be able to predict P concentration profiles using only the processing conditions. This

is because it was thought that if a diffusion furnace is designed that is capable of delivering the gas mixture uniformly to an entire wafer batch, rather than a single wafer (as was shown in Figure 15 in section 3.3), then such a diffusion model can be used to control the amount of electrically inactive P. As a result, some important considerations arise for the constants A_k, C_k, D_k and t_0, which determine the instantaneous value of C_{Si} and were introduced in section 4.2. First, for a particular gas flow composition and temperature, the selected constants should allow for good agreement between simulated and experimental profiles when used in combination with the constants of the diffusion and precipitation models.

Secondly, the C_{Si} constants should allow for a reasonable tolerance level such that very good simulation results are still obtained (for the individual gas flow compositions and temperatures) if these constants are varied slightly. This is because when the values of these constants (A_k, C_k, D_k and t_0) are determined for the individual processing conditions, the next step is to extract a relationship between the processing conditions and the constants. Since we do not expect only straightforward relationships between all the constants and the processing conditions, the obtained relationship (polynomial, S-curve and Arrhenius expressions) will not be able to predict the values of A_k, C_k, D_k and t_0 very accurately. Therefore, when modelling the profiles for the individual processing conditions using the obtained relationships and the processing conditions as input parameters, it will still be possible to get very good simulation results, despite the fact the relationships do not accurately predict the values of the constants A_k, C_k, D_k and t_0 that were obtained in the first place.

Lastly, if the relationship between A_k, C_k, D_k or t_0 for a certain processing condition is a polynomial equation, it is important that the polynomial is smooth over the entire range of interest.

Following the identification of the important considerations, I undertook several steps in order to determine the best possible values for the required constants. In the first step,

processes 1-6 (different diffusion durations) were simulated using the empirical surface concentration given in Figure 19 and the effective diffusivity given in section 4.3. For these processes, sufficient experimental data was available for the determination of the constants pertaining to the instantaneous surface concentration. Therefore, the only fitting parameters required are the ones pertaining to the diffusion and precipitation models. These coefficients were chosen such that very good agreement was observed between simulated and total P. In addition, it was also important that the correlation between simulated total and electrically active P would have the same form as that proposed by Fair & Tsai [15]. If any of the above considerations were not met, step 1 was repeated and new coefficients for diffusivity and precipitation were determined.

In the second step, processes 10-15 (different gas compositions) which were conducted at the same diffusion temperature (890 ºC) as were processes 1-6, were simulated using the same diffusion and precipitation related coefficients as were determined in step 1. For all these processes, only the constants used in the empirical determination of the surface concentration were altered such that the final empirical surface concentrations matched the desired experimental surface concentrations. The additional considerations were that the constants chosen for the surface concentrations should result in very good agreement between experimental and simulated profiles and with the correlation between electrically active and total simulated P conforming to the form obtained by Fair & Tsai [15]. If these considerations were not met, both steps 1 and steps 2 were repeated with the aim of obtaining new coefficients for effective diffusivity and precipitation kinetics.

The aim of step three was to determine the constants for the surface concentration, diffusivity and precipitation for temperatures other than 890 ºC. The constants were varied such that the requirements for simulated total and electrically active P, as discussed above for steps 1 and 2, were met. In addition, the constants associated with the precipitation model and the diffusion model must either be independent of the temperature or should have an Arrhenius

dependence on temperature. If all requirements were not met, steps one, two and three were repeated.

After the first two steps, it was found that if the contribution of singly negative vacancies V^- to overall P diffusivity is not negligible then the agreement between simulated and total P profiles is significantly affected for the heavily doped specimens. In addition, with a non-negligible diffusivity contribution of V^-, very good agreement between experimental and simulated total P profiles was not possible for various temperatures, with the model constants following an Arrhenius temperature dependence. The contribution of V^- to dopant diffusivity was therefore ignored and the effective P diffusivity was determined using,

$$D_P^{eff} = D_{(PI)^0} + D_{(PI)^+} + D_{(PV)^-} \tag{4.34}$$

where $D_{(PI)^0}$, $D_{(PI)^-}$ and $D_{(PV)^-}$ are given by equations 4.23, 4.24 and 4.32. As noted in the previous section equation 4.33 can be used for $D_{(PV)^-}$ and the vacancies can be assumed to be in equilibrium throughout the diffusion profile. Such an approximation can, in certain cases, result in very small variations in the simulated profile in region 2. For completeness purposes, the simulations in this study have been carried out using equation 4.32 for $D_{(PV)^-}$.

The final values of the constants for the diffusion and precipitation models are shown in Tables 1 and 2, respectively. Also given in Table 2 are values for the constants used by Dunham for modelling precipitation kinetics. A more detailed discussion of these values is given in chapter 5.

In Figures 24-27, the simulated and experimental P diffusion profiles are shown, as an example to illustrate one of the considerations discussed in this section, namely the best possible value for the constant $D_{(PV)_i^{-,*}}$ to get good agreement between most of the simulated and experimental total P concentration profiles. The constants used in these simulations are the same as those listed in Tables 1 and 2, with the only exception that values used for the

activation energy and pre-exponential factor for the constant $D_{(PV)_i^{-,*}}$ are $4.7eV$ and $1.54 \times 10^2\ cm^2 sec^{-1}$, respectively. These values for the pre-exponential factor and activation energy are such that the resulting simulated and experimental P profiles for process 8 (925 ^oC) in Figure 27 are in very good agreement while for the remaining processes (Figures 24-26) the closest possible agreement between simulated and experimental profiles is obtained. The discrepancy in the simulated and experimental profiles at the *Si* surface arises due to the poor depth resolution of the *SIMS* technique, as was pointed out in section 3.1.2.

On the other hand, using the pre-exponential factor and activation energy listed in Table 1 for the constant $D_{(PV)_i^{-,*}}$, the depth of the simulated P profile for process 8 in region 1 is ~ 4nm less compared to the experimental profile, as is shown in Figure 28. However, the value listed for $D_{(PV)_i^{-,*}}$ in Table 1 gives very good simulation accuracies for most of the other processes (that are shown in Figure 30-33 and discussed in chapter 5) while the modified value for $D_{(PV)_i^{-,*}}$ gives relatively poor results for these remaining processes that are shown in Figure 24-27. This distortion in the simulation results arises because of the requirement of obtaining an Arrhenius dependence of $D_{(PV)_i^{-,*}}$ on temperature.

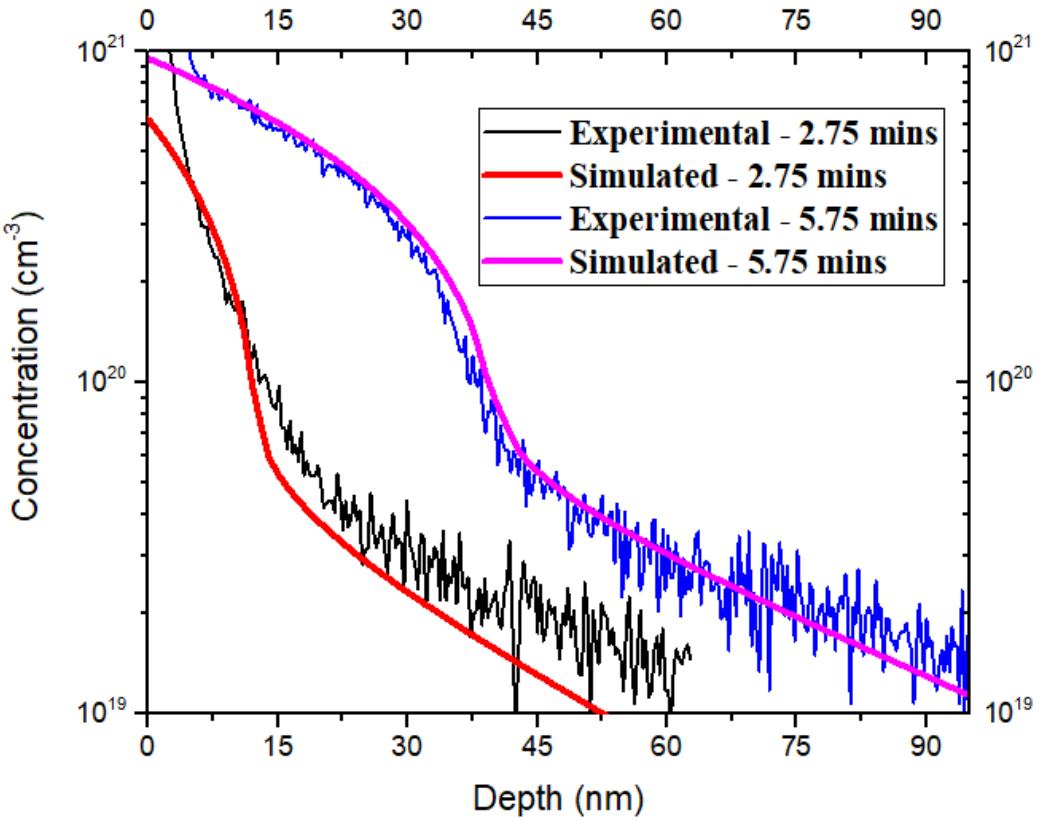


Figure 24: Simulated (red) and experimental (black) P profiles for process 3 (2.75 minutes long diffusion) and simulated (pink) and experimental (blue) P profiles for process 4 (5.75 minutes long diffusion). Both processes (Process 3 and Process 4) had the same diffusion temperature (890 °C) and gas composition ($POCl_3$ = 375 SCCM, O_2 = 500 SCCM, N_2 = 13.125 SLPM). The simulated profiles used a modified value for the vacancy diffusivity ($D_{(PV)_i^{-,*}} = 1.54 \times 10^2 exp(-4.7eV/KT) cm^2 s^{-1}$) instead of the actual value ($D_{(PV)_i^{-,*}} = 1.22 \times 10^2 exp(-4.69eV/KT) cm^2 s^{-1}$) that has been used in simulating P profiles in this work.

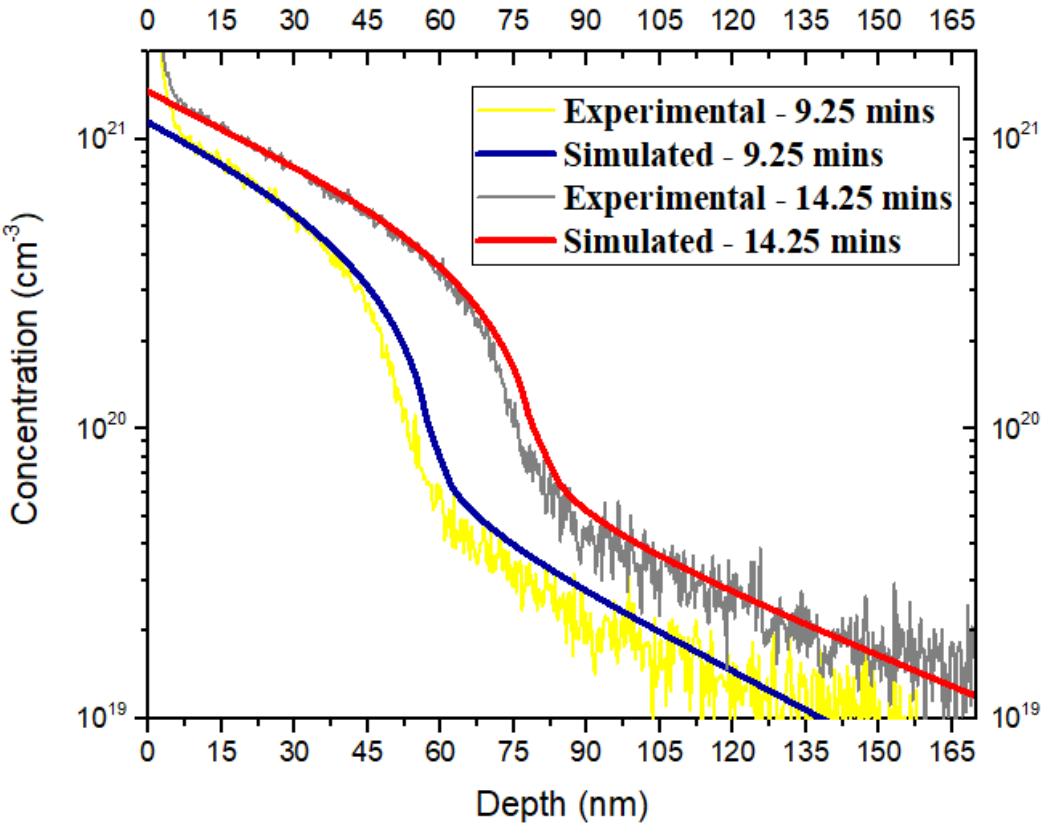


Figure 25: Simulated (blue) and experimental (yellow) P profiles for process 5 (9.25 minutes long diffusion) and simulated (red) and experimental (grey) P profiles for process 6 (14.25 minutes long diffusion). Both processes (Process 5 and Process 6) had the same diffusion temperature (890 °C) and gas composition ($POCl_3$ = 375 SCCM, O_2 = 500 SCCM, N_2 = 13.125 SLPM). The simulated profiles used a modified value for the vacancy diffusivity ($D_{(PV)_i^{-,*}} = 1.54 \times 10^2 exp(-4.7eV/KT) cm^2 s^{-1}$) instead of the actual value ($D_{(PV)_i^{-,*}} = 1.22 \times 10^2 exp(-4.69eV/KT) cm^2 s^{-1}$) that has been used in simulating P profiles in this work.

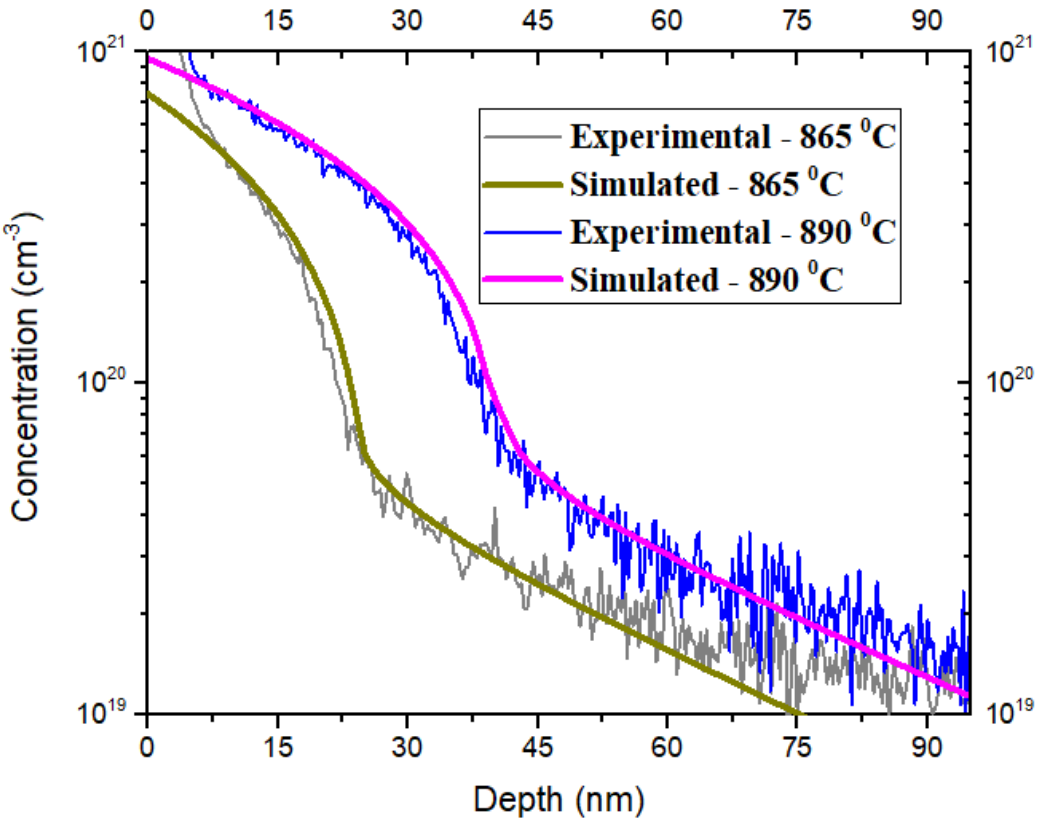


Figure 26: Simulated (green) and experimental (grey) P profiles for process 7 (diffusion at 865 °C) and simulated (pink) and experimental (blue) P profiles for process 4 (diffusion at 865 °C). Both processes (Process 4 and Process 7) had the same diffusion duration (5.75 minutes) and gas composition ($POCl_3$ = 375 SCCM, O_2 = 500 SCCM, N_2 = 13.125 SLPM). The simulated profiles used a modified value for the vacancy diffusivity ($D_{(PV)_i^{-,*}} = 1.54 \times 10^2 exp(-4.7eV/KT) cm^2 s^{-1}$) instead of the actual value ($D_{(PV)_i^{-,*}} = 1.22 \times 10^2 exp(-4.69eV/KT) cm^2 s^{-1}$) that has been used in simulating P profiles in this work.

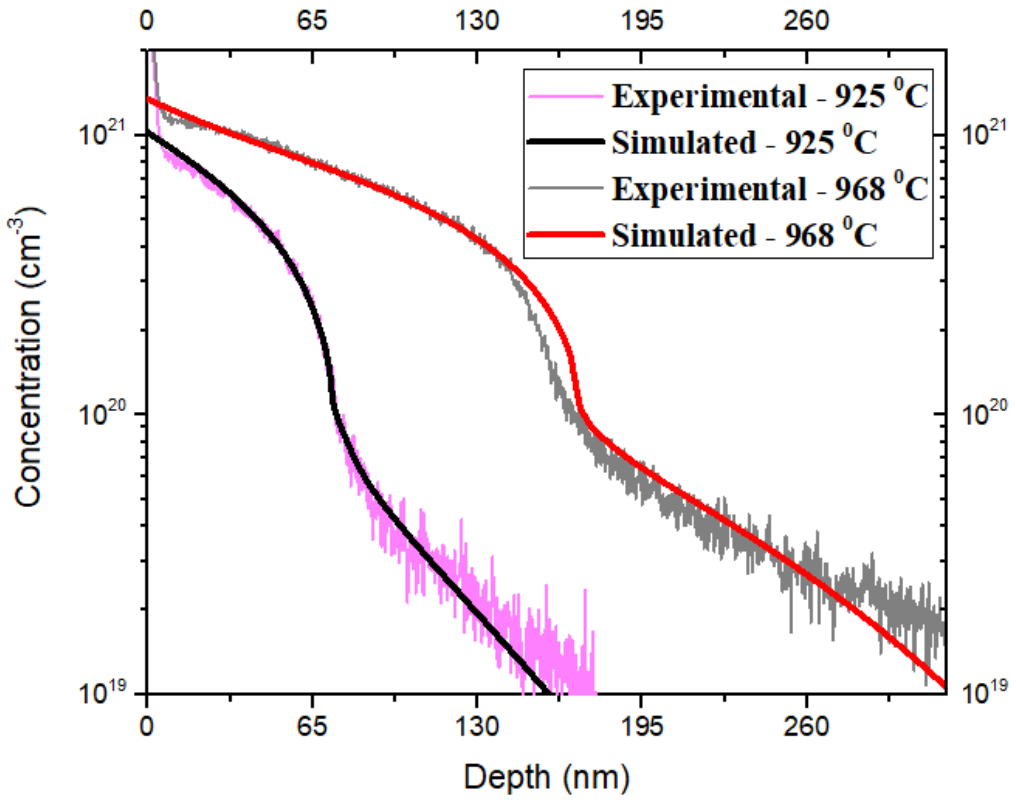


Figure 27: Simulated (black) and experimental (pink) P profiles for process 8 (diffusion at 925 °C) and simulated (red) and experimental (grey) P profiles for process 9 (diffusion at 968 °C). Both processes (Process 8 and Process 9) had the same diffusion duration (5.75 minutes) and gas composition ($POCl_3$ = 375 SCCM, O_2 = 500 SCCM, N_2 = 13.125 SLPM). The simulated profiles used a modified value for the vacancy diffusivity ($D_{(PV)_i^{-,*}} = 1.54 \times 10^2 exp(-4.7eV/KT) cm^2 s^{-1}$) instead of the actual value ($D_{(PV)_i^{-,*}} = 1.22 \times 10^2 exp(-4.69eV/KT) cm^2 s^{-1}$) that has been used in simulating P profiles in this work.

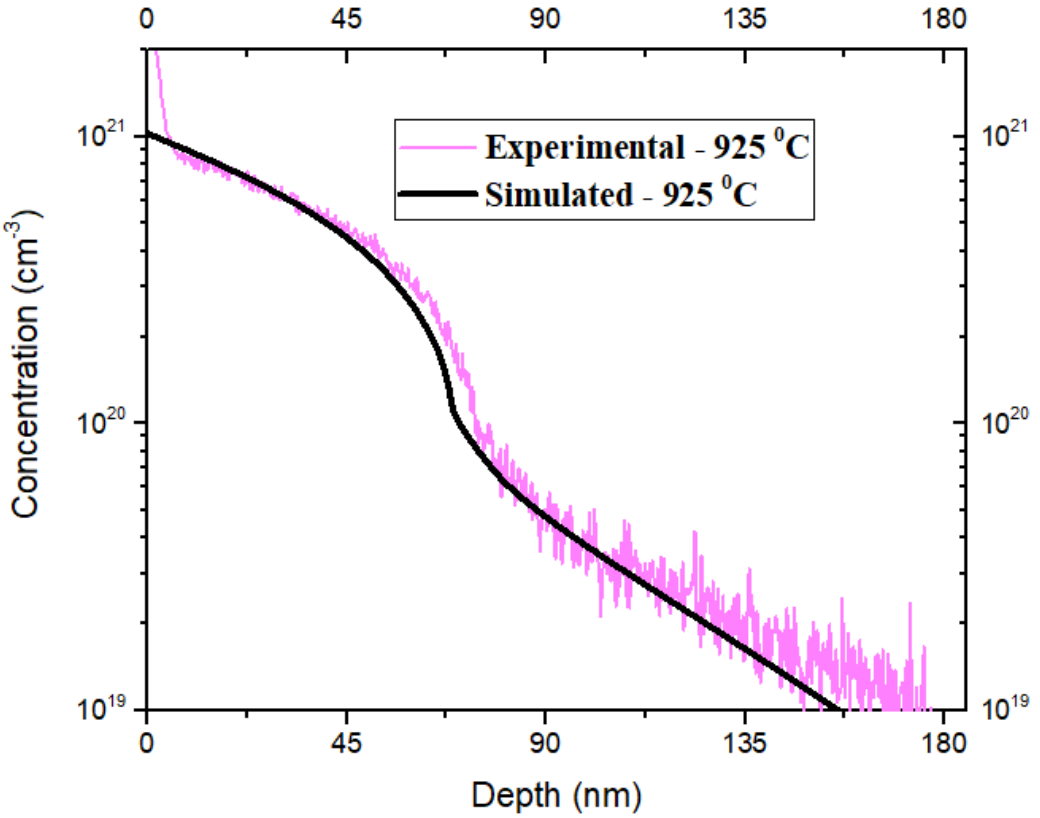


Figure 28: Simulated (black) and experimental (pink) *P* profiles for process 8 (5.75 mins) using the constants determined in this study and listed in Table 1, i.e., using the actual value for $D_{(PV)_i^{-,*}}$ (see text for explanation).

.

An alternative approach is to use the value for $D_{(PV)_i^{-,*}}$ as listed in Table 1 and only change the value of the parameter t_0 that is used in the determination of the phosphorus concentration at the silicon surface (C_{Si}) as was discussed in section 4.2. As shown in Figure 29, reducing the value of t_0 by 30 seconds from its suggested value in this study (listed in Appendix B), allows for very good agreement between simulated and experimental P profiles in region 1 for process 8. Since the parameter t_0 denotes the initial duration during which the surface concentration rises slowly, a reduction in the value of t_0 means that there is more time for the diffusion to proceed while C_{Si} is at a higher value. The overall effect is an increased diffusion depth in the simulated profile. However, in this particular case such an adjustment in the value of the parameter t_0, required a polynomial equation to explain the dependence of t_0 on temperature (that was not smooth over the entire temperature range 865 – 968 ºC) instead of an Arrhenius equation that has been used in this study.

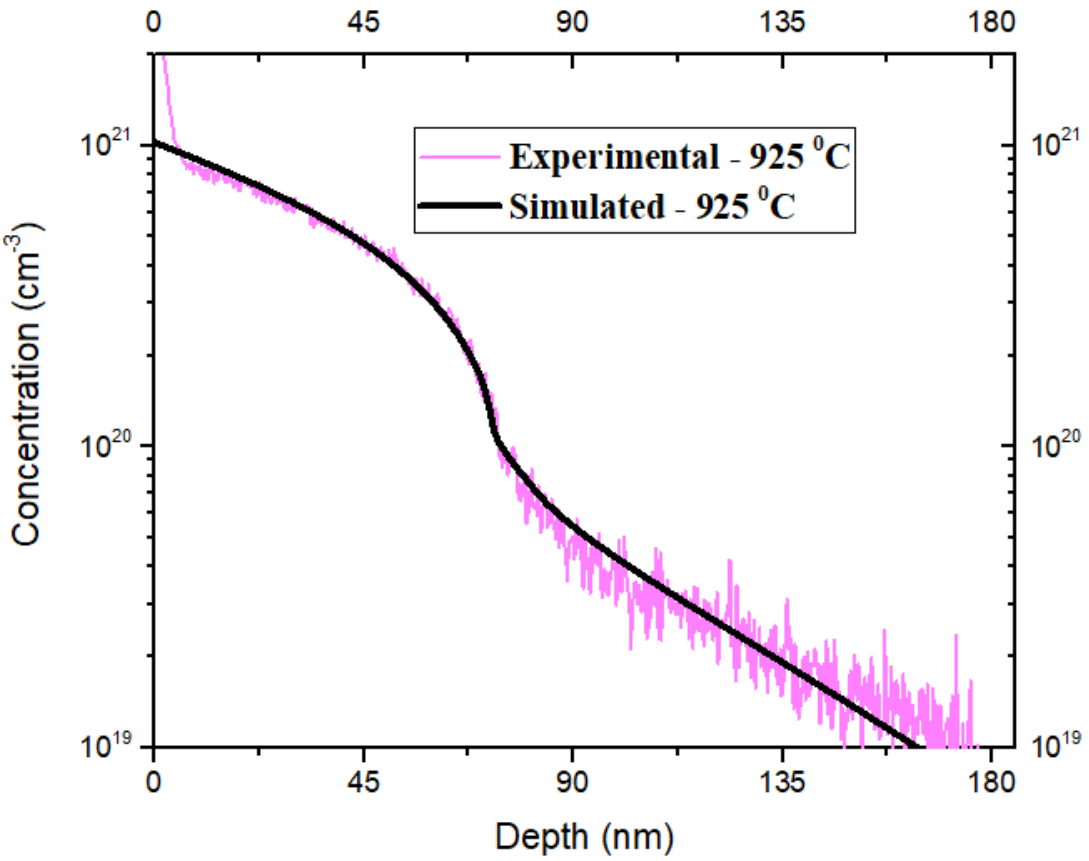


Figure 29: Simulated and experimental *P* profiles for process 8 (5.75 mins) using the constants listed in Table 1 and the modified of t_0 (see text for explanation).

Coefficient	Activation Energy (eV)	Pre-exponential factor	Definition of Coefficients
$\boldsymbol{D_{(PI)_i^{+,*}}}$	4.26	933 $cm^2 sec^{-1}$	Diffusivity of P due to I^0 under equilibrium and intrinsic conditions
$\boldsymbol{D_{(PI)_i^{0,*}}}$	2.62	1.48×10^{-5} $cm^2 sec^{-1}$	Diffusivity of P due to I^- under equilibrium and intrinsic conditions
$\boldsymbol{D_{(PV)_i^{-,*}}}$	4.69	1.22×10^{2} $cm^2 sec^{-1}$	Diffusivity of P due to V^{--} under equilibrium and intrinsic conditions
$\boldsymbol{C_{Th}}$	1.59	7.78×10^{26} cm^{-3}	Threshold concentration of C_P^+ above which vacancy percolation is dominant
$\boldsymbol{S_0}$	-2.79	1.53×10^{-10}	Supersaturation factor of I^0 due to the kick

			out reaction in the absence of external influences
S_1	3.51	1.52×10^{16}	Supersaturation factor of I^- due to the kick out reaction in the absence of external influences
n_{k1}	0.19	$6.35 \times 10^{20}\ cm^{-3}$	Electron concentration at which the dissociation rate of $(PI)^+$ equals the rate of excess I^0 formation
n_{k2}	-0.1	$6.66 \times 10^{19}\ cm^{-3}$	Electron concentration at which the dissociation rate of $(PI)^0$ equals the rate of excess I^- formation
m	0	1	Number of phosphorus atoms with which a vacancy interacts while percolating through the material

Table 1. List of parameters used in the determination of the effective P diffusion coefficient.

Parameter	This work	Dunham [64]
$a_1(eV)$	0.69	0.69
m_1	$^2/_3$	$^2/_3$
$a_2(eV)$	-1.4	-1.54
m_2	$^1/_3$	$^1/_3$
$a_3(eV)$	$-2.01 \times 10^4 \exp(-1.17/KT)$	-0.49
m_3	-1	-1
$C_{SS}(cm^{-3})$	$1.33 \times 10^{22} \exp(-0.37/KT)$	$8.33 \times 10^{21} \exp(-0.328/KT)$

Table 2. List of constants used in modelling dopant precipitation by Dunham [64] and in this work.

4.5 Summary

In this chapter, a comprehensive model of P diffusion has been explained, which is consistent with the general understanding of P diffusion in Si. The mathematical approach outlined in this chapter relies on an approximate solution for the interstitial concentration profile in the diffused emitter, which allows for a straightforward solution to the continuity equations. Fundamental to the model are the assumptions of the kick out reactions and the conversion of phosphorus interstitial *PI* pairs (due to their dissociation) into phosphorus vacancy pairs at high electron concentrations. While the kick out reactions have previously been posited as the most likely cause of the interstitial supersaturation, plausible explanations have been provided in this work for the dissociation reactions of *PI* pairs.

Also discussed in this chapter are the simulation methodology and the determination of the dopant concentration at the *Si* surface. The finite difference method has been employed to compute the solute flux diffusing into Si and the growing precipitates. Moreover, since the diffusion model requires several constants, an iterative approach has been used to determine the best values for these constants.

CHAPTER 5
RESULTS AND DISCUSSION

In this chapter, I discuss simulation results that were obtained using the diffusion model discussed in chapter 4. The constants used in these simulations are listed in Tables 1 and 2 in chapter 4 and in Appendix B. These constants have been used to simulate all diffusion profiles shown in this chapter. In section 5.1, the simulation results are shown and the effective P diffusivity in the three regions is discussed. In section 5.2, the diffusion and precipitation related constants listed in Tables 1 and 2 (section 4.4) are compared with those reported in previous studies. A discussion on the electrically active P profiles is given in section 5.3.

5.1 Results

Simulated total P profiles, which were obtained using the methodology outlined in section 4.1 and the effective diffusivity given by equation 4.34, for processes 3-9 are shown in Figures 30-33. In Figures 30 and 31, the simulated and experimental profiles are shown for processes 3-6, where only the diffusion duration was altered. Comparison of the simulated and experimental profiles for various diffusion temperatures are shown in Figure 32 and 33. It can be seen that very good agreement for all profiles is obtained. As noted previously in section 4.4 and discussed in section 3.1.2, the discrepancy in the simulated and experimental P profiles at the *Si* surface arises due to the poor depth resolution of *SIMS* for the relatively narrow pile up layer.

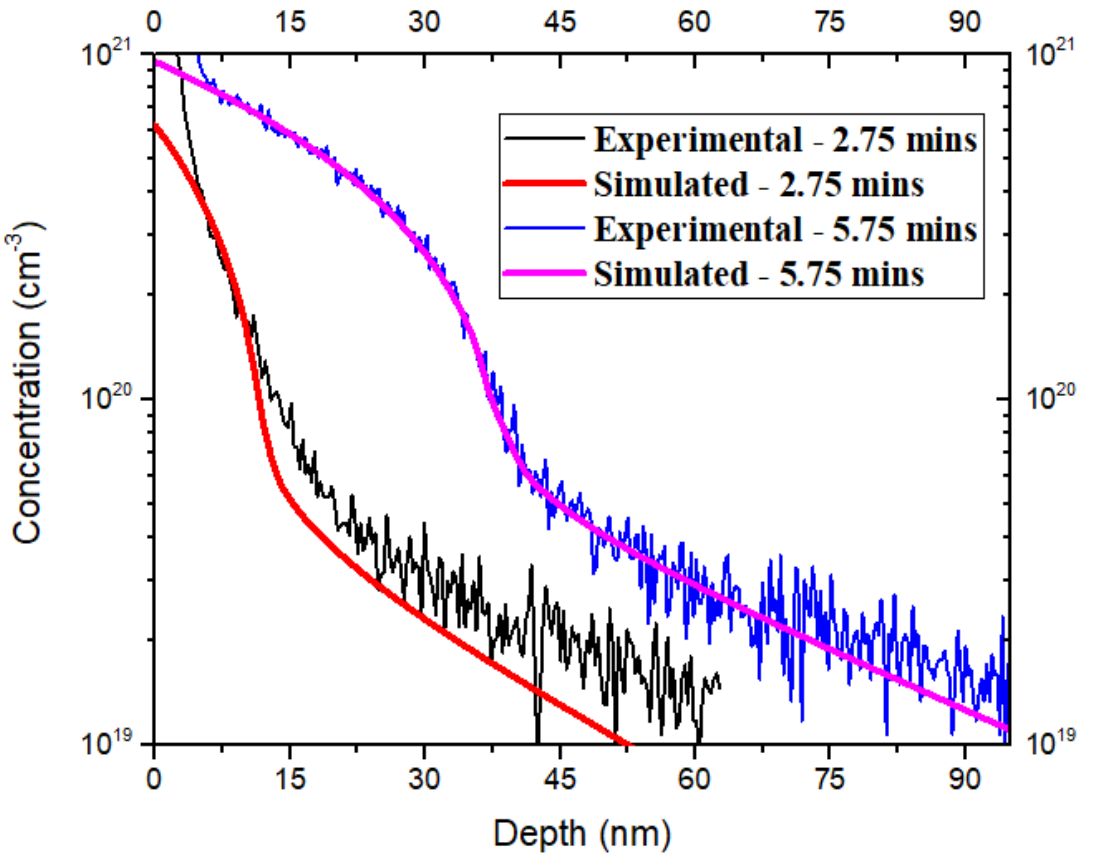


Figure 30: Simulated and experimental *P* profiles for process 3 and process 4 (at 890 °C).

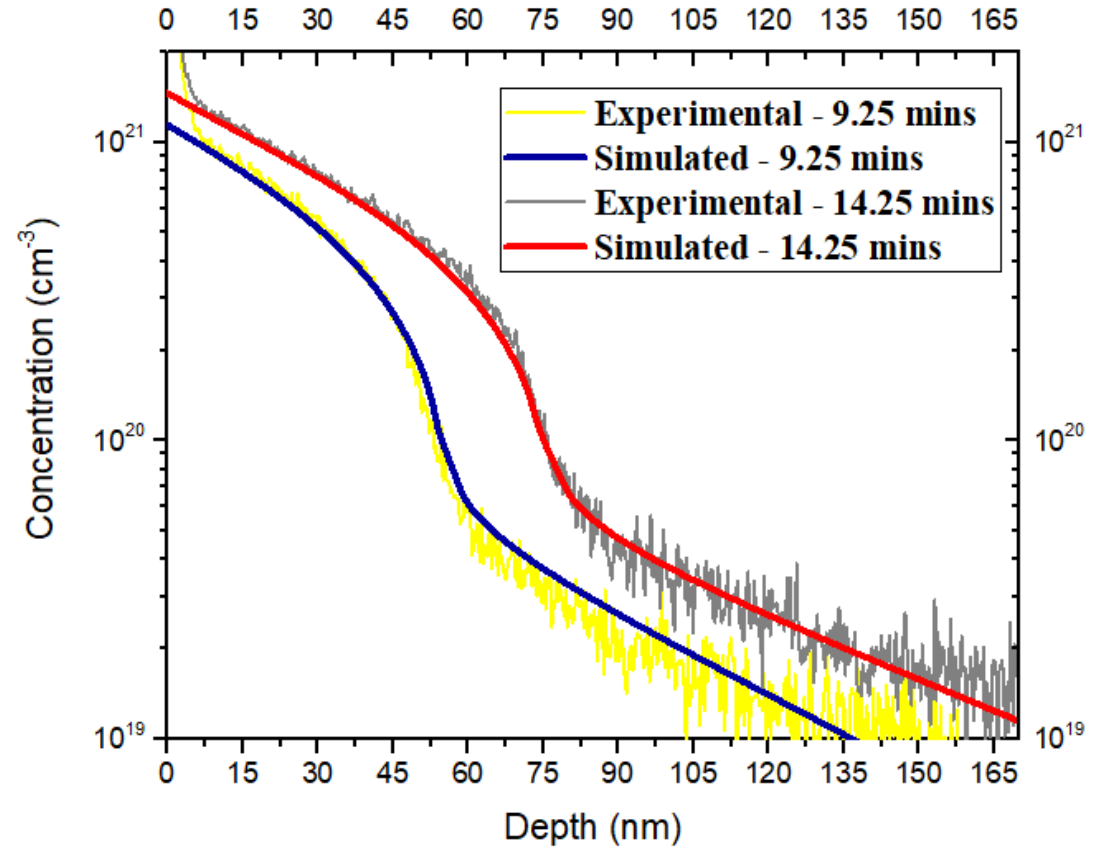


Figure 31: Simulated and experimental *P* profiles for process 5 and process 6 (at 890 °C).

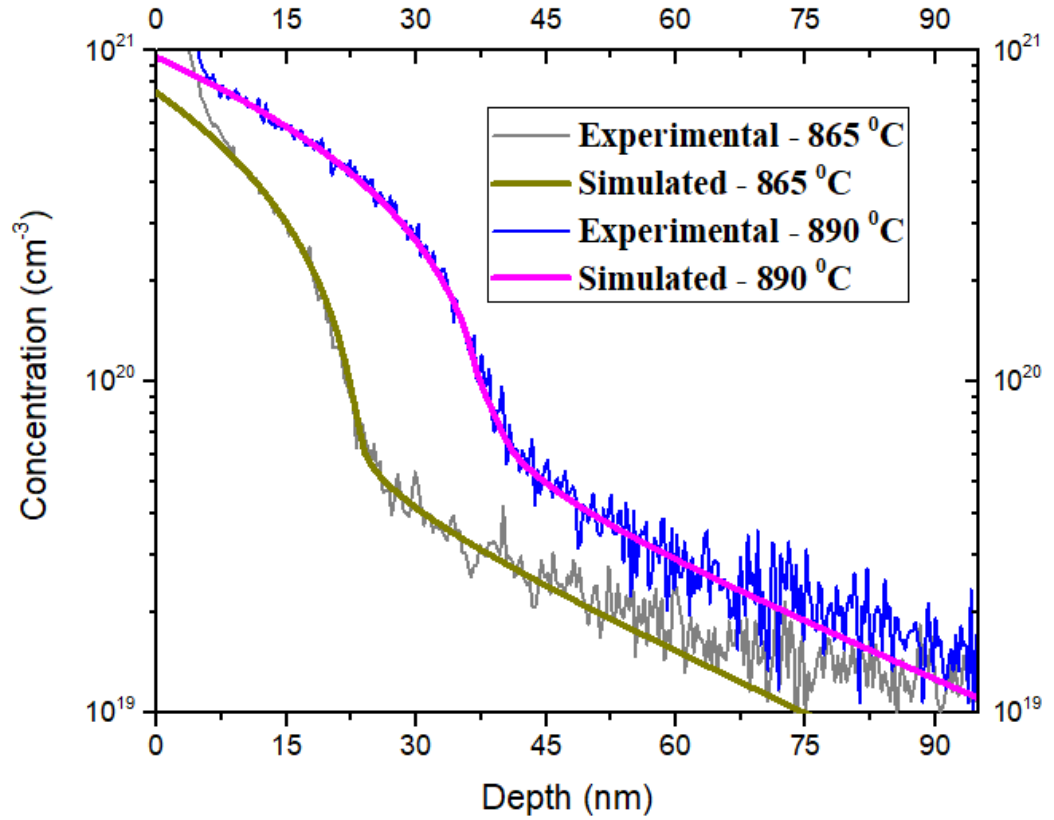


Figure 32: Simulated and experimental *P* profiles for process 4 and process 7 (5.75 mins).

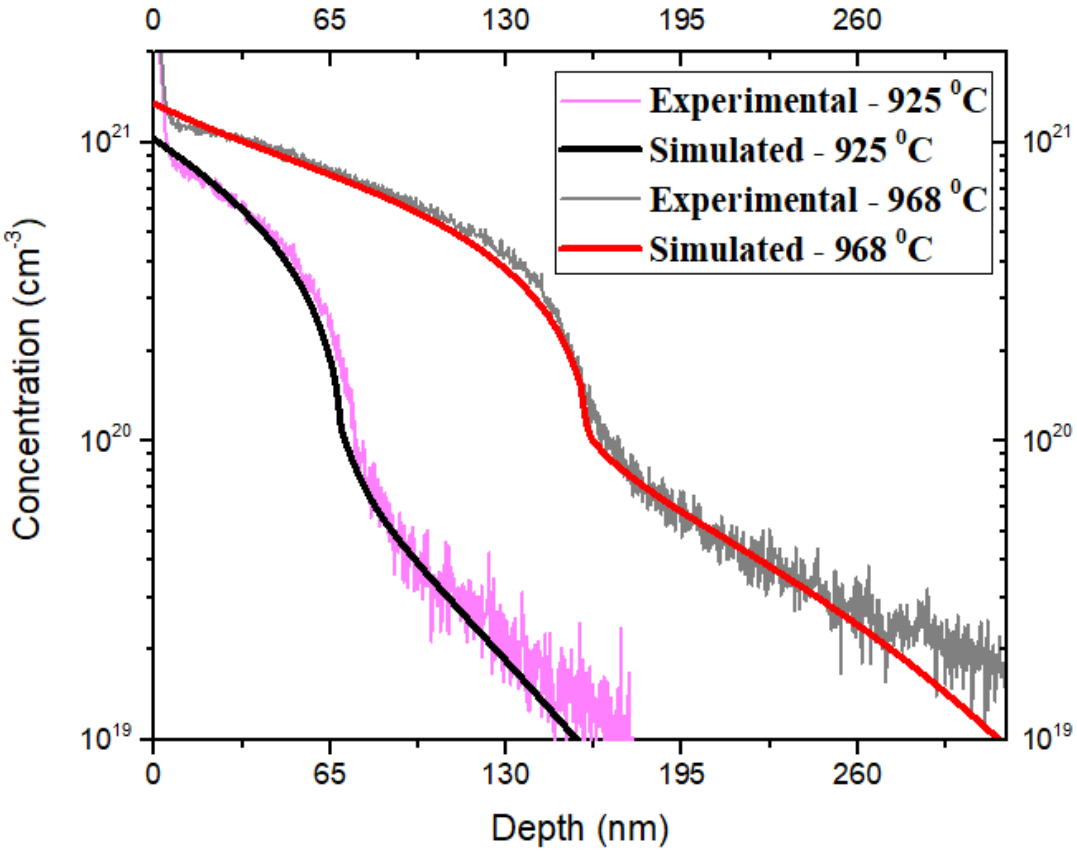


Figure 33: Simulated and experimental *P* profiles for process 8 and process 9 (5.75 mins).

Simulation results for processes 10, 5 and 11 where only the $POCl_3$ partial pressure was varied (0.05%, 0.1%, 0.21%) are shown in Figure 34.

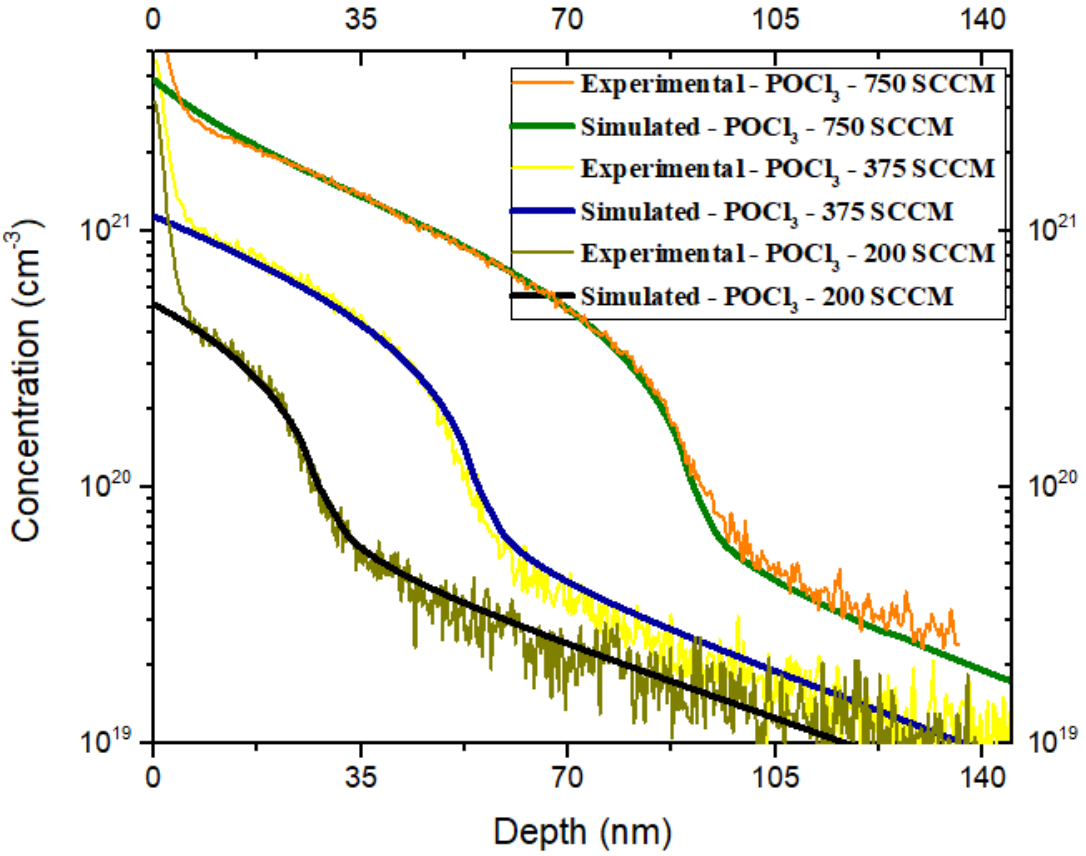


Figure 34: Experimental and simulated diffusion profiles for processes 5 & 10 with different *$POCl_3$* contents in the gas phase. (890 ºC, 9.25 mins).

The N_2 flow (and total flow) in process 13 was reduced to 8 SLPM. The corresponding increase in the $POCl_3$ partial pressure therefore results in heavy doping of the substrate. In Figure 35, the profile of process 13 is shown in comparison with profiles of processes 12 (the heaviest doped specimen reported in this study) and 5 (moderate $POCl_3$ flow of 375 SCCM).

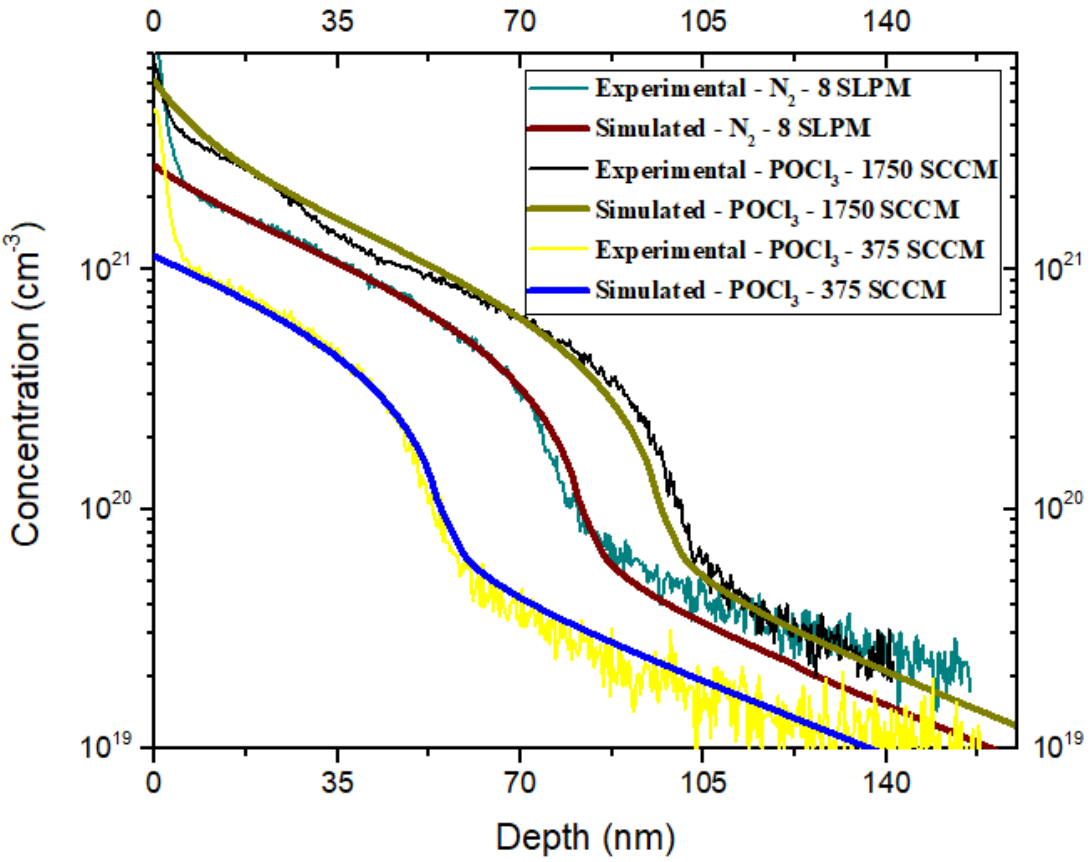


Figure 35: Experimental and simulated diffusion profiles for processes (5, 12 & 13) with same diffusion temperature (890 ºC) and duration (9.25 mins) but different gas flow composition (appendix A).

Results for processes 5, 14 and 15 where only the oxygen partial pressure was varied are shown in Figures 36 and 37. Since process 14 and process 15 result in similar depths, they are for clarity purpose compared separately with the *P* profile of process 5 in Figure 36 and Figure 37, respectively. The relatively higher doping levels that are achieved in these cases (compared to process 5 – O_2 500 SCCM) are perhaps due to the complicated mass transfers taking place inside the *PSG* and its interfaces with gas and substrate.

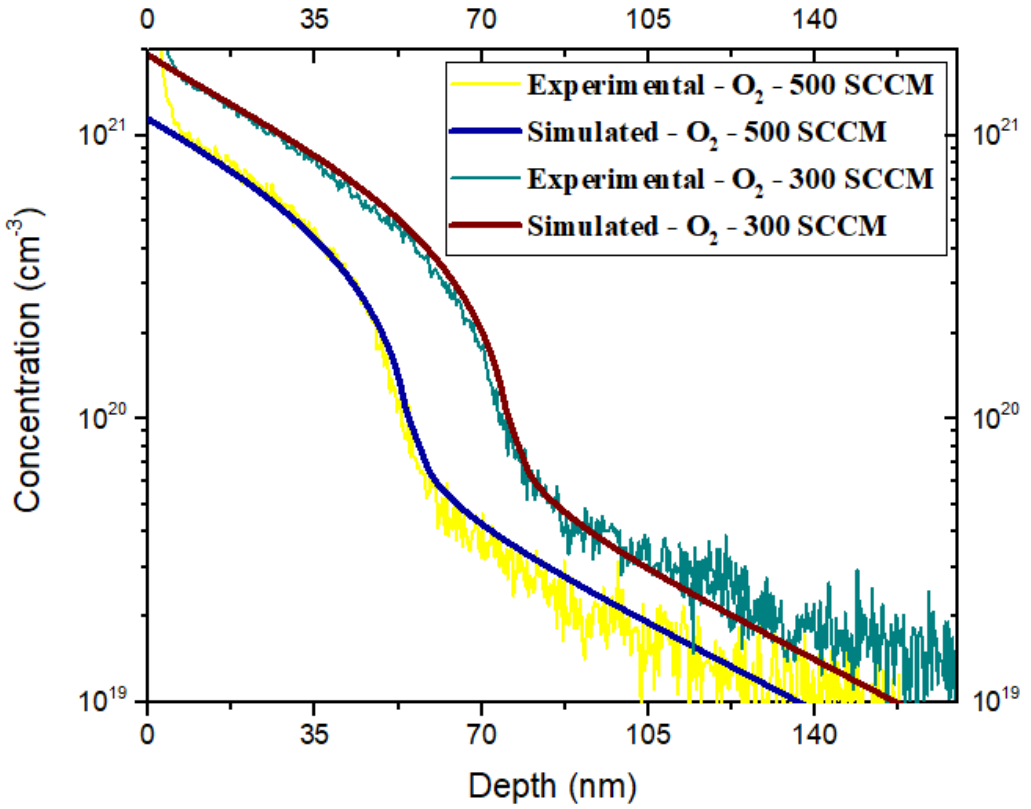


Figure 36: Experimental and simulated diffusion profiles for processes with different O_2 partial pressure in the gas phase.

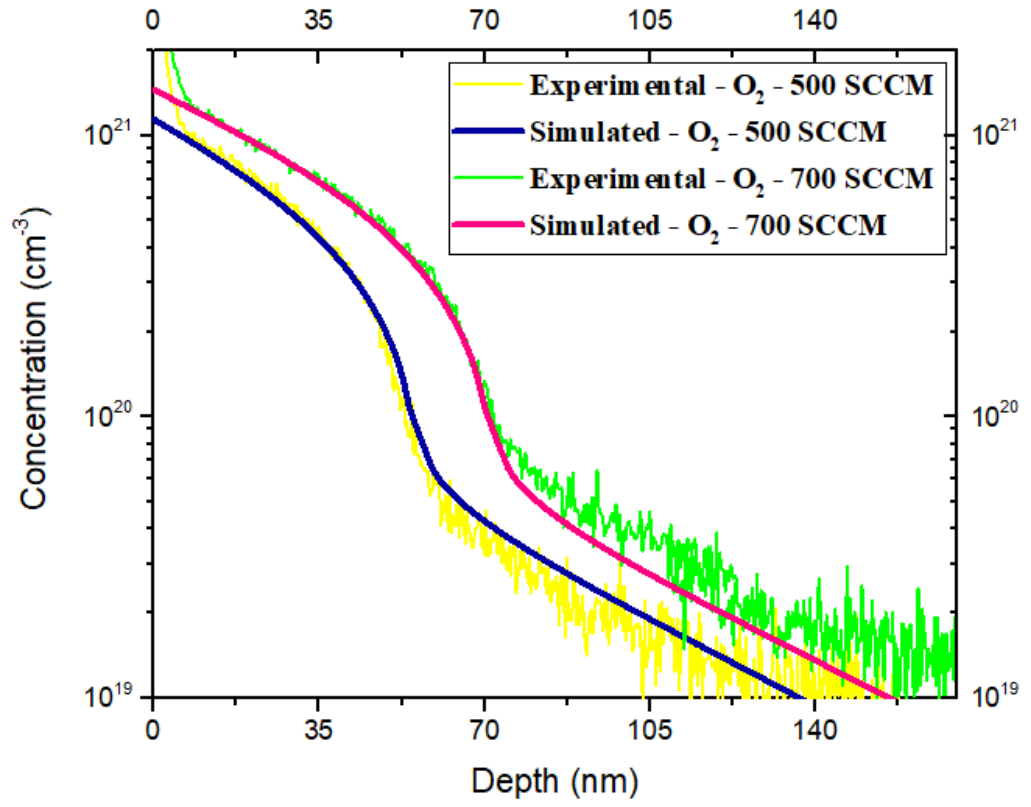


Figure 37: Experimental and simulated diffusion profiles for processes with different O_2 partial pressure in the gas phase.

In Figure 38, the simulated electrical profile (left y-axis) along with its corresponding vacancy and interstitial diffusivities (right y-axis) are shown. The concentration profile and the diffusivities as a function of depth were obtained at the end of a simulation scheme. The interstitial diffusivity, which is given by the sum of the contributions from the neutral ($D_{(PI)^+}$) and the negatively charged ($D_{(PI)^0}$) interstitials to P diffusivity, is not insignificant in region 1, however, compared with the vacancy diffusivity, the interstitial diffusivity in region 1 is mall and does not change significantly with the doping level. As per this study, the contribution of vacancies to P diffusivity in region 1 is dominant in comparison to the contribution of interstitials to P diffusivity. Due to the percolation effect, the vacancy diffusivity drops rapidly at the percolation threshold, somewhere at the intersection of regions 1 and 2. The vacancy diffusivity quickly becomes negligible in region 2 while the interstitial diffusivities begin to rise in a complex manner.

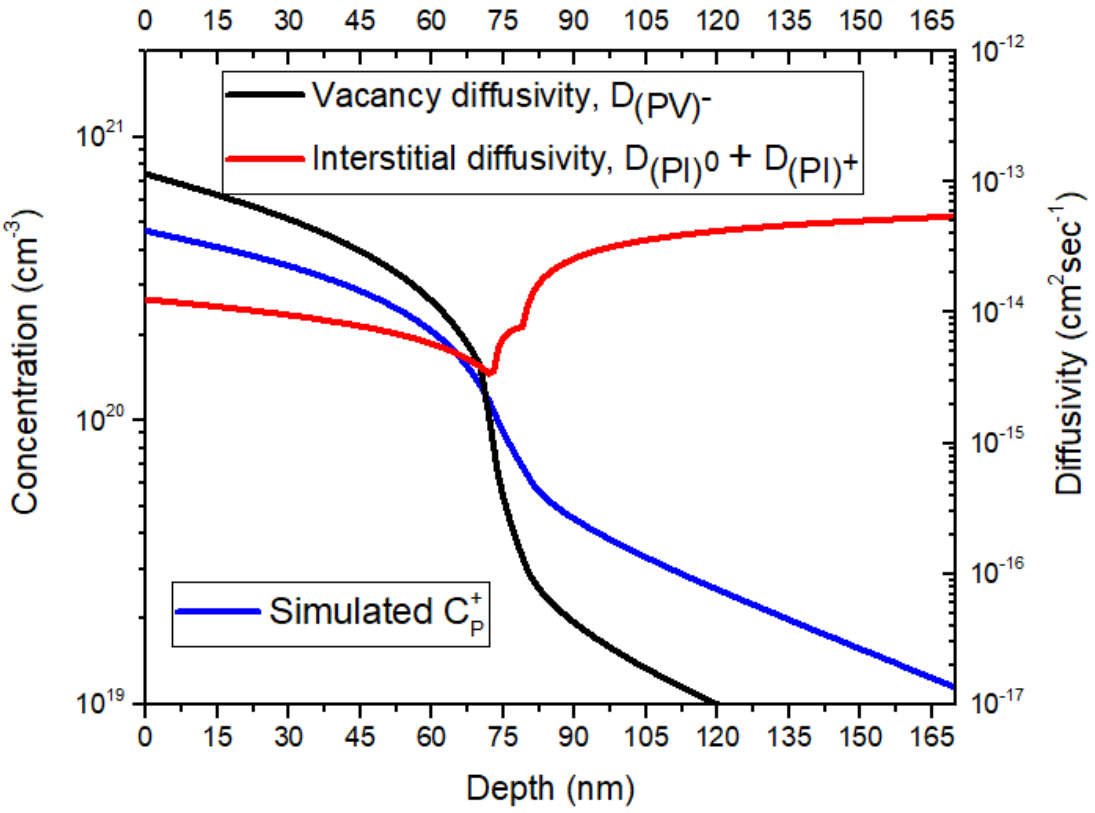


Figure 38: Simulated electrical profile (blue) for process 6 (890 °C, 14.25 mins). The vacancy diffusivity (black) drops rapidly at the intersection of regions 1 and 2. Interstitial diffusivity (red) dominates P diffusion in regions 2 and 3. The vacancy and interstitial diffusivities shown are those pertaining at the end of the simulation.

In Figure 39, the two interstitial diffusivity components are shown along with the same electrically active P profile. P diffusivity due to neutral interstitials paired with a positively charged P ion, $D_{(PI)^+}$, is negligible in regions 1 and 2 as opposed to in region 3 where it is dominant. The value selected for the neutral interstitial diffusivity under intrinsic and equilibrium conditions ($D_{(PI)_i^{+,*}}$) is small. For a temperature of 890 ºC (the temperature of the simulated electrical profile in Figure 39), the supersaturation factor in the bulk (i.e. the maximum value of the supersaturation factor) is approximately 70. Due to the very large value of S_0, $D_{(PI)^+}$ dominates overall P diffusivity in region 3. However, equation 4.19a suggests that with increasing electron concentrations the effective supersaturation of neutral interstitials in region 3 slowly decreases from its maximum value in the bulk, and that neutral interstitial concentrations will decrease rapidly for concentrations approaching the kink concentration. In regions 1 and 2 the neutral interstitial concentration is in equilibrium (due to the rapid reaction rate of reaction R4.1) resulting in a very low value of $D_{(PI)^+}$. In addition, since the neutral interstitial concentration is independent of the Fermi level, the value of $D_{(PI)^+}$ is a constant in regions 1 and 2, i.e. $D_{(PI)^+} = D_{(PI)_i^{+,*}}$.

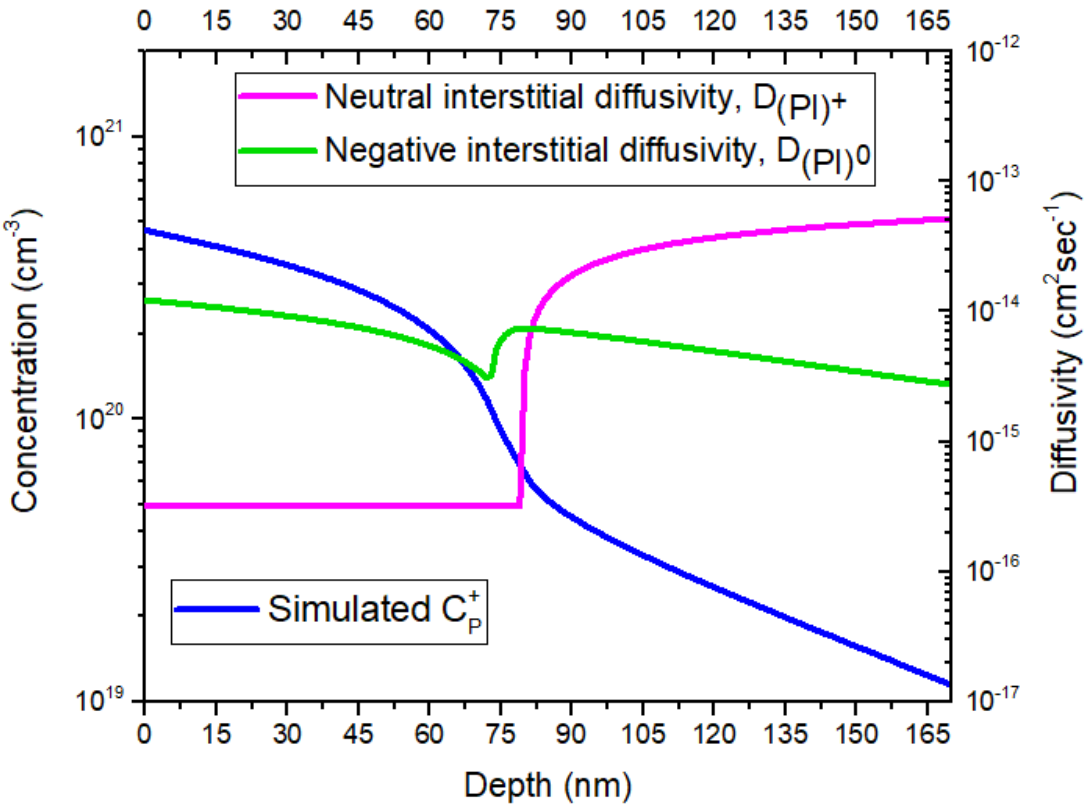


Figure 39: Simulated electrical profile (blue) for process 6 (890 °C, 14.25 mins). The corresponding diffusivities of P via pairing with the neutral and negatively charged interstitials are shown by the pink and green curves, respectively. These diffusivities were obtained at the end of a simulation scheme.

The contribution of negative interstitials to overall P diffusivity, $D_{(PI)^0}$, is not negligible in regions 1 and 3 but is certainly not the dominant mechanism in these regions. Negative interstitials acquire equilibrium in region 1 and their effective supersaturation factor decreases rapidly in region 2. The value of the maximum supersaturation factor of negative interstitials in the bulk at 890 °C (S_1~9.4) is small compared to S_1. Moreover, the value of the neutral interstitial diffusivity under intrinsic and equilibrium conditions ($D_{(PI)_i^{0,*}}$) is also small compared to that of $D_{(PI)_i^{+,*}}$. This means that relative to $D_{(PI)^+}$, the contribution of $D_{(PI)^0}$ to overall P diffusivity remains small for the low doping levels in region 3. The concentration of I^-, C_{I^-}, in region 3 is affected by changes in the Fermi level in two different ways. First, C_{I^-} increases with the Fermi level according to n/n_i due to changes in the local equilibrium. Secondly, C_{I^-} decreases with the Fermi level due to an increased reaction rate of reaction R4.2. The overall effect is that the value of $D_{(PI)^0}$ increases with doping in region 3

and, despite experiencing a sudden dip, dominates diffusion in the rapidly falling region of the P profile, region 2.

5.2 Comparison of constants with values from previous studies

In this section, the values of the model constants listed in Tables 1 and 2 (section 4.4) with their estimated values reported in the literature are compared. In subsection 5.2.1, the model constants in table 1 are discussed with reference either to their experimental (if available) or theoretical estimates. Where a direct comparison was not possible, the model constants in Table 1 were compared with similar (or equivalent) constants in the literature. Comparison for the model constants in Table 2 with that reported by Dunham is given in section 5.2.2.

5.2.1 Constants for the effective diffusivity of P

The overall diffusion coefficient of *P* under intrinsic conditions is governed by interstitial diffusivity [56]. It can be approximated by,

$$D_{(PI)_i^*} \sim D_{(PI)_i^{0,*}} + D_{(PI)_i^{+,*}} \tag{5.1}$$

where the contribution from vacancies and positively charged interstitials has been ignored. In Figure 40 comparison between $D_{(PI)_i^{0,*}} + D_{(PI)_i^{+,*}}$ (as determined in this work) and literature value [15] of $D_{(PI)_i^*}$ is shown.

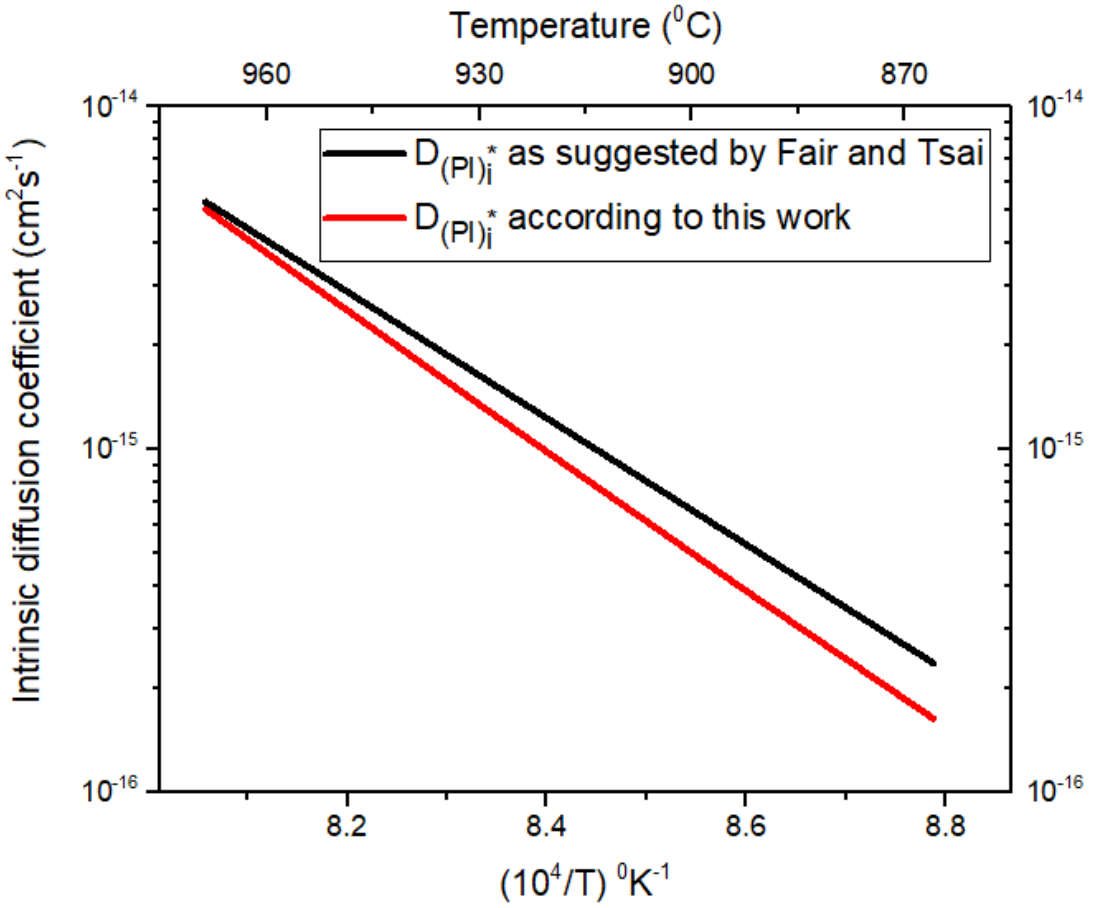


Figure 40: Expected intrinsic diffusivity of *P* as determined via simulations (red) and the intrinsic diffusivity (black) of *P* given by Fair & Tsai [15]. (See text for explanation).

Morehead and Lever [58] have reported an approximate value of 70 and 1000 for the supersaturation factor at 900 ºC and 700 ºC, respectively. The supersaturation factor of neutral interstitials, S_0, listed in Table 1 is greater by a factor of 2.12 compared to the values given in [58]. However, it must be noted that the Morehead and Lever used a crude approximation for the supersaturation factor. Their approximation assumes a constant diffusivity in the tail region which is enhanced over the intrinsic diffusivity by an amount corresponding to the interstitial supersaturation, $S = D_{tail}/D_{(PI)_i^*}$, where $D_{(PI)_i^*}$ is taken from [15] and D_{tail} (diffusivity of P in region 3) is determined using an error function approximation from the tail region of experimental profiles. Such an approach means that the authors do not consider the profile shape in the tail region but only the overall depth of the tail region. Moreover, the value of $D_{(PI)_i^*}$ used by Morehead and Lever is 1.65 times the

value of $D_{(PI)_i^{+,*}}$ used in this work, and can somewhat account for the relatively small supersaturation factor reported by the authors.

Diffusion models that consider diffusion via the doubly negative vacancy [15, 46, 47, 60, 61] as the dominant diffusion mechanism have always ignored the percolation effect. On the other hand, the Dunham vacancy percolation model [32], unlike the Dunham diffusion model [46], considers P diffusion to be mediated primarily by singly negative vacancies V^- at high doping levels. The probable reason for this drastic departure from conventional models [15, 46, 47, 60, 61] (that consider diffusion via V^{--}) might be that the percolation study of Dunham [32] is mainly aimed at the diffusion behaviour of arsenic, which diffuses via V^-. The goal in Dunham's percolation model is to show that the diffusion coefficients of donors scale with higher powers $(n/n_i)^m$ with $m > 2$ of the electron concentration at very high doping levels and that this behaviour can be explained from first principles. Dunham *et al.* [32] had suggested a value of four for m for most donors, while the suggested value for P was close to five. Later, however, in his review on dopant diffusion modelling the author [63] reported a value between three and four for P. The value of m listed in Table 1 is one, however, when the doubly negative vacancy is considered as the percolating specie and the value of m is one then the overall diffusivity will scale with a cubic dependence on the electron concentration $(n/n_i)^3$ for the very high doping levels. This is effectively the same outcome as using a value of three for m and considering diffusion to be mediated via V^-.

From published data of arsenic (at 915 ºC and 1050 ºC) and phosphorus (at 1050 ºC), Dunham *et al.* [32] infer the vacancy percolation threshold concentration to be above $C^{Th} = 2 \times 10^{20} cm^{-3}$ at diffusion temperatures. Mathiot and Pfister [33], on the other hand, suggested a theoretical value of $3 \times 10^{20} cm^{-3}$ for the vacancy percolation threshold concentration. The best possible value for C^{Th} that allowed for very good agreement between simulated and total P profiles in this work was found to be a function of temperature. The pre-exponential factor and activation energy were $7.78 \times 10^{26} cm^{-3}$ and $1.59\, eV$,

respectively. The resulting value of C^{Th} in this study varies between $7 \times 10^{19}\ and\ 2.7 \times 10^{20} cm^{-3}$ for the temperature range 865-968 ºC.

5.2.2 Constants for the P precipitation kinetics

In section 2.5.2.3 the discrepancy between the solubility limit and the maximum electrically active P concentration, as reported by Solmi *et al.* [66], was discussed. Prior to the work of Solmi *et al.* in 1996 [66], the maximum electrically active P level was taken as the solubility limit. Since the work of Solmi *et al.* appeared after the Dunham precipitation model [64], Dunham used the available solubility values of Massetti *et al.* [10], which were obtained after prolonged $POCl_3$ diffusion processes wherein the concentration level of the plateau was taken as the solubility limit. Prior to Dunham's precipitation model, Nobili *et al.* [9] had pointed out that such a determination might be close to the actual solubility limit since the system after prolonged annealing times would have acquired equilibrium.

According to the findings of Nobili *et al.* [9] P does not form large precipitates and most of the inactive P is present in the form of small disc and dot like precipitates that are perfectly coherent with the *Si* matrix. Under conventional diffusion processes, large rod-like orthorhombic *SiP* precipitates have been observed only at the *PSG/Si* interface [71], where they lie parallel to the interface. One of the reasons for such structures to exist at the *PSG/Si* interface is that a high density of *Si* self-interstitials (generated due to oxidation) is readily available at the interface, which can assist the growth of large *SiP* structures. In the Si away from the moving *PSG/Si* interface where the Si self-interstitial concentration is low compared to that at the interface, large *SiP* structures are not favourable owing to the free energy of the precipitates, as will be discussed later in this section. The concentration of Si self-interstitials drops rapidly (within a few nm) away from the interface into the Si bulk [106, 107]. In the *PSG* away from the moving *PSG/Si* interface, we expect the incoming oxygen molecules to break the Si-P bonds and result in the formation of Si-O bonds and the release of a P atom. Therefore, the *SiP* structures do not effectively move into the *PSG* or Si

during oxidation and remain limited to the *PSG/Si* interfacial region. Large *SiP* structures in Si (away from the *PSG/Si* interface) have only been reported [66] when the P and Si self-interstitial concentrations were exceptionally high (of the order of the Si atomic density).

The work of Solmi *et al.* [66] (co-authored by Nobili) attempted to revisit the solubility studies of Masetti *et al.* [10], which in turn was co-authored by both Solmi and Nobili. Since the solubility limit is defined as the concentration of the solute which is in equilibrium with a (an infinitely) large precipitate, Solmi *et al.* [66] attempted to form large *SiP* structures in the wafer bulk. Therefore, very heavy doses of P were implanted ~ 100 nm away from the *Si* surface and, unlike the work of Nobili *et al.* [9], the implantation damage was not recovered. *SNMS* (secondary neutral mass spectroscopy) profiles after several annealing durations at a given temperature allowed the authors to determine the solubility limit. The profiles displayed a peak at a location where the maximum implanted dose was present and which, according to TEM studies, corresponded to the presence of large rod-like *SiP* after annealing. The rapid drop in the profile after the peak was followed by a region with very high diffusivity and was more characteristic of a P diffusion profile in region 1 of conventional solar cell emitters. The intersection of the rapidly falling region (after the peak) and the region with high diffusivity was referred to as the shoulder of the P profile. Moreover, the concentration level of the shoulder was found to attain a constant value after prolonged annealing times, which, as per the authors, corresponded to the solubility limit since it represented the intersection of the mobile and immobile P under equilibrium conditions.

For temperatures below 750 ºC, the solubility limit reported by Solmi *et al.* [66] was in agreement with the electrically active P concentration in the specimens. However, for higher temperatures the authors found the solubility limit to be higher than the electrically active P concentration, with the discrepancy between the two increasing with temperature. The authors suggested that the discrepancy arises due to the presence of agglomerates, i.e. small clusters of phosphorus that are present along with the large rod like *SiP* precipitates. It must

be noted then, that the solubility limit reported by Solmi *et al.* [66] is the concentration of the solute plus the concentration of phosphorus in very small clusters. Therefore, the solubility limit reported by the authors does not correspond to the actual solubility limit. The (close to) true solute concentration which was in equilibrium with the large precipitates in [66] was the value of the electrically active phosphorus in that study, which can be taken as the actual solubility limit of P.

The solubility limit used in this work and listed in Table 2 is the concentration of the maximum electrically active P, as reported by Solmi *et al.* [66]. These values are in close agreement with those previously reported by Massetti *et al.* [10] that were used by Dunham in his precipitation model. In addition, the values of the constant a_1 in Table 2 is the same as that reported by Dunham while the value of the constant a_2 is in close agreement with Dunham's value. The constants a_1 and a_2 determine the precipitate/matrix interface energy and the precipitate strain energy, respectively. For larger precipitate sizes the excess energy of the precipitate free energy, in equation 2.24 of section 2.5.2.2, scales with the surface area of the precipitate. With the proposed values for the constants a_1 and a_2 in Table 2, the excess energy becomes proportional to the precipitate surface area for precipitate sizes greater than fifty P atoms. On the other hand, the value of the constant a_3 in this work varies from -0.13 to -0.36 for the temperature range 865 ºC to 968 ºC, while Dunham has suggested a constant value of -0.49 for a_3. In order to better understand the role of the constant a_3 in the Dunham precipitation model, one first needs to recognize the possible role of clusters in the course of the precipitation process.

Dopant atoms can be electrically inactive at high doping levels by forming clusters and/or precipitates [108]. Dopant clusters in *Si* comprise of dopant-vacancy complexes (A_mV_n) as opposed to dopant precipitates that have a zinc blend structure with both *Si* and the dopant atom having four nearest neighbours of the other species [109]. Clusters typically comprise of a few atoms while precipitates may contain thousands of dopant atoms. Boron and

antimony deactivate directly through precipitation [108] while arsenic, under common experimental conditions, deactivates via clustering [108]. Phosphorus, on the other hand, is thought to initially deactivate through the formation of dopant-vacancy clusters. These clusters can then evolve into precipitates as the annealing proceeds [108].

For phosphorus deactivation kinetics, the choice between precipitation and clustering depends on the thermal budget (temperature and time) of the process and the amount of dopant. If diffusion is too small for precipitation to occur and/or the doping level is not significantly high, donor deactivation via clustering needs to be taken into account [108]. For high doping levels and very large thermal budgets, clustering can be ignored and donor precipitation will dominate P deactivation. Solar cell emitters can comprise both clusters and precipitates since the thermal budgets of the $POCl_3$ process are neither very low nor very high.

Clustering models, that often consider clusters containing up to only four dopant atoms, cannot account for the formation of precipitates [110, 111]. On the other hand, precipitation models are not appropriate (accurate) when a significant proportion of the inactive dopant is trapped in small clusters. The Dunham precipitation model is also able to suggest a simplified treatment for clusters that form during the course of precipitation. Conventional clustering models, as per Dunham, can therefore be regarded as a subset of the present author's more general precipitation model. This is because the suggested values by Dunham for the constants a_1, a_2, m_1, m_2 and m_3 in equation 2.24 are such that the choice of the constant a_3 can allow for various deactivation kinetics that can range from a system with no cluster formation during deactivation to a system where the deactivation is primarily governed by cluster formation.

In his precipitation model, Dunham considered P deactivation directly via precipitation and arsenic deactivation to be affected by cluster formation. However, a year after the Dunham precipitation model Solmi *et al.* [66] reported the presence of P clusters under equilibrium

conditions that were responsible for the discrepancy between the solubility limit and the maximum electrically active P. The presence of such clusters under equilibrium conditions suggests that P is expected to deactivate initially via cluster formation as was previously also suggested by Takamura *et al.* [108] on the basis of thermal stability studies of common dopants in *Si*. Moreover, the discrepancy between solubility limit and electrically active P in the study of Solmi *et al.* [66] increased with temperature, which means that clustering kinetics will be affected by the diffusion temperature. According to Dunham [64] too, the very small precipitate sizes are expected to respond most rapidly to temperature changes and that one can attribute the differences in the experimental and simulated results in Dunham's study to the fact that the precipitate free energy in his model is considered independent of temperature.

In this work, the best results were obtained by choosing the constant a_3 to be temperature dependent, as shown in Table 2. In Figures 41-43, the precipitate free energy vs. the precipitate size as determined using the constants from Dunham and the constants used in this study are shown for various values of the solute supersaturation, C_P^+/C_{SS}. In Figures 41-43, the change in the solute free energy has been determined for a certain solute supersaturation at 890 ºC.

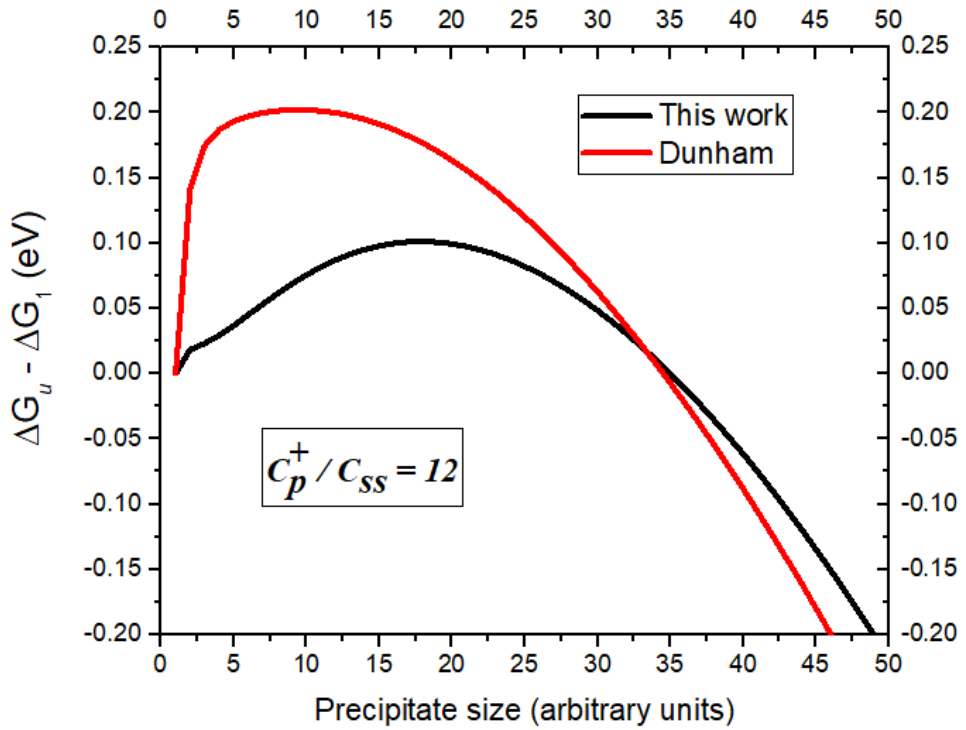


Figure 41: Precipitate free energy with respect to the free energy of the solute ($\Delta G_u - \Delta G_1$) as a function of the precipitate size (number of P atoms) for spherical P precipitates at 890 ºC and with a solute supersaturion, C_P^+ / C_{SS}, of 12. Compared to the findings of Dunham (red line), markedly lower free energy is predicted for the small precipitate sizes in this work (black line).

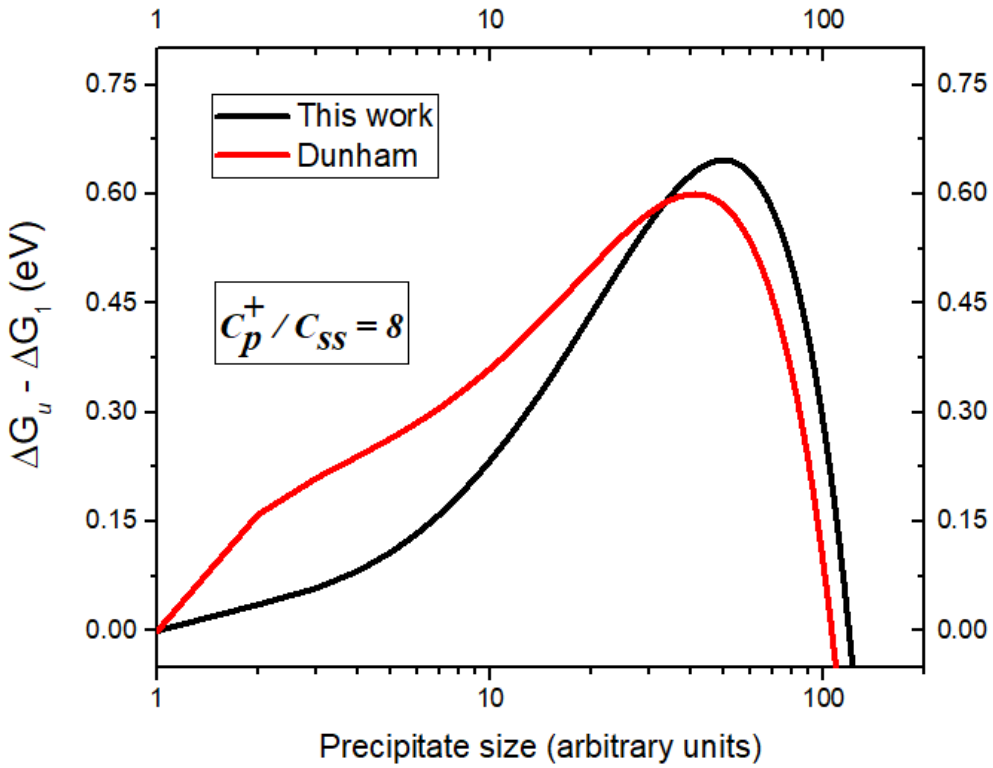


Figure 42: Precipitate free energy with respect to the free energy of the solute ($\Delta G_u - \Delta G_1$) as a function of the precipitate size (number of P atoms) for spherical P precipitates at 890 ºC and with a solute supersaturion, C_P^+ / C_{SS}, of 8. Compared to the findings of Dunham (red line), markedly lower free energy is predicted for the small precipitate sizes in this work (black line).

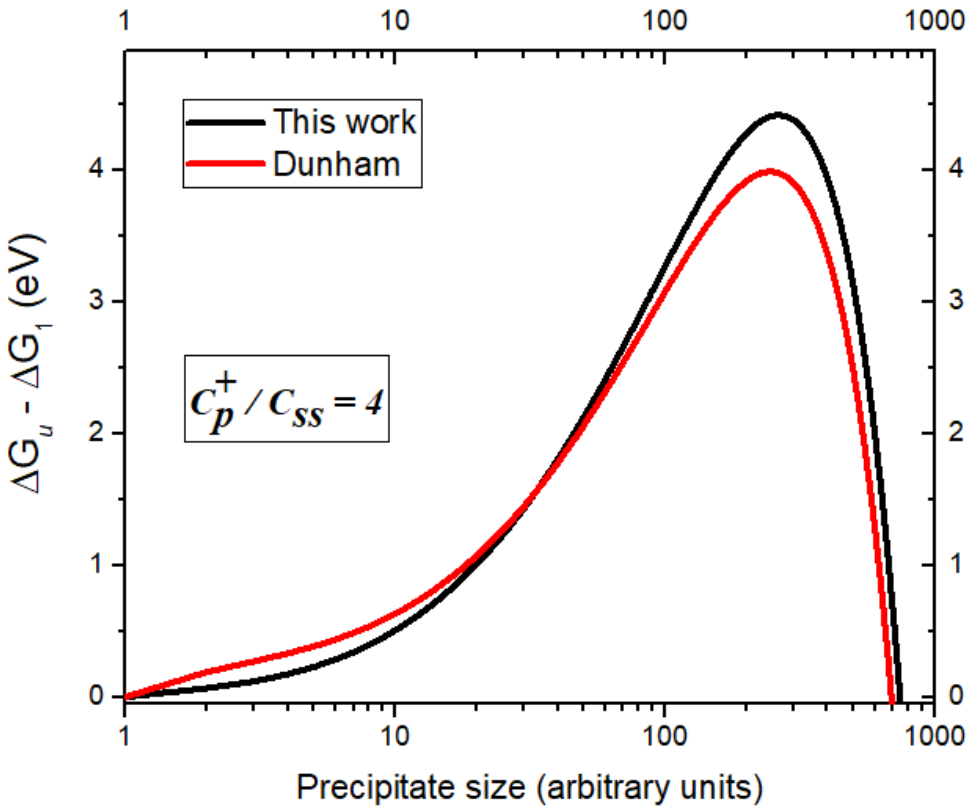


Figure 43: Precipitate free energy with respect to the free energy of the solute ($\Delta G_u - \Delta G_1$) as a function of the precipitate size (number of P atoms) for spherical P precipitates at 890 ºC and with a solute supersaturion, C_P^+/C_{SS}, of 4. Compared to the findings of Dunham (red line), markedly lower free energy is predicted for the small precipitate sizes in this work (black line).

For $C_P^+/C_{SS} = 12$ (Figure 41) the nucleation barrier for precipitate formation suggested in this work is smaller compared to that predicted by Dunham, however, the energy cost to form a small P cluster is relatively small when using the constants suggested in this work. When the solute supersaturation is reduced ($C_P^+/C_{SS} = 8$ and $C_P^+/C_{SS} = 4$ in Figures 42 and 43, respectively), the nucleation barrier for precipitate formation suggested in this work increases relative to that suggested by Dunham while the energy required to form a small P cluster remains low. The low energy cost associated with small P clusters, as determined in this study, is suggestive of the fact P will initially deactivate via forming clusters and that these clusters can then evolve into precipitates as the annealing proceeds. This has previously been suggested by Takamura *et al.* [108] and can be inferred from the data of Solmi *et al.* [66], wherein it was reported that small P clusters exist along with large SiP precipitates even under equilibrium conditions. On the other hand, the Dunham model predicts that P deactivates directly via precipitation. One of the reasons why Dunham might have

considered P deactivation via direct precipitation is that at the time the data of Solmi *et al.* [66] was not available. It is pertinent to mention that Dunham actually reported a value of -4.9 for a_3 as opposed to the value of -0.49 listed in Table 2 and used (for the red curves) in Figures 41-43. This is because the Dunham reported value is very likely a typographical error. This discrepancy becomes apparent from Figure 9 in Dunham [64].

Precipitate and/or cluster concentration, f_u, versus precipitate size, u, at the *Si* surface for 4 different processes (6, 11, 12, 13) conducted at 890 ºC are shown in Figure 44. The longer process (process 6 - 14.25 mins) was carried out under moderate $POCl_3$ partial pressure (0.1%). Since precipitate growth is diffusion limited [70] the very large precipitate sizes were not attained for small diffusion durations. In Figure 45, the precipitate concentration versus precipitate size is shown for samples that were doped under moderate $POCl_3$ partial pressures (0.1%) at different temperatures for short durations (5.75 minutes).

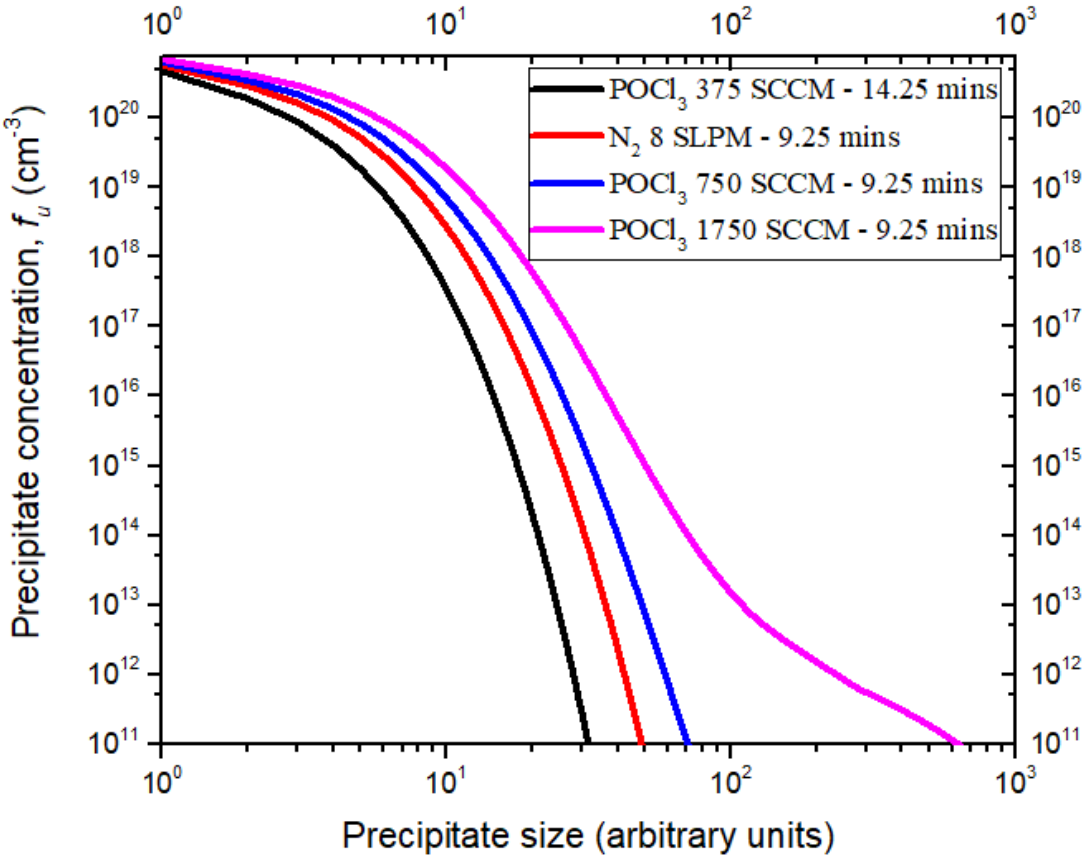


Figure 44: Precipitate concentration vs precipitate size (number of P atoms) for spherical P precipitates at the *Si* surface as determined at the end of a simulation. The $POCl_3$ partial pressures for processes 6 (black), 13 (red), 11 (blue) and 12 (pink) were 0.1%, 0.16%, 0.21% and 0.53%, respectively. Diffusion duration for process 6 (black) was 14.25 minutes while for all remaining processes (11, 12 and 13) the diffusion duration was 9.25 minutes. Diffusion temperature was 890 ºC for all processes.

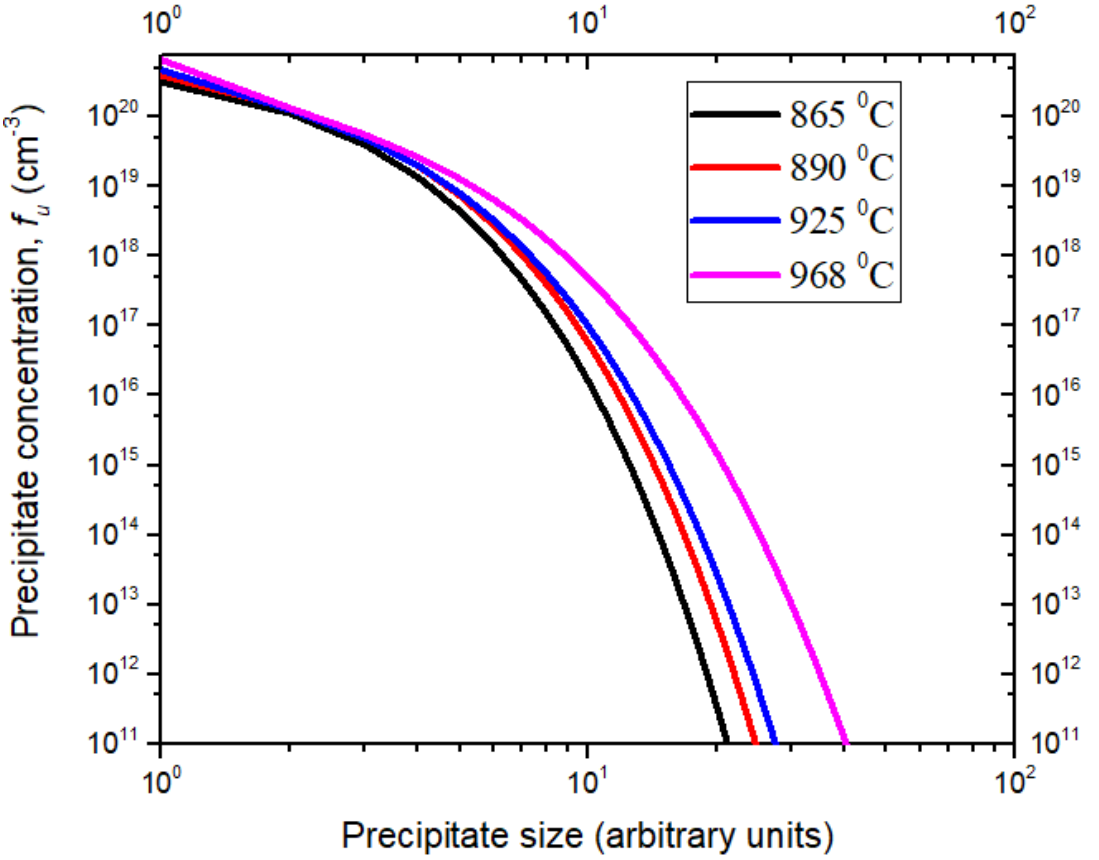


Figure 45: Precipitate concentration vs precipitate size (number of P atoms) for spherical P precipitates at the *Si* surface as determined at the end of a simulation, for processes conducted at different temperatures. Diffusion duration (5.75 minutes) and gas flow composition ($POCl_3$ = 375, O_2 = 500, N_2 = 13125 SCCM) was the same for all processes.

In summary most of the constants listed in Tables 1 and 2 are in good agreement with the values suggested in the literature. Previous studies have often reported the experimental values for only particular constants pertaining to P diffusion (e.g. the supersaturation factor, the solubility limit, the diffusivity under intrinsic conditions, the percolation threshold concentration, etc). The diffusion model developed in this work, however, is not limited to only a particular feature of the P profile but rather the entire P profile and suggests values for the different model parameters that are in good agreement with their literature values.

5.3 Concentration profiles of electrically active P

In this section, the correlation between total and electrically active P profiles after $POCl_3$ diffusion is discussed. Also shown is the effectiveness of the high temperature low duration processes (that were discussed in chapter 1) in reducing inactive P.

Electrically active P concentration profiles for various temperatures and durations are reported in Figure 46 and in Figure 47. These electrical profiles are similar to the ones reported by several other authors who have used a $POCl_3$ source [103, 104, 105]. In addition, the correlation between simulated total and electrically active P in this study conforms to the form obtained by Fair and Tsai [15]. The empirical form proposed by Fair & Tsai is given by,

$$C_P = n + K_E n^3 \tag{5.2}$$

where C_P is the total phosphorus concentration, n is the electron concentration that can be approximated by the solute concentration ($C_P^+ = n$) and K_E is a constant. Fair & Tsai reported a value of $2.04 \times 10^{-41} cm^6$ for K_E, however, in this study a lower value (10^{-41}) of K_E can somewhat allow for a close relationship between simulated total and electrically active P. In Figure 48, the total and electrically active P profiles, as determined in this study at a temperature of 890 ºC and 14.25 min diffusion, are shown. Also depicted is the resulting total P from the electrically active P using relation 5.2, where a value of 10^{-41} has been used for K_E.

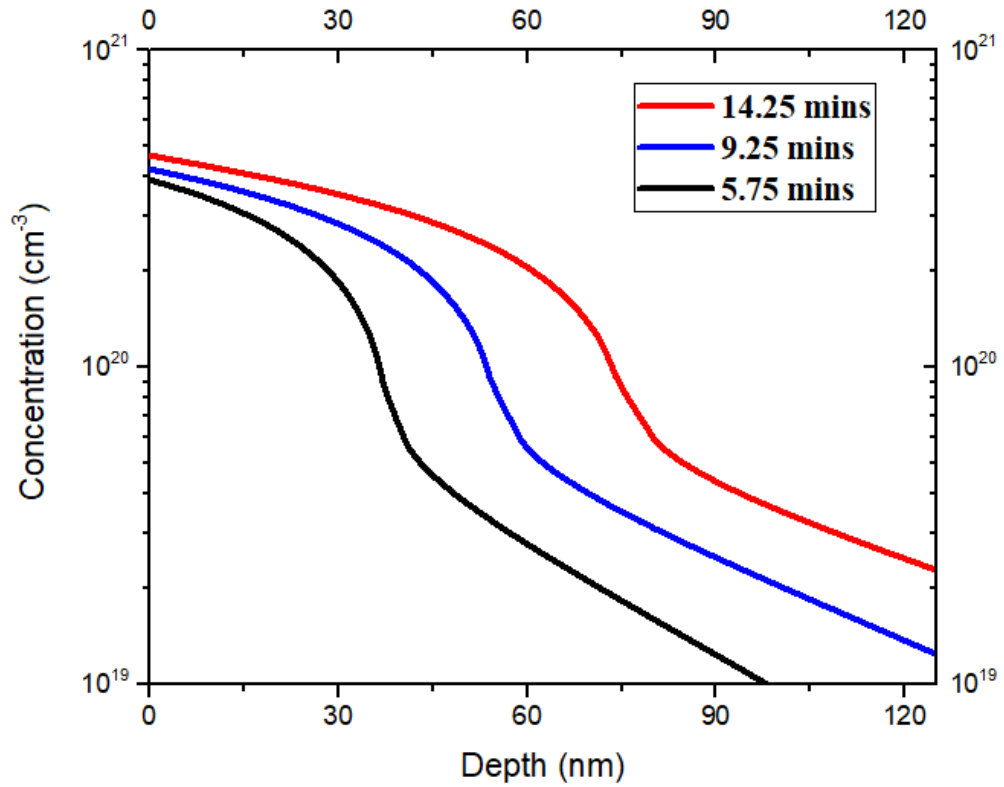


Figure 46: Simulated electrical profiles for processes 4, 5 and 6. Temperature (890 ºC) and gas flow composition ($POCl_3$ = 375 SCCM, O_2 = 500 SCCM and N_2 = 13125 SCCM) was same for all processes.

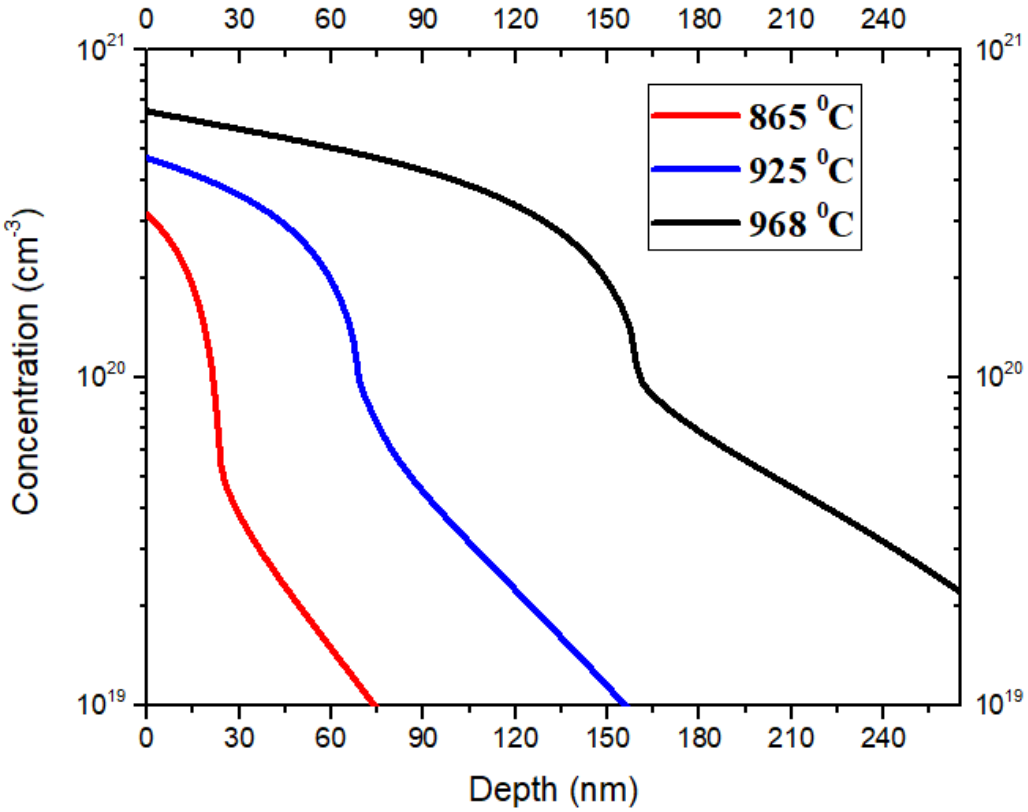


Figure 47: Simulated electrical profiles for processes 4, 8 and 9. Diffusion duration (5.75 minutes) and gas flow composition ($POCl_3$ = 375 SCCM, O_2 = 500 SCCM and N_2 = 13125 SCCM) was same for all processes.

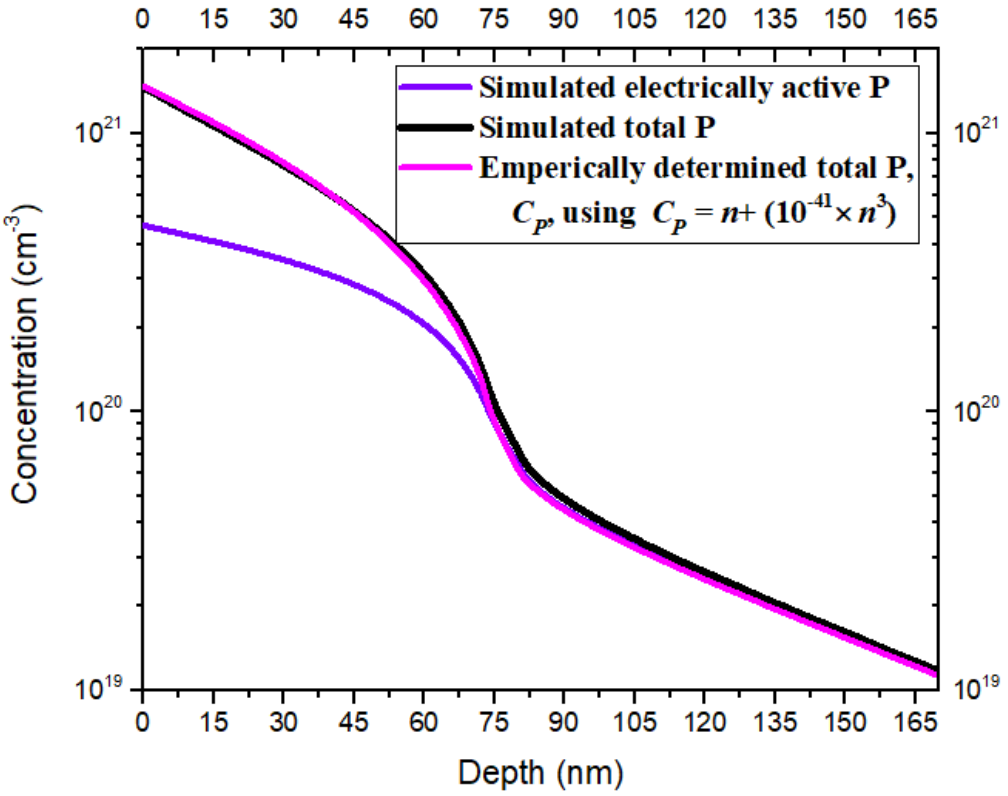


Figure 48: Simulated total, simulated electrically active and empirically determined (using equation 4.18) total P profile for process 6 (Temperature = 890 ºC, time = 14.25 minutes, $POCl_3$ = 375 SCCM, O_2 = 500 SCCM and N_2 = 13125 SCCM).

For the short diffusion durations used in this work, we expect very high (greater than solubility) solute concentrations in region 1 of the P profile. This is because precipitation is diffusion limited (from Ham [70]) and as the diffusion duration increases the precipitates will grow in size resulting in a reduction of the solute concentration in region 1. Due to the moderate diffusion durations used by Fair & Tsai [15], the solute concentrations obtained by the authors in region 1 was lower (but still higher than solubility) compared to those found in this work and is the probable reason for the different K_E values. In the year when the Fair & Tsai paper was published, Massetti *et al.* [10] had reported electrically active and total P profiles after prolonged annealing using $POCl_3$ source. In that study, the electrically active P concentrations had acquired values very close to the equilibrium values and were more typical of the solubility limit. The solubility limit of P proposed by Massetti *et al.* [10] was used by Dunham in his precipitation model.

It is pertinent to mention that the $POCl_3$ method (or any surface in-diffusion method) is not a good candidate to study solubility limits. This is because in such methods, the surface concentration does not remain constant and there is little time for the solute near the surface to acquire close to equilibrium values. The overall effect is that there exists a gradient in the electrical profile in region 1, where the surface solute concentration is often above the solubility limit. This is perhaps the reason why Massetti *et al*. [10] noted that the plateau in the electrical profiles are not exactly flat, despite the prolonged annealing durations.

It then remained to be seen if the proposed method (outlined in chapter 1) for reducing inactive P is effective. In Figure 49, simulated total and electrically active *P* is shown for two processes with the same gas flow composition but different diffusion temperatures and durations. The overall $POCl_3$ flow is kept small for both processes shown in Figure 49 while the diffusion duration for each process ensures that a plateau depth of ~40 nm is achieved. It can be seen that the ratio of the electrically active *P* to total *P* increases significantly for the short duration high temperature process. Due to the higher solubility limit of the dopant at elevated temperatures, there is more of the solute for a given amount of dopant. In addition, the large diffusivities at high temperatures allow formation of shallow emitters when sufficient time has not elapsed for the surface concentration to rise significantly beyond the solubility limit.

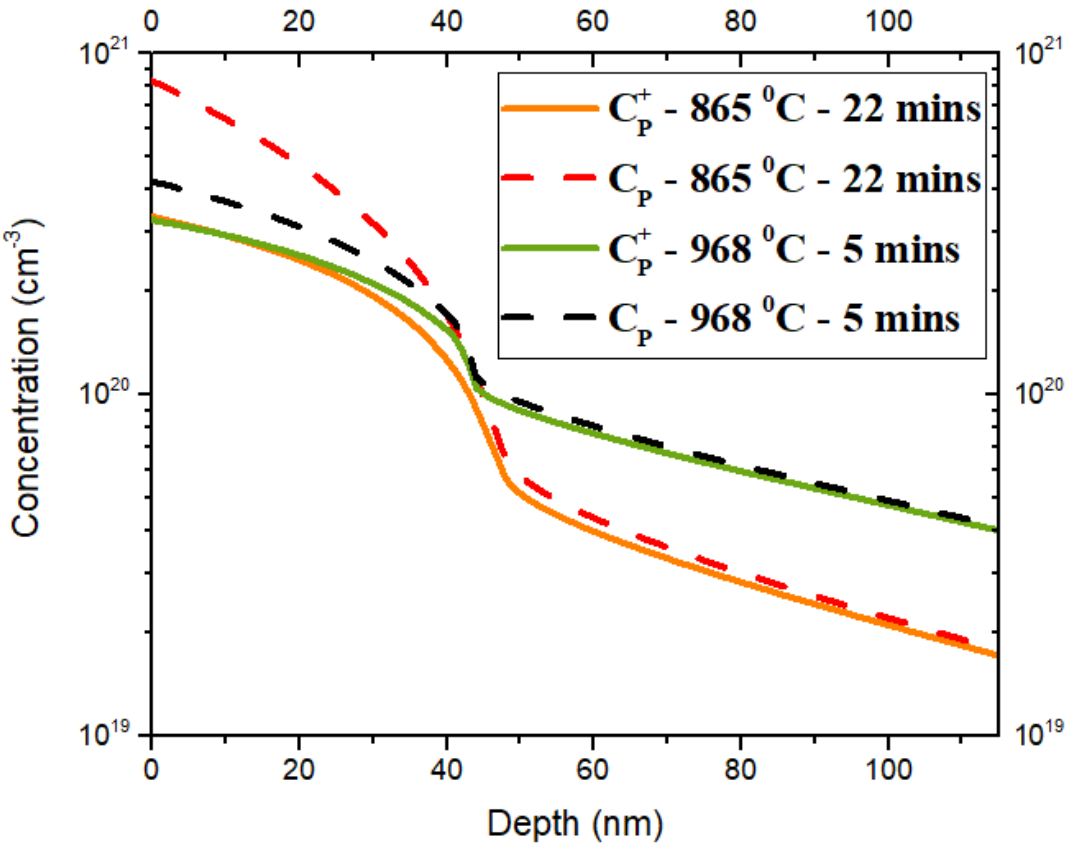


Figure 49: Simulated total C_P (dashed) and electrically active C_P^+ P profiles for low (865 ºC, 22 mins) and high (968 ºC, 5 mins) temperature processes using an overall gas composition (N_2 = 13300 SCCM, O_2 = 500 SCCM, $POCl_3$ = 200 SCCM) with small $POCl_3$ partial pressures.

The P surface concentration increases rapidly with diffusion time when the $POCl_3$ partial pressure is high. However, even for the case of low $POCl_3$ partial pressures, the increase in the surface concentration with diffusion duration is significantly fast. As a result, the surface concentration does not remain at around the solubility limit for a considerable duration. This means that if the process is stopped at a point when the surface concentration is at (or just above) the solubility limit, significant plateau depths (and therefore electrically active P) would not be achieved for the low temperature process. This is shown in Figure 50 where the low temperature process of Figure 49 is shown again in comparison with same high temperature process of Figure 49, except that the diffusion duration of the low temperature process has been adjusted such that the two processes have the same surface concentration.

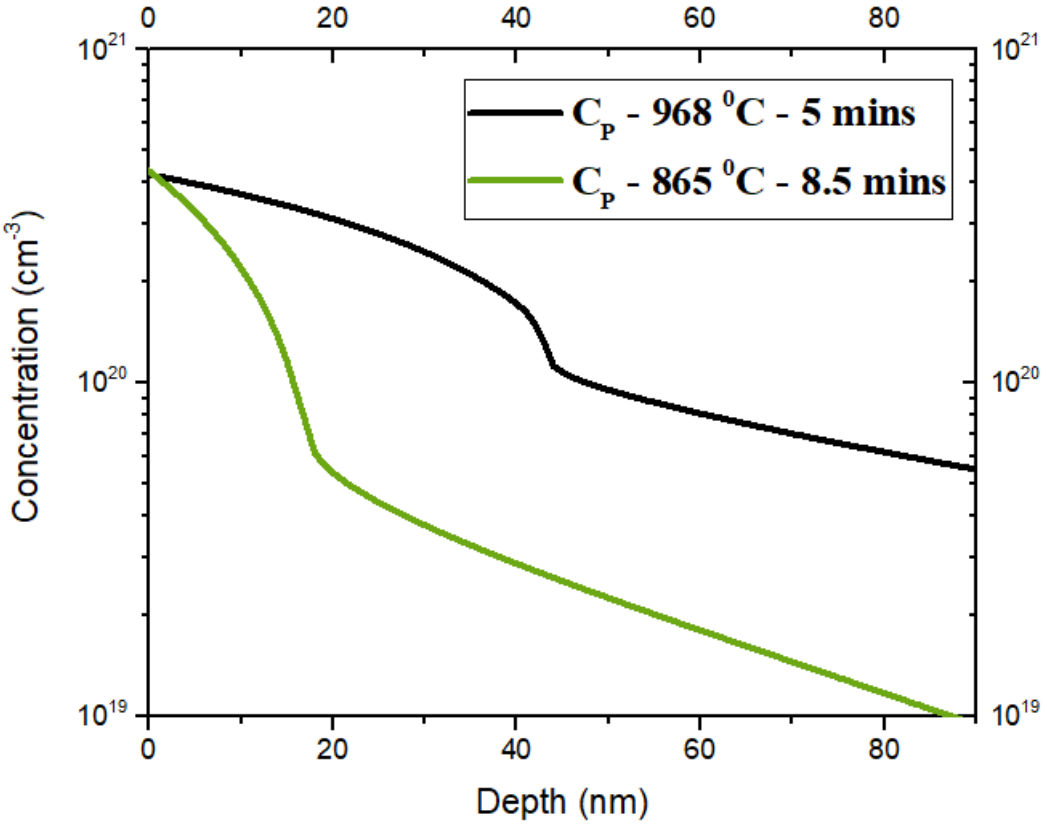


Figure 50: Simulated total C_P P profiles for low (865 ºC, 8.5 mins) and high (968 ºC, 5 mins) temperature processes using an overall gas composition (N_2 = 13300 SCCM, O_2 = 500 SCCM, $POCl_3$ = 200 SCCM) with small $POCl_3$ partial pressures. The diffusion durations are chosen such that the final surface concentrations of the two processes are the same (see text for explanation).

5.4 Summary

In this chapter, the results of the simulations have been discussed in light of the values used for the various constants. Rather than being a purely empirical model the approach has been to analyse the physical processes taking place so that some feeling for the values of the physically important variables is obtained. Not only are the diffusion simulations in very good agreement with experimental results but also the model parameters are in good agreement with previous estimates. However, unlike previous studies that reported values for only a few constants and therefore remained limited to only certain features of the P profile, the current model is able to model P diffusion accurately in all three regions over a relatively wide range of temperatures all using the same fitting constants. In addition, the correlation between electrically active P and total P is typical of that observed after conventional $POCl_3$ diffusion.

CHAPTER 6
CONCLUSIONS AND FUTURE WORK

This thesis discusses a new phosphorus diffusion model. The model is argued to be consistent with previous experimental findings and is able to reasonably predict *P* profiles in *Si* over a wide range of processing conditions. In addition, the model uses a set of well-defined constants and requires only the processing conditions as starting parameters. On the other hand, conventional P diffusion models are often limited to only certain features of the P profile (e.g. profile of the electrically active P only or profile of P in only region 1 or in region 3) and are not able to demonstrate very good simulation accuracies over a range of temperatures by using the same fitting parameters.

This work brings together several features of P diffusion into a single simulation framework. By introducing the appropriate recombination mechanism between vacancies and interstitials, it is shown, from first principles, that the conventional understanding of P diffusion being mediated by vacancies and excess interstitials at high and low electron concentrations, respectively, can allow for accurate modelling of P profiles. Formation of phosphorus vacancy pairs at high doping level facilitates the suppression of excess interstitial concentrations with the help of surface injected vacancies and thereby restoration of point defect equilibrium, hence explaining the changeover from interstitial to vacancy mediated diffusion.

This is the first quantitative P diffusion model that assumes that the point defect supersaturation arises because of the kick out reactions in the wafer and not due to injection of interstitials from the surface, which in turn is consistent with experimental findings. Moreover, incorporation of phosphorus precipitates and/or clusters at high doping levels in a P diffusion model has been performed for the first time in this study. The relationship between total and electrically active P conforms to the form previously obtained by other studies.

The short-duration processes suggested in this study for reduced inactive P can have direct applicability in industrial processing provided delivery of a homogeneous gas mixture for very short diffusion durations under low $POCl_3$ partial pressures is achieved. Future work, must therefore aim to realise such a gas delivery system. This might require a comprehensive study of fluid dynamics within the quartz tube, however, it first needs to be seen whether simple experiments on a diffusion furnace that uses injectors can achieve homogeneous distribution of gases within very short durations. This is because diffusion furnaces that use injectors inject the gas mixture locally instead of injecting the gas at one end of the tube (via a spigot) and can thus significantly reduce the residence time of the system. The optimum location of these injectors can be determined using straightforward sheet resistance measurements and by using conditions of light doping. As discussed in chapter 1, gas non-homogeneity can be detected via sheet resistance measurements if the doping level is below the solubility limit.

Future work should also focus on improving upon the diffusion coefficients extracted in this work after acquiring both total and electrically active P profiles. Moreover, the empirical equations for the surface concentration in this study are only valid for the processing range used in this work. Future work should aim to extend this model to an even wider range of processing conditions.

REFERENCES

[1] Geir Linløkken and Steffen Frölich, "Technical Stock Analysis - for reduced risks and increased returns", Investtech.com AS, 2004.

[2] M. Metayer, C. Breyer and H.-J. Fell, “The projections for the future and quality in the past of the World Energy Outlook for solar PV and other renewable energy technologies”, 31st European Photovoltaic Solar Energy Conference, Hamburg, Germany, 14-18 September 2009.

[3] Vishal Shah and Jerimiah Booream-Phelps, “F.I.T.T. for Investors: Crossing the Chasm”, Technical Report, Deutsche Bank Markets Research, Frankfurt, Germany, 2015.

[4] International Energy Agency (IEA), "Technology Roadmap Solar Photovoltaic Energy", 2014 Edition.

[5] Science Kick, "Working Principle of junction solar cells", website accessed on 21st August 2016.

http://www.science-kick.com/solar-cell-type/working-principle-of-junction-solar-cells

[6] Hocine Ghembaza, Abdellatif Zerga, Rachid Saïm, “Efficiency Improvement Of Crystalline Silicon Solar Cells By Optimizing The Doping Profile Of $POCl_3$ Diffusion”, International Journal of Scientific & Technology Research, Volume 3, Issue 1, Pages 1-5, January 2014.

[7] J. Mayandi, E. S. Marstein, M. Syre, B. R. Olaisen, B. Thomassen, A. Holt, L. Vines, “The effect of P concentration on gettering of multicrystalline Si wafers”, 24th European Photovoltaic Solar Energy Conference, Hamburg, Germany, 21-25 September 2009.

[8] Filip Granek, Martin Hermle, Christian Reichel, Andreas Grohe, Oliver Schultz-Wittmann and Stefan Glunz, “Positive effects of front surface field in high-efficiency back-contact back-junction n-type silicon solar cells”, 33rd IEEE Photovoltaic Specialists Conference (PVSC), 11-16 May 2008.

[9] D. Nobili, A. Armigliato, M. Finetti, and S.Solmi, "Precipitation as the phenomenon responsible for the electrically inactive phosphorus in silicon", Journal of Applied Physics, Volume 53, Issue 3, Pages 1484-1491, (1982).

[10] G. Masetti, D. Nobili and S. Solmi, “Profiles of Phosphorus Predeposited in Silicon and Carrier Concentration in Equilibrium with SiP precipitates”, 3rd International

Symposium on Silicon Materials Science and Technology, edited by H. R. Huff and E. Sirtl (Electrochemical Society, Princeton), Page 648-657, 1977.

[11] P. Ostoja, S. Guerri, P. Negreni and S. Solmi, “The effects of phosphorus precipitation on the open-circuit voltage in n^+ / p Silicon solar cells”, Solar Cells, Volume 11, Issue 1, Pages 1-12, (1984).

[12] A. Kimmerle, A. Wolf, U. Belledin and D. Biro, “Modelling carrier recombination in highly phosphorus-doped industrial emitters”, Energy Procedia, Volume 8, Pages 275-281 (2011).

[13] A. Bentzen, “Phosphorus diffusion and gettering in silicon solar cells”, PhD thesis, University of Oslo, Department of Physics, (2006).

[14] F. A. Kroger, R. B. Fair, and J. C. C. Tsai., “Discussion of "A quantitative model for diffusion of phosphorus in silicon and the emitter dip effect" [R. B. Fair and J. C. C. Tsai pp. 1107-1118, Volume 124, No. 7]”, Journal of the Electrochemical Society, Volume 125, Issue 6, Pages 995–998, (1978).

[15] R. B. Fair and J. C.C. Tsai, “A quantitative model for diffusion of phosphorus in silicon and the emitter dip effect”, Journal of the Electrochemical Society, Volume, 124, Issue 7, Pages 1107-1118, (1977).

[16] Victor Prajapati, “Advanced Front Side Technologies in Crystalline Silicon Solar Cells”, PhD thesis, Katholieke University Leuven, Faculty of Engineering, 2013.

[17] J. Lindmayer and J. F. Allison, "The violet cell: an improved silicon solar cell", Solar Cells, Volume 29, Issues 2-3, Pages 151-166, (1990).

[18] M. M. Hilali, A. Rohatgi and S. Asher, “Development of Screen-Printed Silicon Solar Cells With High Fill Factors on 100 Ω/sq Emitters”, IEEE Transactions on Electron Devices, Vol. 51, Issue 6, Pages 948-955, (2004).

[19] Kishan Devappa Shetty, Mathew B. Boreland, Vinodh Shanmugam, Jessen Cunnusamy, Chun-Kwei Wu, Scott Iggo, Homer Antoniadis, “Lightly Doped Emitters for High Efficiency Silicon Wafer Solar Cells”, Energy Procedia Volume 33, Pages 70-75, (2013).

[20] Daniel Inns, "Understanding metal induced recombination losses in silicon solar cells with screen printed silver contacts", Energy Procedia, Volume 98, Issue, Pages 23-29, (2016).

[21] Chetan Singh Solanki, “Solar Photovoltaics: Fundamental, Technologies and Applications”, Prentice-hall Of India Pvt Ltd, 2009.

[22] Sudipto R. Roy and A. Haji-Sheikh, “Modeling and Analysis of a New Multiwafer Hot Wall Phosphorus Doping Reactor”, Journal of the Electrochemical Society, Volume 143, Issue 4, Pages 1362-1371, (1996).

[23] M. S. R. Heynes and J. T. Wilkerson, "Phosphorus Diffusion in Silicon Using $POCl_3$", Electrochemical Technology, Volume 5, Issues 9-10, Pages 464-467, (1967).

[24] P. Negrini, D. Nobili, and S. Solmi, “Kinetics of Phosphorus Predeposition in Silicon using $POCl_3$” Journal of The Electrochemical Society, Volume 122, Issue 9, Pages 1254-1260, (1975).

[25] Hongzhao Li, Fa-Jun Ma, Ziv Hameiri, Stuart Wenham and Malcom Abbott, "On elimination of inactive phosphorus in industrial $POCl_3$ diffused emitters for high efficiency silicon solar cells", Solar Energy Materials and Solar Cells, Volume 171, Pages 213-221, (2017).

[26] Karthick Murukesan, Sandeep Kumbhar, A. K. Kapoor, A. Dhaul, S. Saravanan, Richard Pinto, B. M. Arora, "POCl3 diffusion process optimization for the formation of emitters in the crystalline silicon solar cells", 40th IEEE Photovoltaics Specialist Conference (PVSC), 8-13 June 2014.

[27] Peter Pichler, “Intrinsic Point defects, Impurities, and Their Diffusion in Silicon”, edited by S. Selberherr, Springer-Verlag Wien, 2004.

[28] Fick, A. (1855), “On liquid diffusion”, Journal of Membrane Science, Volume 100, Issue 1, Pages 33-38, (1995).

[29] S. Coffa, F. Priolo, Emanuele Rimini and J. M. Poate, "Crucial Issues in Semiconductor Materials and Processing Technologies", Kluwer Academic Publishers, Amsterdam, 1992.

[30] S. M. Hu, “On interaction potential, correlation factor, vacancy mobility, and activation energy of impurity diffusion in diamond lattice”, Physica Status Solidi B, Volume 60, Issue 2, Pages 595-604, (1973).

[31] P. M. Fahey, P. B. Griffin, J. D. Plummer, “Point defects and dopant diffusion in silicon”, Reviews of Modern Physics, Volume 61, Issue 2, Pages 289-384, (1989).

[32] S. T. Dunham and C. D. Wu, “Atomistic Models of Vacancy-Mediated Dopant Diffusion in Silicon”, Journal of Applied Physics, Volume 78, Issue 4, Pages 2362-2366, (1995).

[33] D. Mathiot and J.C. Pfister, “High concentration diffusion of P in Si : a percolation problem ?” Journal de Physique Lettres, 1982, Volume 43, Issue 12, Pages 453-459, (1982).

[34] S. M. Sze, “Physics of semiconductor devices”, second edition, Wiley, New York (1981).

[35] C. D. Thurmond, “Standard thermodynamic functions for formation of electrons and holes in Ge, Si, GaAs, and GaP.” Journal of the Electrochemical Society, Volume 122, Issue 8, Pages 1133–1141, (1975).

[36] D. H. Neuhaus, P. P. Altermatt, R. P. Starrett, A. G. Aberle, “Determination of the density of states in heavily doped regions of silicon solar cells”, Solar Energy Materials & Solar Cells, Volume 65, Pages 105-110, (2001).

[37] R. K. Jain, "Calculation of the built-in electric field diffusion enhancement factor", International Journal of Electronic, Volume 44, Issue 3, Pages 333-335, (1978).

[38] Eileen Tannenbaum, "Detailed analysis of thin phosphorus-diffused layers in p-type silicon", Solid-State Electronics, Volume 2, Issues 2-3, Pages 123-132, (1961).

[39] J. M. Fairfield and B. J. Master, “Self-Diffusion in Intrinsic and Extrinsic Silicon”, Journal of Applied Physics, Volume 38, Issue 8, Pages 3148-3154, (1967).

[40] B. J. Masters and J. M. Fairfield, “Arsenic Isoconcentration Diffusion Studies in Silicon”, Journal of Applied Physics, Volume 40, Issue 6, 2390-2394, (1969).

[41] S. M. Hu and S. Schmidt, "Interactions in Sequential Diffusion Processes in Semiconductors", Journal of Applied Physics, Volume 39, Issue 9, Pages 4272-4283, (1968).

[42] Professor Scott T. Dunham, Lecture notes, Washington University, website accessed on 15th April 2015.

http://dunham.ee.washington.edu/ee528/

http://dunham.ee.washington.edu/ee528/notes/pointdefects.pdf

http://dunham.ee.washington.edu/ee528/notes/diff.pdf

[43] M. Finetti, P. Negrini, S. Solmi, and D. Nobili, "Electrical Properties and Stability of Supersaturated Phosphorus-Doped Silicon Layers", Journal of the Electrochemical Society, Volume 128, Issue 6, Pages 1313-1317, (1981).

[44] S. M. Hu, P. Fahey, and R. W. Dutton, “On models of phosphorus diffusion in silicon”, Journal of Applied Physics, Volume 54, Issue 12, Pages 6912-6922, (1983).

[45] P. Fahey, R. W. Dutton and S. M. Hu, “Supersaturation of self-interstitials and undersaturation of vacancies during phosphorus diffusion in silicon”, Applied Physics Letters, Volume 44, Issue 8, Pages 777-779, (1984).

[46] S. T. Dunham, “A Quantitative Model for the Couple Diffusion of Phosphorus and Point Defects in Silicon”, Journal of the Electrochemical Society, Volume 139, Issue 9, Pages 2628-2636, (1992).

[47] A. Bentzen, A. Holt, J. S. Christensen and B. G. Svensson, "High Concentration in-diffusion of phosphorus in Si from a spray-on source", Journal of Applied Physics, Volume 99, Issue 6, Pages 064502(1-8), (2006).

[48] F. N. Schwettmann and D. L. Kendall, "Carrier Profile Change for Phosphorus-Diffused Layers on Low Temperature Heat Treatment", Applied Physics Letters, Volume 19, Issue 7, Pages 218-220, (1971).

[49] F. N. Schwettmann and D. L. Kendall, "On the nature of the kink in the carrier profile for phosphorus-diffused layers in silicon", Applied Physics Letters, Volume 21, Issue 1, Pages 2-4, (1972).

[50] S. M. Hu, "Chapter 5 - Diffusion in Silicon and Germanium", Atomic Diffusion in Semiconductors, edited by D. Shaw, Plenum Press New York, 1973.

[51] M. Yoshida, E. Arai, H. Nakamura, and Y. Terunuma, "Excess vacancy generation mechanism at phosphorus diffusion into silicon", Journal of Applied Physics, Volume 45. Issue 4, Pages 1498-1506, (1974).

[52] M. Yoshida, "Excess vacancy generation by E-center dissociation in the case of phosphorus diffusion in silicon", Journal of Applied Physics, Volume 48, Issue 6, Pages 2169-2174, (1977).

[53] Masayuki Yoshida, "Numerical Solution of Phosphorus Diffusion Equation in Silicon", Japanese Journal of Applied Physics, Volume 18, Issue 3, Page 479-489, (1979).

[54] R. N. Ghoshtagore, "Low concentration diffusion in silicon under sealed tube conditions", Solid-State Electronics, Volume 15, Issue 10, Pages 1113-1120 (1972).

[55] S. Matsumoto, M. Yoshida, and T. Niimi, "The Confirmation of the Surface Effect upon Phosphorus Diffusion into Silicon", Japanese Journal of Applied Physics, Volume 13, Issue 11, Pages 1899-1900, (1974).

[56] A. Ural, P. B. Griffin, and J. D. Plummer, “Fractional contributions of microscopic diffusion mechanisms for common dopants and self-diffusion in silicon”, Journal of Applied Physics, Volume 85, Issue 9, Pages 6440-6446, (1999).

[57] P. M. Fahey, "Point defects and dopant diffusion in silicon", Ph.D. thesis, Stanford University, Department of Electrical Engineering, 1985.

[58] F. F. Morehead and R. F. Lever, "Enhanced "tail" diffusion of phosphorus and boron in silicon: Self-interstitial phenomena", Applied Physics Letters, Volume 48, Issue 2, Pages 151-153, (1986).

[59] B. J. Mulvaney and W. B. Richardson, "A Model for Defect-Impurity Pair Diffusion in Silicon", Applied Physics Letters, Volume 51, Issue 18, Pages 1439-1441, (1987).

[60] H. U. Jager, T. Feudel and S. Ulbric, “Modeling of Defect-Phosphorus Pair Diffusion in Phosphorus-Implanted Silicon”, Physica Status Solidi A, Volume 116, Issue 2, Pages 571-581, (1989).

[61] Masashi Uematsu. “Simulation of boron, phosphorus, and arsenic diffusion in silicon based on an integrated diffusion model, and the anomalous phosphorus diffusion mechanism”, Journal of Applied Physics, Volume 82, Issue 5, Pages 2228-2246, (1997).

[62] A. Nylandsted Larsen, K. Kyllesbech Larsen, P E. Andersen, and B. G. Svensson, "Heavy doping effects in the diffusion of group IV and V impurities in silicon", Journal of Applied Physics, Volume 73, Issue 2, Pages 691-698 (1993).

[63] S.T. Dunham, Alp H. Gencer, S. Chakravarthi, “Modeling of dopant diffusion in silicon”, IEICE Transactions on Electronics, Volume E82C, Issue 6, Pages 800-812, (1999).

[64] Scott T. Dunham, "Modeling of the Kinetics of Dopant Precipitation in Silicon", Journal of the Electrochemical Society, Volume 142, Issue 8, Pages 2823-2828, (1995).

[65] D. Nobili, A. Carabelas, G. Celloti, and S. Solmi, "Precipitation as the Phenomenon Responsible for the Electrically Inactive Arsenic in Silicon", Journal of the Electrochemical Society, Volume 130, Issue 4, Pages 922-928, (1983).

[66] S. Solmi, A. Parisini, R. Angelucci, A. Armigliato, D. Nobili and L. Moro. "Dopant and carrier concentration in Si in equilibrium with monoclinic SiP precipitates", Physical Review B, Volume 53, Issue 12, Pages 7836-7841, (1996).

[67] Professor Scott T. Dunham, Lecture notes, Washington University, website accessed on 15th April 2015.

http://dunham.ee.washington.edu/ee528/notes/precip.pdf

[68] Bart Trzynadlowski, "Reduced Moment-Based Models for Oxygen Precipitates and Dislocation Loops in Silicon", Doctor of Philosophy thesis, University of Washington, Department of Electrical Engineering, 2013.

[69] Hsiu-Wu Guo, "Diffusion and precipitation models for silicon gettering and ultra shallow junction formation", Doctor of Philosophy thesis, University of Washington, Department of Electrical Engineering, 2008.

[70] F.S. Ham, "Diffusion-Limited Growth of Precipitate Particles", Journal of Applied Physics, Volume 30, Issue 10, Pages 1518-1525, (1959).

[71] A. Armigliato, D. Nobili, M. Servidori, and S. Solmi, "SiP precipitation within the doped silicon lattice, concomitant with phosphorus predeposition", Journal of Applied Physics, Volume 47, Issue 12, Pages 5489-5491, (1976).

[72] Four Point Probes, a division of Bridge Technologies, website accessed on 13th June 2016,

http://four-point-probes.com/four-point-probe-manual/

[73] Biswajit Saha and Purushottam Chakraborty, "Inelastic ion-surface collisions: Understanding secondary emission of molecular ions", Journal of Physics: Conference Series, Volume 185, Pages 012039(1-6), (2009).

[74] Anna M. Belu, Daniel J. Graham, David G. Castner, "Time-of-flight secondary ion mass spectrometry: techniques and applications for the characterization of biomaterial surfaces", Biomaterials, Volume 24, Issue 21, Pages 3635-3653, (2003).

[75] Leonard J. Brillson, "An essential guide to electronic material surfaces and interfaces", John Wiley & Sons, Ltd, Chichester, UK, 2016.

[76] Biswajit Saha and Purushottam Chakraborty, "MCs_n^+-SIMS: an innovative approach for direct compositional analysis of materials without standards", Energy Procedia, Volume 41, Pages 80-109, (2013).

[77] H. Gnasner and H. Oechsner, “SIMS depth profile analysis using MCs^+ molecular ions”, Fresenius' Journal of Analytical Chemistry, Volume 341, Issue 1-2, Pages 54-56, (1991).

[78] Y. Gao, “A new secondary ion mass spectrometry technique for III-V semiconductor compounds using the molecular ions CsM+”, Journal of Applied Physics, Volume 64, Issue 7, Pages 3760-3762, (1988).

[79] Biswajit Saha, Purushottam Chakraborty, Hubert Gnasner, Manjula Sharma, Milan K. Sanyal, “Exact compositional analysis of SiGe alloys by matrix effect compensated MCs^+-SIMS", Applied Physics A: Materials Science & Processing, Volume 108, Issue 3, Pages 671-677, (2012).

[80] K. Wittmaack, "Basic requirements for quantitative SIMS analysis using cesium bombardment and detection of MCs^+ secondary ions", Nuclear Instruments and Methods in Physics Research Section B: Beam Interactions with Materials and Atoms, Volume 64, Issues 1-4, Pages 621-625, (1992).

[81] Cosimo Gerardi and Claudia Massaro, “On the Improvement of SIMS Technique by the use of MCs^+ Molecular ions”, Microscopy Microanalysis Microstructures, Volume 6, Issue 5-6, Pages 523-531, (1995).

[82] John C. Vickerman and David Briggs, “TOF-SIMS: MATERIAL ANALYSIS BY MASS SPECTROMETRY”, second Edition, IM Publications LLP and SurfaceSpectra Limited, Chichester, UK, 2013.

[83] P. Holliger, F. Laugier and J. C. Dupuy, "SIMS depth profiling of ultrashallow P, Ge and As implants in Si using MCs_2^+ ions", Surface and Interface Analysis, Volume 34, Issue 1, Pages 472-476, (2002).

[84] K. Wittmaack, "Angular dependence of ion yields and cesium surface coverage in Cs+ attachment secondary ion mass spectrometry (CsAMS)", Nuclear Instruments and Methods in Physics Research Section B: Beam Interactions with Materials and Atoms, Volume 85, Issues 1-4, Pages 374-378, (1994).

[85] SIMS characterization by Hamid Kheyrandish, Aystorm Scientific Ltd., website accessed on 11th January 2012.

http://www.aystorm.com/

[86] Renyu Chen, Hannes Wagner, Amir Dastgheib-Shirazi, Michael Kessler, Zihua Zhu, Pietro P. Altermatt and Scott T. Dunham, “Understanding Coupled Oxide Growth and Phosphorus Diffusion in POCl3 Deposition for Control of Phosphorus Emitter Diffusion”, 38th IEEE Photovoltaics Specialist Conference (PVSC), 3-8 June 2012.

[87] C. Steen, A. Martinez-Limia, P. Pichler, H. Ryssel, S. Paul, W. Lerch, L. Pei, G. Duscher, F. Severac, F. Cristiano and W. Windl, “Distribution and segregation of arsenic at the SiO_2/Si interface”, Journal of Applied Physics, Volume 104, Issue 2, Pages 023518(1-11), (2008).

[88] F. Lau, L. Mader, C. Mazure, C. Werner, and M. Orlowski, "A model for phosphorus segregation at the silicon-silicon dioxide interface", Applied Physics A, Volume 49, Issue 6, Pages 671-675, (1989).

[89] L. Pei, G. Duscher, C. Steen, P. Pichler, H. Ryssel, E. Napolitani, D. De Salvador, A. M. Piro, A. Terrasi, F. Severac, F. Cristiano, K. Ravichandran, N. Gupta, W. Windl, "Detailed arsenic concentration profiles at Si/SiO_2 interfaces", Journal of Applied Physics, Volume 104, Issue 4, Pages 043507(1-11), 2008.

[90] J. Dabrowski, R. A. Casali, H.-J. Müssig, R. Baierle, M. J. Caldas and V. Zavodinsky, "Mechanism of dopant segregation to SiO2/Si(001) interfaces", Journal of Vacuum Science & Technology B, Nanotechnology and Microelectronics: Materials, Processing, Measurement, and Phenomena, Volume 18, Issue 4, Pages 2160-2164, (2000).

[91] Renyu Chen, Hannes Wagner, Amir Dastgheib-Shirazi, Michael Kessler, Zihua Zhu, Vaithiyalingam Shutthanandan, Pietro P. Altermatt and Scott T. Dunham, "A model for phosphosilicate glass depostion via $POCl_3$ for control of phosphorus dose in Si", Journal of Applied Physics, Volume 112, Issue 12, Pages 124912(1-6), (2012).

[92] J. M. Eldridge and P. Balk, "Formation of Phosphosilicate Glass Films on Silicon Dioxide", Transactions of the Metallurgical Society of AIME, Volume 242, Pages 539-545, (1968).

[93] Versum Materials, "Application Notes: Process Guidelines for Using Phosphorus Oxychloride as an N-Type Silicon Dopant", website accessed on 16th May 2012.

https://v8cnuz00-a.akamaihd.net/wp-content/uploads/2016/09/POCl3-applicationnotes-process-guidelines.pdf

[94] D. A. Antoniadis, M. Rodoni and R. W. Dutton, "Impurity Redistribution in SiO -Si during Oxidation: A Numerical Solution Including lnterfacial Fluxes", Journal of the Electrochemical Society, Volume 126, Issue 11, pages 1939-1945, 1979.

[95] B. E. Deal, A. S. Grove, "General Relationship for the Thermal Oxidation of Silicon", Journal of Applied Physics, Volume 36, Issue 12, Pages 3770-3778, 1965.

[96] Doriano Brogioli, "Violation of the mass-action law in dilute chemical systems", The Journal of Chemical Physics, Volume 139, Issue 18, Pages 184102 (1-8), (2013).

[97] Hu, S.M., "Interstitial and vacancy concentrations in the presence of interstitial injection", Journal of Applied Physics, Volume 57, Issue 4, pages 1069-1075, (1985).

[98] E. Sirtl in "Proceedings of the Symposium on Defects in Silicon", edited by W. Murray Bullis and L. C. Kimerling (Electrochemical Society, Pennington), Page 45, (1983).

[99] Yeager, H. R., and R. W. Dutton, "An approach to solving multiparticle diffusion exhibiting nonlinear stiff coupling", IEEE Transactions on Electron Devices, Volume 32, Issue 10, Pages 1964-1976, (1985). 1985.

[100] Eric Garfunkel, Evgeni Gusev and Alexander Vul', "Fundamental Aspects of Ultrathin Dielectrics on Si-based Devices", First Edition, Springer Netherlands, 1998.

[101] H. Bracht, "Diffusion Mechanisms and Intrinsic Point-Defect Properties in Silicon", Materials Research Society Bulletin, Volume 25, Issue 6, Pages 22-27, (2000).

[102] S. K. Dhayalan, J. Kujala, J. Slotte, G. Pourtois, E. Simoen, E. Rosseel, A. Hikavyy, Y. Shimura, S. Iacovo, A. Stesmans, R. Loo, and W. Vandervorst, "On the manifestation of phosphorus-vacancy complexes in epitaxial Si:P films", Applied Physics Letters, Volume 108, Issue 8, Pages 082106(1-4), (2016).

[103] Michael Steyer, Amir Dastgheib-Shirazi, Giso Hahn, Barbara Terheiden, "New method for determination of electrically inactive phosphorus in n-type emitters", Energy Procedia, Volume 77, Pages 316-320, (2015).

[104] G. Micard, A. Dastgheib-Shirazi, M. Steyer, H. Wagner, P. Altermatt, G. Hahn, "Advances in the understanding of phosphorus silicate glass (PSG) formation for accurate process simulation of phosphorus diffusion", 27th European Photovoltaic Solar Energy Conference, Frankfurt, Germany, 24-28 September 2009.

[105] Dinesh Kumar, S. Saravanan and Prakash Suratkar, "Effect of oxygen ambient during phosphorus diffusion on silicon solar cells", Journal of Renewable and Sustainable Energy, Volume 4, Issue 3, Pages 033105(1-8), (2012).

[106] Masashi Uematsu, "Self-diffusion and impurity diffusion in silicon dioxide", Journal of Phase Equilibria and Diffusion, Volume 26, Issue 5, Pages 547-554, (2005).

[107] Kenzo Ibano, Kohei M. Itoh, Masashi Uematsu, "Generation of Excess Si species at Si/ SiO_2 interface and their diffusion into SiO_2 during Si thermal oxidation", Journal of Applied Physics, Volume 103, Issue 2, Pages 026101(1-3), (2008).

[108] Y. K. Takamura, S. H. Jain, P. B. Griffin and J. D. Plummer, "Thermal stability of dopants in laser annealed silicon", Journal of Applied Physics, Volume 92, Issue 1, Pages 230-234, (2002).

[109] H. O. Dokumaci, "Analysis and Modeling of Arsenic Activation and Deactivation in Silicon", University of Florida, Electrical and Computer Engineering, 1997.

[110] M. A. Berding, A. Sher, M. van Schilfgaarde, P. M. Rousseau, and W. E. Spicer, "Deactivation in Heavily Arsenic-Doped Silicon", Applied Physics Letters, Volume 72, Issue 12, Pages 1492-1494, (1998).

[111] C. Ahn and S. T. Dunham, "Charge carrier induced lattice strain and stress effects on As activation in Si", Applied Physics Letters, Volume 93, Issue 2, Pages 022112 (1-3), (2008).

APPENDIX A

Processing runs carried out in this work are shown in Table 3. The delay of gases in reaching the wafers and the delays associated with gas valve on/off states and in pulling the wafers out of the furnace have been approximated and accounted for in the diffusion durations listed in Table 3. Except for process 13, the total gas flow was fixed to 14 SLPM. The bubbler temperature was fixed to 20 ºC for all cases.

Process #	N_2 flow (SLPM)	O_2 flow (SCCM)	$POCl_3$ flow (SCCM)	Temp (°C)	Duration (mins)
1	13.125	500	375	890	1.25
2	13.125	500	375	890	1.58
3	13.125	500	375	890	2.75
4	13.125	500	375	890	5.75
5	13.125	500	375	890	9.25
6	13.125	500	375	890	14.25
7	13.125	500	375	865	5.75
8	13.125	500	375	925	5.75
9	13.125	500	375	968	5.75
10	13.3	500	200	890	9.25
11	12.75	500	750	890	9.25
12	11.75	500	1750	890	9.25
13	8	500	375	890	9.25
14	13.32	300	375	890	9.25
15	12.925	700	375	890	9.25

Table 3. Summary of the diffusion conditions used in this work.

APPENDIX B

The constants A_k, C_k D_k and t_0 that are used in the determination of the surface concentration and the constants B_k and E_k (which are used in the determination of the oxide thicknesses and were discussed in section 4.2) are all process dependent and can be expressed as,

$$Z_k = Z_{11}Z_{22}Z_{33}\ (for\ Z = A, B, C\ D, E\ and\ t)$$

where Z_{11}, Z_{22} and Z_{33} account for the effect of O_2 partial pressure (p_O), $POCl_3$ partial pressure (p_P) and diffusion temperature (T), respectively. Determination of the partial pressures is outlined in Appendix C. The constants Z_{11}, Z_{22} and Z_{33} are given in Tables 4, 5 & 6, respectively. It should be noted that an Arrhenius expression for the constant A_{33} could not be obtained in this study, which can result in erroneous surface concentrations for temperatures outside the temperature range used in this study (865-968 ºC).

Constant	
A_{11}	$\left\{\begin{matrix}-(2.44468\times10^{26}\mathrm{P_O^3})+(3.07694\times10^{25}\mathrm{P_O^2})-\\(1.22767\times10^{24}\mathrm{P_O})+(1.64885\times10^{22})\end{matrix}\right\}/8.03\times10^{20}$
B_{11}	$\left\{\begin{matrix}-(1.77712\times10^{7}\mathrm{P_O^4})+(2.67982\times10^{6}\mathrm{P_O^3})-(1.4298\times10^{5}\mathrm{P_O^2})+\\(3.17489\times10^{3}\mathrm{P_O})-(23.1221)\end{matrix}\right\}/1.1$
C_{11}	$\left\{\begin{matrix}(1.99521\times10^{2}\mathrm{P_O^3})-(25.19484\mathrm{P_O^2})+\\(0.993381\mathrm{P_O})-(0.0113821)\end{matrix}\right\}/0.00093$
D_{11}	$\left\{\begin{matrix}-(5795690\mathrm{P_O^3})+(696697\mathrm{P_O^2})-\\(26468\mathrm{P_O})+(331.79)\end{matrix}\right\}/12.1$
E_{11}	$\left\{\begin{matrix}(166424\mathrm{P_O^3})-(20395.8\mathrm{P_O^2})+\\(798.864\mathrm{P_O})-(6.4749)\end{matrix}\right\}/3.6$
t_{11}	$\left\{\begin{matrix}(1.14953\times10^{9}\mathrm{P_O^4})-(1.67899\times10^{8}\mathrm{P_O^3})+(8.44342\times10^{6}\mathrm{P_O^2})-\\(1.69567\times10^{5}\mathrm{P_O})-(1.19752\times10^{3})\end{matrix}\right\}/130$

Table 4. List of constants used in the determination of Si surface concentration.

Constant	
A_{22}	$\left\{\left(\frac{2.5\times10^{21}+(350p_P-1.6)}{0.475+exp\left(-\left(2200(p_P-0.001475)\right)\right)}\right)+1\right\}/8.03\times10^{20}$
B_{22}	$\left\{\left(\frac{19.9+(350p_P-1.6)}{8.75+exp\left(-\left(5300(p_P-0.002)\right)\right)}\right)+1\right\}/1.1$
C_{22}	$\left\{8.6\times10^{-8}\left(p_p\right)^{-1.34}\right\}/0.00093$
D_{22}	$\left\{\left(\frac{18.05+(350p_P-1.6)}{0.15+exp\left(-\left(2880(p_P-0.0011)\right)\right)}\right)\right\}/12.1$
E_{22}	$\left\{\left(\frac{17+(350p_P-1.6)}{5.25+exp\left(-\left(5000(p_P-0.001)\right)\right)}\right)+1\right\}/3.6$
t_{22}	$\left\{\left(\frac{392.5+(350p_P-1.6)}{1.9+exp\left(+\left(4000(p_P-0.001)\right)\right)}\right)+1\right\}/130$

Table 5. List of constants used in the determination of Si surface concentration.

Constant	
A_{33}	$(1.48537\times10^{15}\mathrm{T}^3)-(5.29244\times10^{18}\mathrm{T}^2)+$ $(6.29044\times10^{21}\mathrm{T})-(2.49314\times10^{24})$
B_{33}	$1.02\times10^{10}exp(-2.3/KT)$
C_{33}	$2.6\times10^{-13}exp(2.21/KT)$
D_{33}	$4.19\times10^{2}exp(-0.37/KT)$
E_{33}	$1.29\times10^{4}exp(-0.82/KT)$
t_{33}	$1.93\times exp(0.42/KT)$

Table 6. List of constants used in the determination of Si surface concentration.

Determination the partial pressure (p_X) of a gas constituent X, is given below. $p_X = \eta_X \times 1atm$

where η_X is the mole fraction of X which is given by,

$$\eta_X = W_X \times (M_{ave}/M_X)$$

where W_X is the mass fraction of X, M_{ave} is the average molecular mass of the gas mixture and M_X is the molecular mass of X.

The mass flow rate of a gas constituent, X, is given by,

$$m_X^{flow} = \frac{M_X P}{RT}$$

The mass flow rate m_X^{flow} of a gas constituent, X, is given by,

$$m_X^{flow} = \frac{M_X P}{RT} V_X^{\wedge} \qquad (g/min)$$

where P is the pressure taken as 1 atm (pressure in FAB), T is 273.15 ^{o}K (0 ^{o}C) and R is the gas constant (82.1 $(cm^{-3}.atm)/(mole.K)$).

$V_X^{\wedge}$ is the volumetric flow rate in units of SCCM. For O_2 and N_2 this is simply given by the flow rates of the respective MFCs. $V_{POCl_3}^{\wedge}$ is given by,

$$V_{POCl_3}^{\wedge} = \left[\frac{P_{vap}}{P_B - P_{vap}}\right] V_{N_2 POCl_3}^{\wedge}$$

where P_{vap} is the vapour pressure at bubbler temperature, P_B is the pressure in bubbler (i.e. atmospheric pressure in FAB) and $V_{N_2 POCl_3}^{\wedge}$ is the N_2 flow rate flowing through the $POCl_3$ bubbler. For a maximum bubbler flow of 2 SLPM (2000 SCCM) the $POCl_3$ pick up rate is 0.5 g/min which (at bubbler temperatures) translates into an actual flow of ~ 70 SCCM of

pure $POCl_3$. P_{vap} is a function of bubbler temperature and can be found in the supplier's notes [93].

The resulting surface concentrations for different temperatures and $POCl_3$ partial pressures are shown in Figures 51 and 52, respectively. Markers represent surface concentrations as determined experimentally.

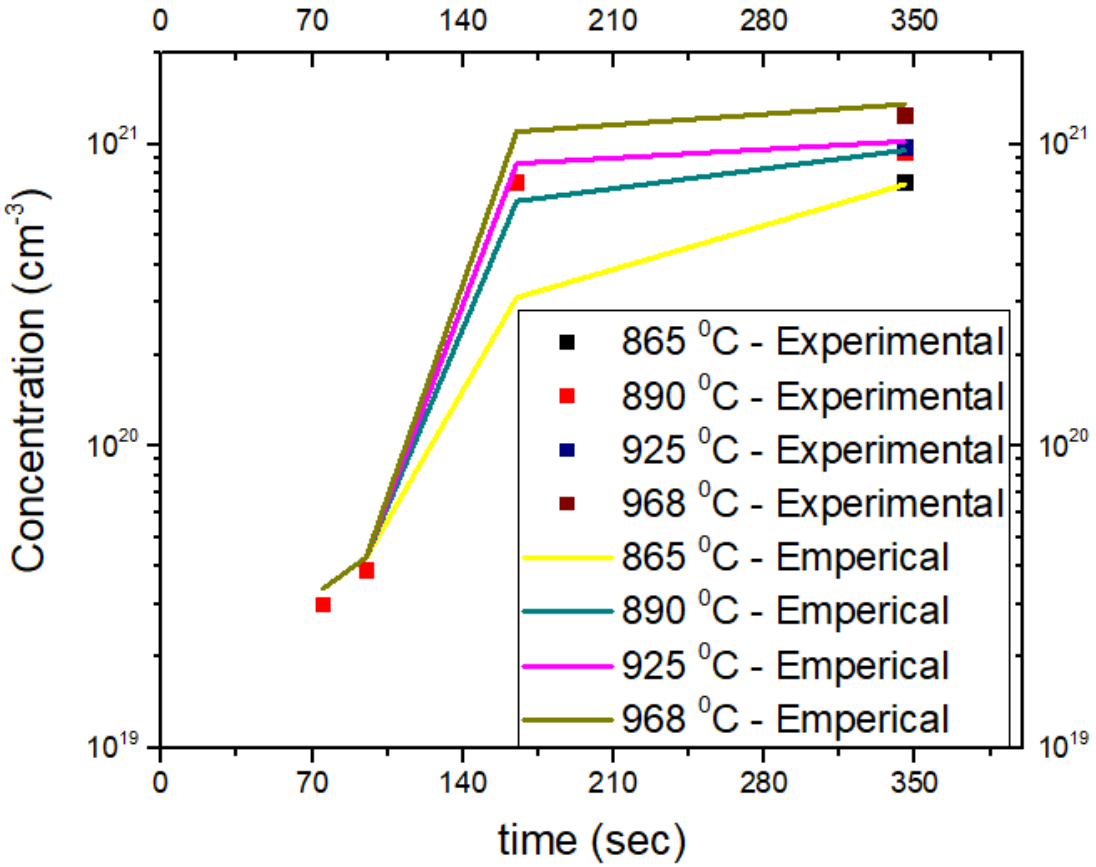


Figure 51: Experimentally and empirically (using equation 4.4) determined phosphorus concentration at the *Si* surface concentration as a function of diffusion duration for the different diffusion temperatures.

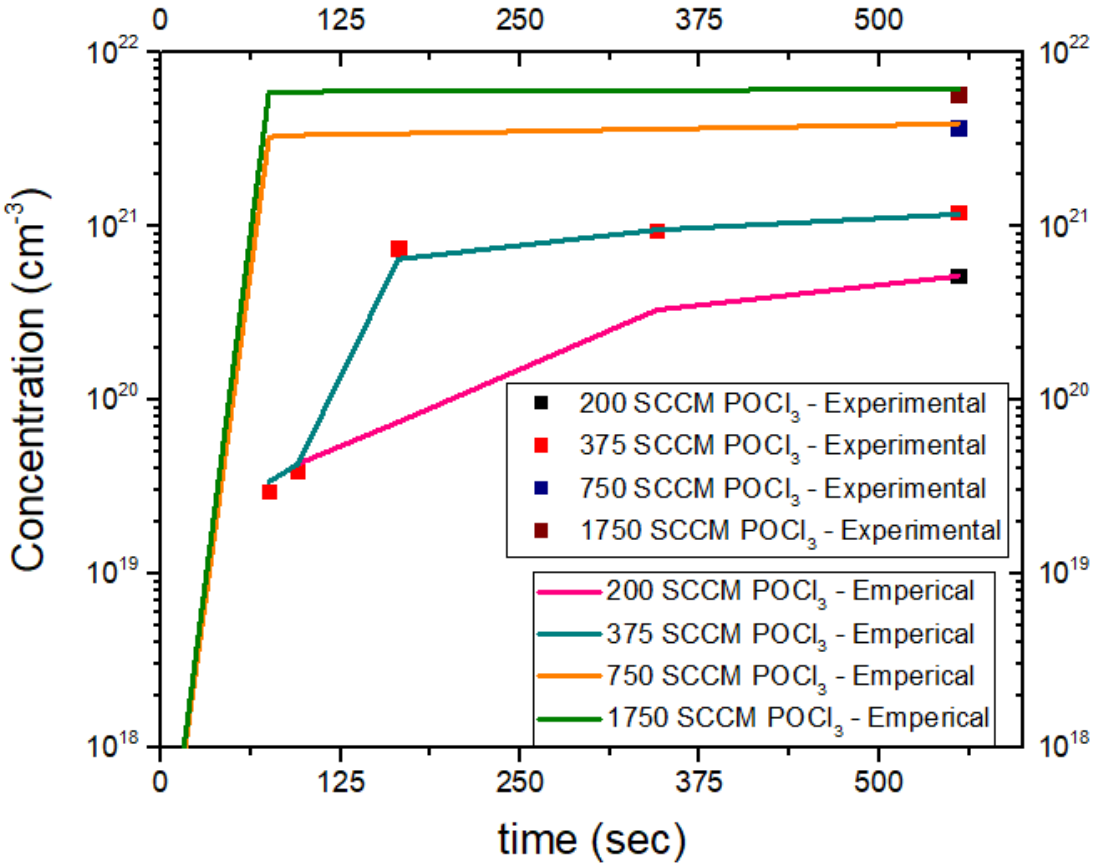


Figure 52: Experimentally and empirically (using equation 4.4) determined phosphorus concentration at the *Si* surface concentration as a function of diffusion duration for the different $POCl_3$ partial pressures.